



UNIVERSITY OF UDINE

Polytechnic Department of Engineering and Architecture
Ph.D. Course in Energy and Environmental Engineering Sciences

Doctoral Thesis

Liquid crystal thermography for the thermal analysis
of gas turbine blades internal cooling systems

Supervisor
Prof. Luca Casarsa

Candidate
Lorenzon Andrea

XXXII Ph.D. Cycle
2020

Abstract

The present work focus on the analysis of the transient liquid crystal thermography, which is employed to accomplish spatially resolved heat transfer performance on cooling channel of gas turbine blades. This methodology has already been implemented to its early stage in the rotating channel test facility of the Turbomachinery and Energy Systems Laboratory of the University of Udine; however, several aspects are still unsettled. Therefore, the main objectives of this thesis is to address the accuracy and validation of the transient thermography technique with the particular approach developed at the University of Udine.

With these aims, transient thermography tests are carried out in a ribbed cooling channel on both static and rotating conditions. Even if a very common channel geometry has been chosen as a study case, no reliable experimental data were found in the open literature for validation purposes. In order to overcome this lack, the heat transfer data necessary to perform the comparison are achieved with the better-established liquid crystal thermography in steady-state approach.

This work addresses further development and improvement of the test facility to make possible the implementation of the steady-state methodology. Moreover, a complex iterative numerical procedure is set up to estimate the heat losses that are the major cause of the lack of accuracy in the steady-state thermography measurements. Part of the work was also dedicated to the definition of the best calibration methodology to take when liquid crystals are exploited as temperature indicators in transient thermography; especially, when liquid crystals with activation temperatures below ambient one are used, as in the present case. The results clearly show that the temperature evolution approach must be preferred to the previously used calibration method (gradient temperature approach).

The results for all the rotation conditions provided by the two experimental approaches are in good agreement, representing the evidence of the validation of the transient thermography. Nevertheless, this work suggests a possible method to estimate the uncertainty of the heat transfer coefficient values in transient experimental approach, and this is done by a sensitivity analysis to the variation of the most important experimental parameters.

Furthermore, the influence of two uneven channel wall heating conditions on the local heat transfer distribution is investigated by means of the steady-state technique. The results show that the uneven thermal conditions have negligible

impact on the stationary case, but they significantly affect the heat transfer when the rotation takes place. This can be due to the different buoyancy effects that in turns affects the secondary flow structures, and consequently, the local heat transfer. Anyway, additional investigations are required to better understand the reasons why of this behaviour.

Contents

| | |
|--|-------------|
| Abstract | iii |
| List of Figures | vii |
| List of Tables | xi |
| List of Acronyms | xiii |
| List of Symbols | xv |
| 1 Introduction | 1 |
| 1.1 Gas turbine overview | 1 |
| 1.1.1 Cycle performance | 3 |
| 1.2 Turbine blade cooling systems | 6 |
| 1.2.1 Effect of rotation in internal channel cooling | 11 |
| 1.2.2 Heat transfer model and measurement techniques | 14 |
| 1.2.3 Similarity parameters for heat transfer in cooling channel . | 16 |
| 1.3 Scope of the present work | 17 |
| 2 Liquid crystal thermography | 19 |
| 2.1 General introduction to liquid crystal | 19 |
| 2.2 Colour digital description | 23 |
| 2.3 Thermography in steady-state method | 24 |
| 2.4 Thermography in transient method | 26 |
| 3 Experimental setup | 31 |
| 3.1 Case description | 31 |
| 3.1.1 Channel model for transient approach | 33 |
| 3.1.2 Channel model for steady-state approach | 35 |
| 3.2 Test facility | 36 |
| 3.2.1 The basement | 38 |
| 3.2.2 The rotating arm | 39 |
| 3.2.3 The air conditioning section and the heater foil supply system | 45 |
| 3.2.4 Control system | 47 |
| 3.3 Calibration facilities | 50 |
| 3.3.1 Temperature gradient approach | 51 |

| | | |
|----------|---|------------|
| 3.3.2 | Temperature evolution approach | 52 |
| 3.4 | Liquid crystals surface preparation technique | 54 |
| 4 | Data reduction | 57 |
| 4.1 | Camera calibration | 57 |
| 4.1.1 | Color calibration | 57 |
| 4.1.2 | Spatial calibration | 59 |
| 4.2 | Transient experiments data processing | 61 |
| 4.2.1 | Fluid temperature evaluation | 62 |
| 4.2.2 | Surface temperature evaluation | 63 |
| 4.2.3 | Heat transfer evaluation | 69 |
| 4.3 | Steady-state experiments data processing | 70 |
| 4.3.1 | Fluid temperature evaluation | 70 |
| 4.3.2 | Surface temperature evaluation | 70 |
| 4.3.3 | Heat transfer evaluation | 71 |
| 4.4 | Temperature gradient calibration data processing | 76 |
| 4.5 | Temperature evolution calibration data processing | 78 |
| 5 | Results | 81 |
| 5.1 | Liquid crystals calibration | 81 |
| 5.1.1 | Wide-banded liquid crystals | 81 |
| 5.1.2 | Narrow-banded liquid crystals | 82 |
| 5.2 | Heat transfer distribution | 85 |
| 5.2.1 | Transient tests | 86 |
| 5.2.2 | Steady-state tests | 95 |
| 5.2.3 | Approaches comparison | 101 |
| 6 | Conclusion | 109 |
| A | Thermal proprieties | 113 |
| A.1 | Air | 113 |
| A.2 | Inconel alloy 600 | 115 |
| B | Uncertainty and sensitivity analysis | 117 |
| B.1 | Transient test data elaboration | 117 |
| B.2 | Steady-state test data elaboration | 121 |
| | Bibliography | 129 |

List of Figures

| | | |
|------|---|----|
| 1.1 | Trend of turbine inlet temperature and engine pressure ratio over the years | 1 |
| 1.2 | Gas Turbines of General Electric | 2 |
| 1.3 | Major sections of a gas turbine engine (GE90-series) | 3 |
| 1.4 | Gas turbine layout and Brayton-Joule cycle | 3 |
| 1.5 | Real working cycle of gas turbine | 5 |
| 1.6 | Turbine inlet temperature and developed cooling technology over the years | 6 |
| 1.7 | Example of cooling scheme in a turbine blade | 7 |
| 1.8 | Examples of rib arrangements and pin fins array at the trailing edge | 8 |
| 1.9 | Flow structure inside a dimple | 9 |
| 1.10 | Impingement cooling concept and impingement cooling arrangement of a gas turbine airfoil | 9 |
| 1.11 | Film cooling concept and high pressure turbine blade protected by film cooling | 10 |
| 1.12 | Stabilizing/destabilizing effects on the boundary layers | 11 |
| 1.13 | Coriolis effects in smooth rotating channel | 12 |
| 1.14 | Formation of instability and the subsequent establishment of the Taylor-Proudman regime | 13 |
| 1.15 | Lumped model of heat transfer in a cooling channel | 14 |
| 2.1 | Schematic representation of the classification of liquid crystals . . | 19 |
| 2.2 | Helycooidally architecture of the cholesteric liquid crystals and constructive interference phenomena | 20 |
| 2.3 | Selectively reflected light as a function of temperature | 21 |
| 2.4 | Representations of RGB colour model and HSL colour model . . . | 23 |
| 2.5 | The two calibration methods of liquid crystals: maximum intensity method and hue method | 23 |
| 2.6 | LC thermography applied in steady-state method | 24 |
| 2.7 | Heat fluxes balance | 25 |
| 2.8 | LC thermography applied in transient method | 26 |
| 2.9 | Semi-infinite-plate problem: reference system of the solid domain | 27 |
| 2.10 | Discretization of fluid temperature variation in order to apply Duhamel's superposition theorem | 28 |
| 3.1 | Main dimension of the ribbed channel model | 31 |

| | | |
|------|---|----|
| 3.2 | Test section relative coordinate system | 32 |
| 3.3 | Liquid crystals painted surface and locations of fluid thermocouples for the transient channel model | 34 |
| 3.4 | Detail of the fluid thermocouple installation | 34 |
| 3.5 | Inconel foils location and connection | 35 |
| 3.6 | Inconel foils location and connection | 35 |
| 3.7 | Comparison of operational range between the previous and the present facilities | 37 |
| 3.8 | Test facility sketch | 37 |
| 3.9 | Test facility with the main basement items | 38 |
| 3.10 | Settling chamber sketch and its photo during the assembly phase | 39 |
| 3.11 | Velocity profiles of the inlet flow | 40 |
| 3.12 | Onboard data acquisition system | 41 |
| 3.13 | Relative position of the vision system items | 42 |
| 3.14 | Virtual model of the equipped rotating arm | 43 |
| 3.15 | Qualitative estimation of rotating arm diplacements | 44 |
| 3.16 | Basement corner displacements evaluation through the laser sys- tem and high-sensitive camera | 44 |
| 3.17 | Nitrogen-air heat exchangers and valves system operating scheme | 45 |
| 3.18 | Example of inlet temperatures achievable | 46 |
| 3.19 | Diagram of the control system connections | 47 |
| 3.20 | Close loop control | 48 |
| 3.21 | Trends of the main parameters during a transient test | 49 |
| 3.22 | Calibration facility sketch, for temperature gradient approach . . | 51 |
| 3.23 | Calibration plate for the temperature evolution approach | 52 |
| 3.24 | Calibration facility sketch, for temperature evolution approach . . | 52 |
| 3.25 | Two-dimensional model for Comsol simulation | 53 |
| 3.26 | Transient copper plate simulation results | 54 |
| 4.1 | Images acquired by the cameras used in the steady-state thermog- raphy | 58 |
| 4.2 | Colour evaluation of the camera images | 58 |
| 4.3 | Reference systems during the spatial calibration | 59 |
| 4.4 | Space transformations | 60 |
| 4.5 | Acquired and dewarped image of the transient model channel . . . | 61 |
| 4.6 | Thermocouples signals acquired during a transient test | 62 |
| 4.7 | Computational grid for fluid temperature interpolation | 62 |
| 4.8 | Interpolated spatial distribution of the fluid temperature at one time instant | 63 |
| 4.9 | Example of ROI of the 9th inter-rib | 64 |
| 4.10 | Image sequence reduction of acquisition for a transient thermog- raphy test and example of the colour history of a pixel | 64 |
| 4.11 | Background subtraction | 65 |
| 4.12 | Frequency spectrum | 66 |
| 4.13 | Raw starting signal and relative filtered signal | 66 |
| 4.14 | Derived points in the peak finding procedure | 67 |

| | | |
|------|---|----|
| 4.15 | Peak finding refinement | 68 |
| 4.16 | Halves of two frames acquired during transient test of the 9th inter-rib at different time and relative liquid crystals activation time map | 69 |
| 4.17 | Wall temperature distribution evaluated from the acquired images | 71 |
| 4.18 | Boundary condition for the conduction problem | 72 |
| 4.19 | Computational mesh used for the conduction problem | 73 |
| 4.20 | Boundary condition for the radiative problem | 74 |
| 4.21 | Block diagram of the heat transfer evaluation procedure | 74 |
| 4.22 | Example of the heat transfer coefficient trends over loop iterations | 75 |
| 4.23 | Example of heat transfer coefficient distribution for first attempt . | 76 |
| 4.24 | Liquid crystals calibration images | 77 |
| 4.25 | Maximum colour intensity method in temperature gradient calibration | 77 |
| 4.26 | Hue method in temperature gradient calibration | 78 |
| 4.27 | Wall and fluid temperature evolutions and relative cooling rates for a transient test | 79 |
| 4.28 | Region of interest (ROI) for averaging colour signals in temperature evolution approach | 79 |
| 4.29 | Maximum colour intensity method in temperature evolution approach | 80 |
| 5.1 | Hue-temperature calibration of R35C7W | 82 |
| 5.2 | Trends of R13C1W calibration temperature for the different calibration approaches | 84 |
| 5.3 | Comparison between the calibration temperatures obtained from the different calibration approaches | 85 |
| 5.4 | Main flow structure into an internal ribbed channel | 86 |
| 5.5 | Definition of averaging windows for transient tests | 86 |
| 5.6 | Average dimensionless wall temperature | 87 |
| 5.7 | Fluid temperature evolutions for static and rotation conditions . . | 88 |
| 5.8 | Comparison between tests carried out with different fluid temperature evolutions | 88 |
| 5.9 | Enhancement factor maps for the different rotation conditions . . | 90 |
| 5.10 | Enhancement factor profiles extracted at $z = 30\text{ mm}$ (R3C1W) and $z = 20\text{ mm}$ (R13C1W) for different rotation conditions | 91 |
| 5.11 | Percentage difference of the enhancement factor between the extracted profile at $z = 30\text{ mm}$ (R3C1W) and $z = 20\text{ mm}$ (R13C1W) for different rotation conditions | 92 |
| 5.12 | Average enhancement factor values along the channel length for different rotation conditions | 93 |
| 5.13 | Normalized enhancement factor at the 9th inter-rib for different rotation conditions | 94 |
| 5.14 | Comparison of the enhancement factor profiles for different rotating conditions | 94 |
| 5.15 | Overall enhancement factor and overall buoyancy parameter comparisons for different rotation conditions | 95 |

| | | |
|------|--|-----|
| 5.16 | Definition of averaging window for steady-state tests | 96 |
| 5.17 | Comparison between the different heat boundary conditions at static condition | 97 |
| 5.18 | Comparison between the different heat boundary conditions for the rotation condition at $Ro = 0.1$ | 98 |
| 5.19 | Comparison between the different heat boundary conditions for the rotation condition at $Ro = 0.18$ | 99 |
| 5.20 | Overall enhancement factor and overall buoyancy parameter comparisons for different rotation conditions | 100 |
| 5.21 | Enhancement factor distribution of the stationary steady-state test with one heated side compared with literature result | 101 |
| 5.22 | Enhancement factor distribution for the first attempt of the iterative data processing procedure compared with literature result | 102 |
| 5.23 | Comparison with literature of the spanwise averaged enhancement factor | 103 |
| 5.24 | Enhancement factor maps obtained for the different thermography methods | 104 |
| 5.25 | Enhancement factor profiles extracted at $z = 20\text{ mm}$ for the different thermography methods | 105 |
| 5.26 | Enhancement factor profiles extracted at $z = 30\text{ mm}$ for the different thermography methods | 106 |
| 5.27 | Average enhancement factor values along the channel length for the different thermography methods | 107 |
| 5.28 | Average enhancement factor of the 9th inter-rib for the different thermography methods | 108 |
| A.1 | Diagrams of air thermodynamic proprieties at pressure of 1 bar | 114 |
| A.2 | Diagrams of electrical resistivity of Inconel alloy 600 | 115 |
| B.1 | Effects of main error sources on the heat transfer values in transient approach tests ($Ro = 0, 0.1$) | 119 |
| B.2 | Effects of main error sources on the heat transfer values in transient approach tests ($Ro = 0.2, 0.3$) | 120 |
| B.3 | Effect of the boundary conditions on the heat transfer distribution: radiative heat fluxes | 122 |
| B.4 | Effect of the boundary conditions on the heat transfer distribution: outer surfaces temperature | 123 |
| B.5 | Effect of the boundary conditions on the heat transfer distribution: heat transfer coefficient on rib areas | 124 |
| B.6 | Effect of the boundary conditions on the heat transfer distribution: heat transfer coefficient on blank areas | 125 |
| B.7 | Effect of the boundary conditions on the heat transfer distribution: heat transfer coefficient on smooth sides | 126 |

List of Tables

| | | |
|-----|---|-----|
| 3.1 | Test matrix of HTC evaluations with LC thermography approaches | 32 |
| 3.2 | Material properties of PMMA | 33 |
| 3.3 | Location of the thermocouples immersed in the flow | 34 |
| 3.4 | Boundary condition parameters of Comsol transient simulation . . | 53 |
| 5.1 | Calibration tests matrix for R35C7W | 81 |
| 5.2 | Calibration temperature of R13C1W and R3C1W liquid crystals resulting from temperature gradient approach | 82 |
| 5.3 | Calibration temperature of R13C1W liquid crystal resulting from temperature evolution approach | 83 |
| 5.4 | Calibration temperature of R3C1W liquid crystal resulting from temperature evolution approach | 83 |
| 5.5 | Summary of liquid crystals calibration temperatures | 85 |
| 5.6 | Test matrix for transient approach experiments | 87 |
| 5.7 | Test matrix for steady-state approach experiments | 96 |
| A.1 | Thermodynamic properties of air at pressure of 1 <i>bar</i> | 113 |
| B.1 | Uncertainties in error sources | 118 |
| B.2 | Uncertainty estimation for the transient tests | 121 |
| B.3 | Boundary condition values considered for the sensitivity analysis . | 122 |

List of Acronyms

| | |
|------|---|
| AC | Alternating Current |
| CCD | Charge-Coupled Device |
| DC | Direct Current |
| IR | Infrared Radiation |
| HSL | Hue, Saturation, Lightness (colour model) |
| HTC | Heat Transfer Coefficient |
| LC | Liquid Crystal |
| LCT | Liquid Crystal Thermography |
| PID | Proportional Integral Derivative controller |
| PIV | Particle Image Velocimetry |
| PMMA | Poly(Methyl MethAcrylate) |
| RAM | Random Access Memory |
| ROI | Region Of Interest |
| RGB | Red, Green, Blue (colour model) |
| UV | UltraViolet light |
| SS | Steady-State liquid crystals thermography test |
| TIFF | Tagged Image File Format |
| TR | Transient liquid crystals thermography test |
| 1HW | One Heated Wall (thermal boundary condition) |
| 3HW | Three Heated Walls (thermal boundary condition) |

List of Symbols

Roman Symbols

| | | |
|-----------------------|---|------------|
| A | surface area | m^2 |
| Bi | Biot number | |
| Bo | Buoyancy number | |
| c_p | specific heat capacity at constant pressure | $W/(Km^2)$ |
| d | wall thickness | m |
| d_{bit} | colour depth of the image | bit |
| D_h | hydraulic diameter | m |
| e | rib height | m |
| E | electric voltage | V |
| EF | enhancement factor | |
| f | frequency | Hz |
| f_c | cutoff frequency | Hz |
| f_s | sampling frequency | Hz |
| F_c | fictitious Coriolis force | N |
| $F_{i \rightarrow j}$ | view factor | |
| Fo | Fourier number | |
| F_r | fictitious centrifugal force | N |
| g | gravitational acceleration | m/s^2 |
| h | heat transfer coefficient | $W/(Km^2)$ |
| H | channel height | m |
| i, j | image coordinates | $pixel$ |
| I | electric current | A |
| k | thermal conductivity | $W/(Km)$ |
| L | characteristic length | m |
| m | mass | kg |
| \dot{m} | mass flow rate | kg/s |
| m_{cw} | counterweight mass | kg |
| M_{RAM} | computer RAM memory | bit |
| M_{ROI} | memory occupied by the images sequence | bit |
| n | refractive index | |
| n_s | number of channel side heated | |
| n_{sd} | number of image sub-domains | |

| | | |
|--------------------------|--|-----------|
| N | number of frames acquired | |
| Nu | Nusselt number | |
| Nu_0 | Nusselt number of fully-developed turbulent flow within a smooth circular section tube | |
| p | pressure | Pa |
| P | pitch | m |
| P_w | wetted perimeter | m |
| P_{joule} | power generated by Joule effect | W |
| Pr | Prandtl number | |
| PD | percentage difference | |
| q | heat flux | W/m^2 |
| q_{cond} | conductive heat flux | W/m^2 |
| q_{conv} | convective heat flux | W/m^2 |
| q_{joule} | heat flux produce by Joule effect | W/m^2 |
| q_{loss} | heat flux loss | W/m^2 |
| q_{rad} | radiative heat flux | W/m^2 |
| r | radial position | m |
| R | electrical resistance | Ω |
| R_{air} | specific gas constant of air | $J/(kgK)$ |
| Re | Reynolds number | |
| Ro | rotation number | |
| S | dimensionless parameter to quantify the stabilizing/destabilizing effect | |
| t | time | s |
| t_{LC} | liquid crystal activation time | s |
| t_{max} | time limit of the transient test | s |
| T | temperature | K |
| T_{amb} | ambient temperature | K |
| T_{aw} | adiabatic wall temperature | K |
| T_f | fluid temperature | K |
| T_f^* | reference fluid temperature | K |
| T_{IN} | channel inlet temperature | K |
| T_{OUT} | channel outlet temperature | K |
| T_w | wall temperature | K |
| T_0 | initial temperature | K |
| u, v, w | fluid velocity components | m/s |
| u_b | fluid bulk velocity | m/s |
| V | volume | m^3 |
| W | channel width | m |
| x, y, z | local space coordinates | m |
| X, Y, Z | global space coordinates | m |
| x_{cw}, y_{cw}, z_{cw} | counterweight position | m |

Greek Symbols

| | | |
|---------------|--|--------------|
| α | thermal diffusivity | m^2/s |
| β | overall pressure ratio | |
| γ | heat capacity ratio | |
| δ | incident lighth direction | rad |
| ε | radiative emissivity | |
| ζ | dimensionless coordinate | |
| η | overall real cycle efficiency | |
| η_{id} | overall ideal cycle efficiency | |
| η_c | compressor efficiency | |
| η_t | turbine efficiency | |
| θ | dimensionless temperature | |
| θ_w | dimensionless wall temperature | |
| λ | light wavelength | m |
| μ | dynamic viscosity | $Pa\ s$ |
| ρ | density | kg/m^3 |
| σ | Stefan-Boltzmann constant | $W/(K^4m^2)$ |
| τ | penetration time | s |
| τ_i | i -th temporal moment | s |
| φ | angle of attack of ribs | deg |
| χ | dimensionless heat transfer in the solution of transient energy equation | |
| ψ | boundary layer's vorticity | $1/s$ |
| Ω | angular velocity | rad/s |

Chapter 1

Introduction

1.1 Gas turbine overview

Gas turbines in their modern form were conceived and patented around the end of the 19th century. The low efficiency of components, the unavailability of heat-resisting materials, and the technology at that time made these machines not suitable to operate, if not even made impossible to build them. However, it was the development of the engines used in the propulsion of military aircraft to give a decisive boost to the improvement of gas turbines. In the midst of the Second World War, the first aircraft engines based on gas turbine technology were seen; thanks to von Ohain and Whittle, who made gas turbine engines in 1939 in Germany and in 1941 in England, respectively. The development of gas turbine and the achievement of suitable performances have been strongly influenced by the attainment of a technological maturity that allowed to build compressors with good efficiency at high compression ratios, and it made possible to realize turbines that withstand high temperatures. Figure 1.1 shows the technological evolution of gas turbines since the post-war period. As will be clarified later, the turbine inlet temperature is an index of the technological level reached and of the performance of the entire engine.

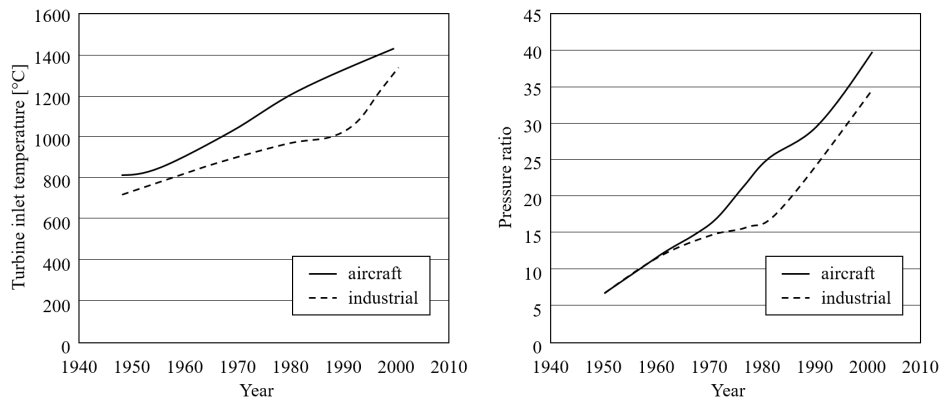


Figure 1.1: Trend of turbine inlet temperature and engine pressure ratio over the years, from Boyce [5]

Nowadays, the gas turbine is the most versatile item of turbomachinery: it can be used in several different ways in critical industries such as power generation, process plants, aviation, and small domestic applications. The global gas turbine market size is expected to register a compound annual growth rate of 4.8% in the forecast period up to 2025 [17]. The continuing success of gas turbine engines is due to the combination of different favourable features, such as the large power-to-weight ratio, the long lifespan, the high reliability, and the high operating flexibility.

Generally, gas turbine engines may be divided into two main types: the ones used for aircraft propulsion, which provide a net thrust as a result of hot gases expansion in the propelling nozzle, and those expressly designed for power production on land-based, which go under the name of heavy-duty applications. As can be seen from Fig. 1.1, heavy-duty applications are generally characterized by lower turbine inlet temperatures and lower pressure ratios. This fact can be explained by considering the massive investments in military aeronautical research, whose developments reflect on the land-based applications. Furthermore, heavy-duty applications have to work for a large number of hours and with high reliability, thereby they are designed to run in less critical operating conditions.



Figure 1.2: Gas Turbines of General Electric: HARriet, heavy-duty gas turbine (left side) and the new Boeing 777X will feature GE9X engine (right side)

The increasing global electricity demand coupled with the ever more awareness about environmental aspects, such as polluting emissions and greenhouse gases, leads to the growth of energy production from renewable energy sources. Renewable sources provide non-programmable production, thus forces a greater flexibility in operating conditions of other power plants. Gas turbine engines can easily meet this requirement, since they have a relatively low start-up time (within a few minutes), and they are capable of pursuing rapid electricity demand variations. Moreover, gas turbines produce lower carbon emissions thanks to the fuel used (natural gas in most cases) and to greater efficiency when they are used in combined cycle configurations. Therefore, from an economic and an environmental perspective there is a high interest and a strong push to develop more and more efficient gas turbine engines.

1.1.1 Cycle performance

The architecture of a typical gas turbine used in aeronautic application is shown in Fig. 1.3. It is composed by the compressor section of the engine through which ambient air is compressed before entering into the combustion chamber. Fuel is introduced and burned in the combustion chamber in order to add heat to the flow. The hot gasses resulting from the combustion expand passing through the turbine, then gasses are discharged to the atmosphere providing the propulsive thrust. Conversely, in heavy-duty applications where there is no interest in propulsion, greater extraction of work is preferred. Anyway, a certain part of the work extracted by the turbine is used to drive the compressor in order to compress the intake air, for this reasons, the two turbomachines of the engine are keyed on the same shaft.

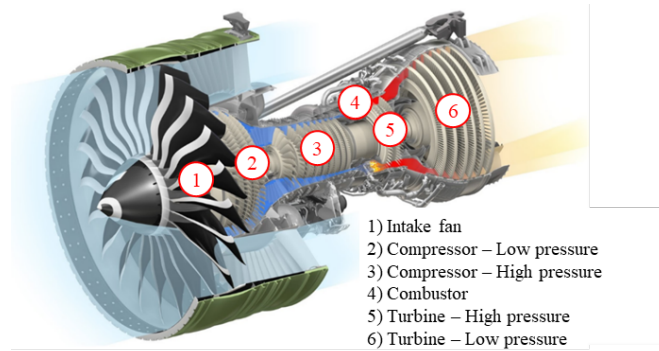


Figure 1.3: Major sections of a gas turbine engine (GE90-series)

The simplified thermodynamic study of gas turbines can be done on the lumped model such as provided in Fig. 1.4 and on the Brayton-Joule cycle. With reference to the ideal close cycle, the fluid is compressed by an isentropic compression (from point 1 to 2), after which heat is supplied at constant pressure (from point 2 to 3). Following, there is the isentropic expansion where work is extracted (from point 3 to 4) and, finally, the fluid returns to the starting point giving heat at constant pressure (from point 4 to 1).

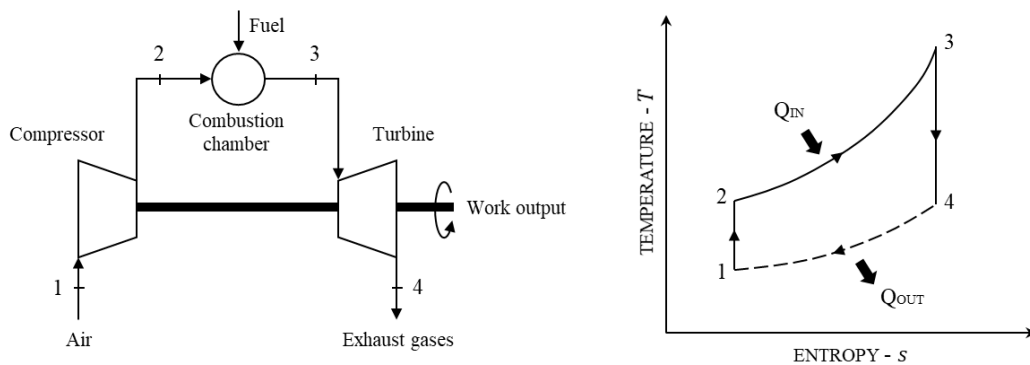


Figure 1.4: Gas turbine layout (left side) and Brayton-Joule cycle (right side)

The ideal cycle efficiency depends on the overall pressure ratio β , between the two isobaric thermodynamic transformations, and on the heat capacity ratio γ of the ideal gas:

$$\eta_{id} = 1 - \frac{1}{\beta^{\frac{\gamma-1}{\gamma}}} \quad (1.1)$$

Actually, in the real engine, the ambient air is compressed and then after the combustion, a gas mixture is formed with different chemical composition and thermodynamic properties relative to pure air (no ideal gas). These gases are expelled and they will not take part in the cycle again (open cycle). Moreover, compared to the ideal one, in the real cycle it is possible to list the following loss contributions:

- *At the inlet:* the possible presence of the inlet filters and particular kind of suction duct (that does not diffuser the flow) generate pressure drops and consequently, the compression starts from a pressure lower than the atmospheric one.
- *In the compression phase:* the thermodynamic transformation is not isentropic, caused by the losses occurring inside the compressor. They are taken into account by a compression efficiency.
- *In the combustion chamber:* pressure drop occurs and, consequently, the heat transfer process doesn't take place along an isobaric transformation. Furthermore, the process is not completely adiabatic because there are unavoidable heat losses.
- *In the expansion phase:* thermodynamic losses take place inside the turbine and they are taken into account by an expansion efficiency.
- *At the outlet:* since there is outlet pressure drop, the discharge pressure is slightly higher than the atmospheric one.
- *To the cooling system:* part of the compressed air bypasses the combustion chamber and is directed into the cooling systems of the turbine, consequently this air doesn't participate wholly in the combustion and in the expansion phases.
- *Mechanical and electrical losses:* the mechanical losses in the transmission components are taken into account by the mechanical efficiency. If the gas turbine is coupled to an electric generator, there will be electrical losses to be taken into account.

However, the performance analysis of the real cycle can be carried out in a similar way to what is done for the ideal cycle. It is possible to refer to a cycle in which only turbomachinery's irreversibilities are introduced. This way, the information does not lose its general validity, since the overall efficiency is penalized mostly by

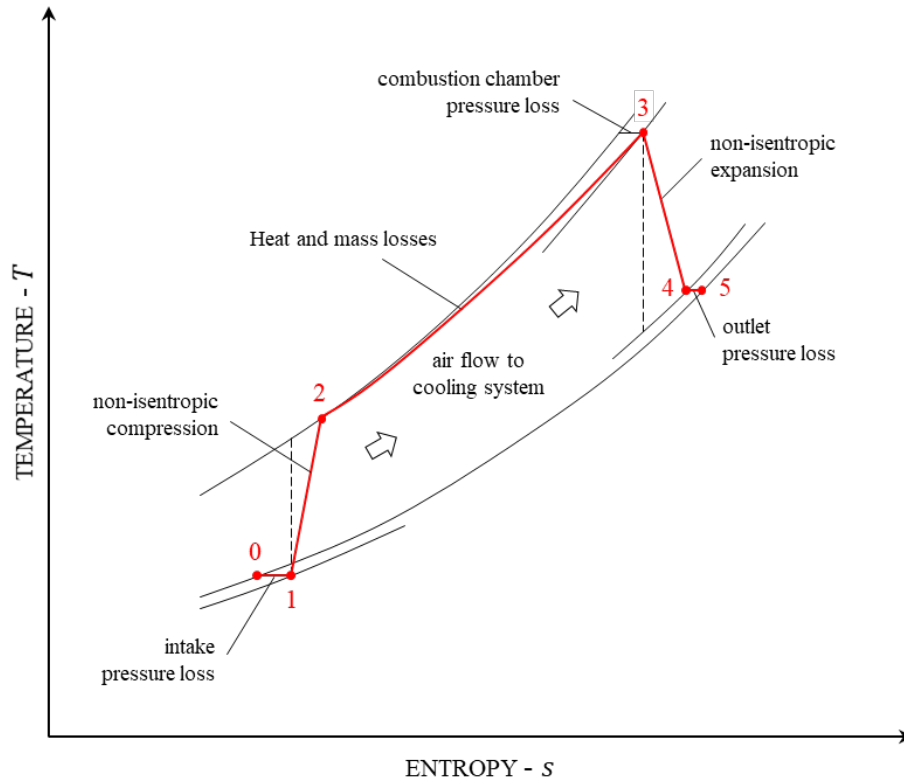


Figure 1.5: Real working cycle of gas turbine

the thermodynamic losses set up within the turbomachines. Under this assumption the overall efficiency still depends on the overall pressure ratio and, further, on the turbomachines efficiency and on the minimum and maximum temperature reached in the cycle:

$$\eta = f\left(\beta, \frac{T_3}{T_1}, \eta_c, \eta_t\right) \quad (1.2)$$

Fixed the minimum temperature of the cycle, that it is determined by the intake air temperature T_1 , in addition to what we have seen for the ideal cycle, the overall cycle efficiency can increase by improving the compressor and turbine efficiencies, or by increasing the maximum temperature of the cycle T_3 . The gases that are entering into the turbine section have the maximum temperature, considering that they are out coming from the combustion chamber. The temperature T_3 is usually renamed as turbine inlet temperature.

The constant quest to increase the turbine inlet temperature in favour of the best cycle performance involves a significant technological challenge and several material resistance issues. The engine components nearby the hot gas path operate in high-temperature conditions, which weaken the mechanical resistance and can cause the drastic reduction of the engine's lifespan.

1.2 Turbine blade cooling systems

The increasing of turbine inlet temperature has been first achieved by innovation in technological and metallurgic fields. This was possible thanks to the improvement of steel alloys; which, after being wrought and cast, have high mechanical properties and chemical resistance even at high temperatures. Fibre-reinforced alloys and thermal barrier coating have been deployed to extend the temperature operating range. Ceramic materials could be an alternative solution instead of metal alloys. Unfortunately, the use of ceramic blades in the turbine still creates problems because of the high thermal and tensile stresses, which these components must withstand; even so, some intermediate solutions have been applied in which metal alloys and ceramic materials are exploited in conjunction. In addition to improvements made in the metallurgical domain, the implementation of cooling systems in the inlet turbine vanes and turbine blades has led to increase even more the turbine inlet temperature. Cooling schemes are also necessary to avoid creeping, thermal fatigue, unwanted heterogeneous temperature distribution inside the blade and minimize hot oxidation. Commonly, cooling is necessary only in the early high-pressure turbine stages, after which the extracted work involves a reduction of the exhaust hot gas enthalpy and, consequently, the temperature falls below the tolerable limits of materials. Commonly, cooling is necessary only in the early high-pressure turbine stages, after which the extracted work involves a reduction of the exhaust hot gas enthalpy and so the temperature falls below the tolerable limits of materials. Over the years, various cooling techniques have been developed as shown in Fig. 1.6.

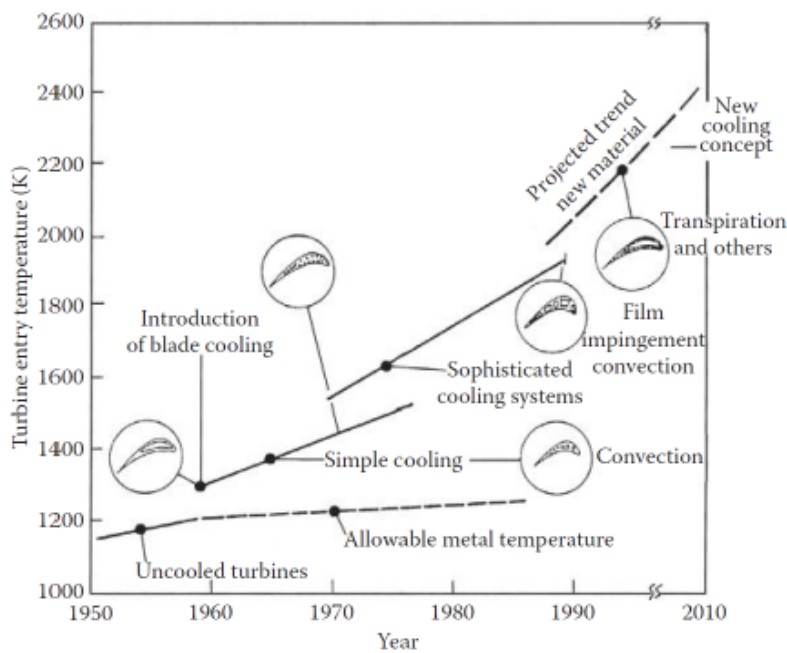


Figure 1.6: Turbine inlet temperature and developed cooling technology over the years, from Lakshminarayana [29]

Depending on the fluid medium used, it is possible to divide cooling systems into two categories: liquid cooling techniques and air cooling techniques. Obviously, heat transfer capabilities of liquid are far greater than those which involve the use of air, thanks to high specific heat and greater density. However, in aeronautical applications, the demand to have light engines and the availability of compressed air overcomes the advantages of liquid cooling. In air cooling systems, the air is bled from the last stages of the compressor. It follows that a minor mass flow rate of air takes part in the combustion and expands in the turbine, causing a lower efficiency and power. This reduction is largely overcome by the increase in the total gas turbine performance, thanks to the higher turbine inlet temperature that is possible to achieve adopting the cooling system.

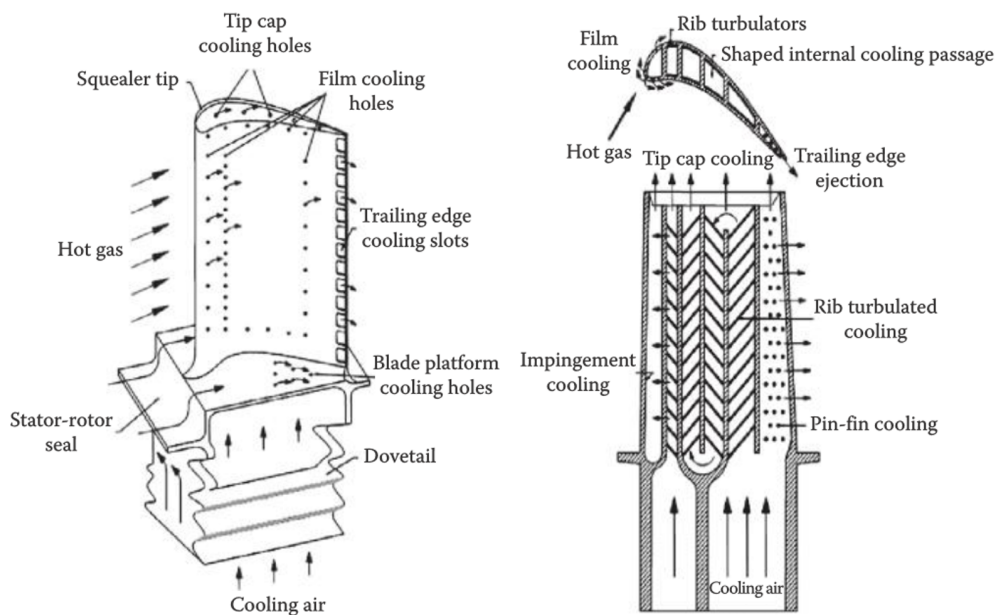


Figure 1.7: Example of cooling scheme in a turbine blade: external cooling (left side) and internal cooling (right side), from Han et al. [18]

As stated before, the cooling system has to be designed to ensure that the maximum surface temperature and the temperature gradient into the blade are below the maximum thermal stress admissible by the material. At the same time, it is important to minimize the consumption of the coolant process to avoid a great amount of power reduction. This goal can be only achieved with a clever combination of different cooling techniques (see Fig. 1.7), and Ligrani [31] provides a wide review of the state of the art of it. The cooling blade configurations and technologies are complex and have a wide geometry variety from manufacturer to manufacturer. Furthermore, many projects of cooling systems are the intellectual property of the producers and are not publicly available in the literature. However, several cooling techniques are possible to be mentioned as the bricks on whom blade cooling had been built from its birth to the present day. They are usually classified in internal or external cooling systems, according to the side of the blade wall to which they are applied. Internal ones are techniques in which

the heat is removed from the inside of the thermally stressed component; the external ones ejects out the coolant from inside the blade onto the hot gas side in order to protect the blade. From the definition of the latter, they are not strictly cooling methods but they are more properly named as protection systems.

Internal forced convection was clearly the first solution employed for blade cooling. In the early application, the coolant was forced to pass through internal radial straight channels from hub to tip of blades. Nowadays, the geometry of the internal channels has become complex: serpentine-shaped channels with different cross-sections are built inside the blade. Various features can be realized on channels' surfaces in order to enhance the heat transfer by disrupting the fluid-dynamic and thermal boundary layers, furthermore by increasing flow turbulence and mixing. These devices, called turbulence promoters, have to fulfil the aforementioned task and, at the same time, do not rise too much pressure losses. The most common used turbulence promoters are ribs and pin-fins as shown in Fig 1.8. The ribs are strips arranged transverse to the bulk flow direction, which can have different cross-section shape (e.g., square, rectangle, triangular) and several types of arrangement in the space. Pin-fins cooling consists of prismatic support (commonly with circular section) spacing with different geometric relationship. They are widely exploited in thin sections of the blade (e.g., trailing edge) because they also have a structural role.

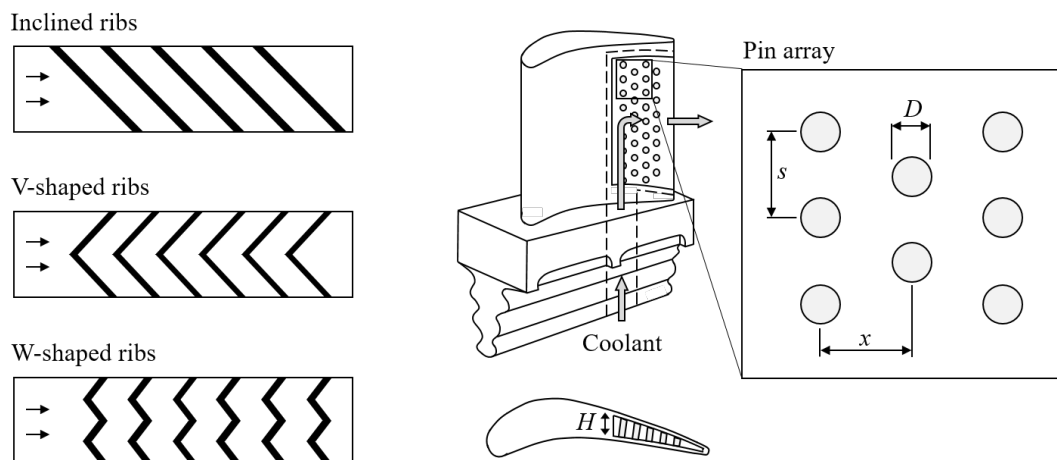


Figure 1.8: Examples of rib arrangements (left side) and pin fins array at the trailing edge (right side)

Dimples are another kind of turbulence promoters, also known as concavities, with whom the heat transfer enhancement is achieved with recessions in the surfaces instead of protrusion, as in the case of the previous turbulence promoters mentioned. They are usually spherical in shape and, as sketched in Fig. 1.9, they generate organized vortical structures that promote flow mixing. The use of dimples do not produce significant amounts of form drag (they produce lower pressure losses respect to ribs and pins), therefore dimples are applied for cooling turbine stages where lower pressure cooling air is employed, or in channels where certain pressure margins have to be maintained downstream the obstacles array.

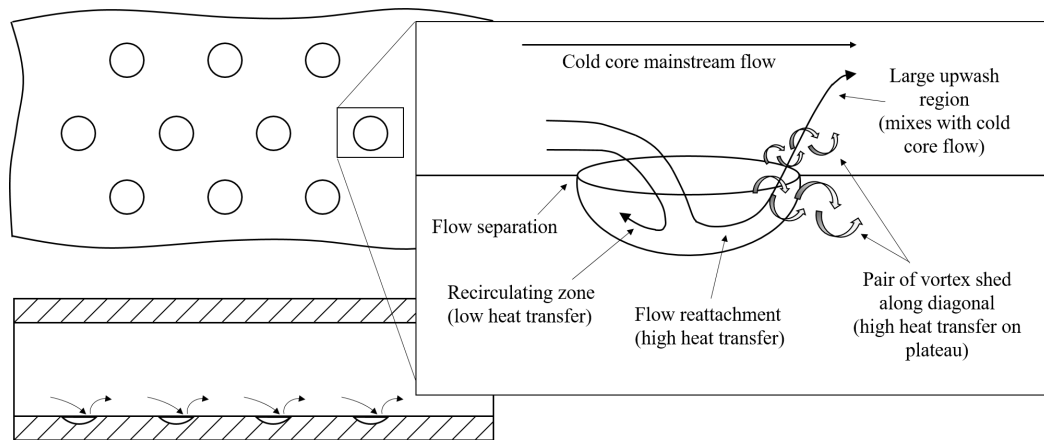


Figure 1.9: Flow structure inside a dimple

In critical sections of the blade where the thermal loads are extremely high and the area is limited (e.g., leading edge), the common solution to increase the heat transfer is to exploit the so-called impingement cooling. With reference with the Fig. 1.10, the air moving inside internal blade passages (feeding channels) is directed against the internal surface of the blade (target surface), through rows of small holes that can have different shape and distribution throughout the channel. In this way, high-velocity impinging jets are generated and, as it is known, they yield high local and area-averaged heat transfer coefficients. The drawback of the impingement is the high-pressure drop, that is due to the dissipation of the dynamic pressure in the impact with the target surface and in the generation of vortical structures.

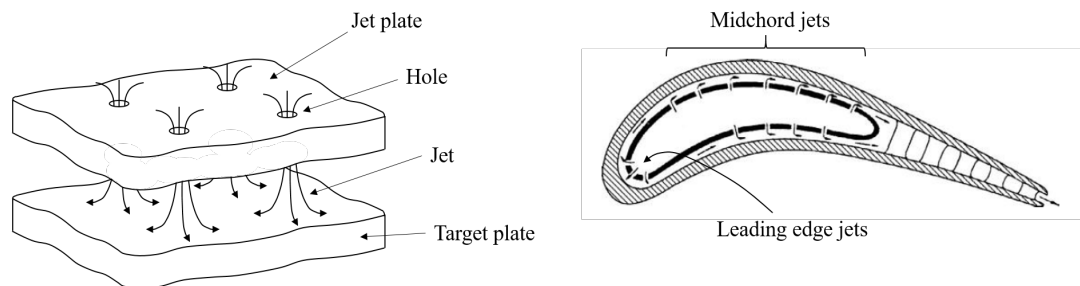


Figure 1.10: Impingement cooling concept (left side) and impingement cooling arrangement of a gas turbine airfoil (right side), from Han et al. [18]

Regarding the protection systems, film cooling is a method in which a thin buffer layer of cooling air covers the outer blade surface, forming a dynamic coating of cold fluid, that protects the material from the hot exhaust gasses. The film is generated and maintained by a continuous discharge of coolant air through a series of surface openings (Fig. 1.11). The openings can be either small holes with exits shaping or bigger slots. Holes are usually located on the blade leading edge, on the first halves of pressure and suction sides. Slots are preferentially

realized in the trailing edge zone of the pressure side, removing part of the material to be cooled while preserving a safe blade thickness (cut-back solution). This technique turns out to be one of the most efficient but, at the same time, the most complicated: the film gradually loses its protective action in the main flow direction as a consequence of the mixing with the hot gases. The mixing produces complex flow structures and thermal field downstream of the holes that could compromise the aerodynamic efficiency of the airfoil. Moreover, the correct prediction of the cooling effectiveness is rather difficult in order to optimize the design of those systems.

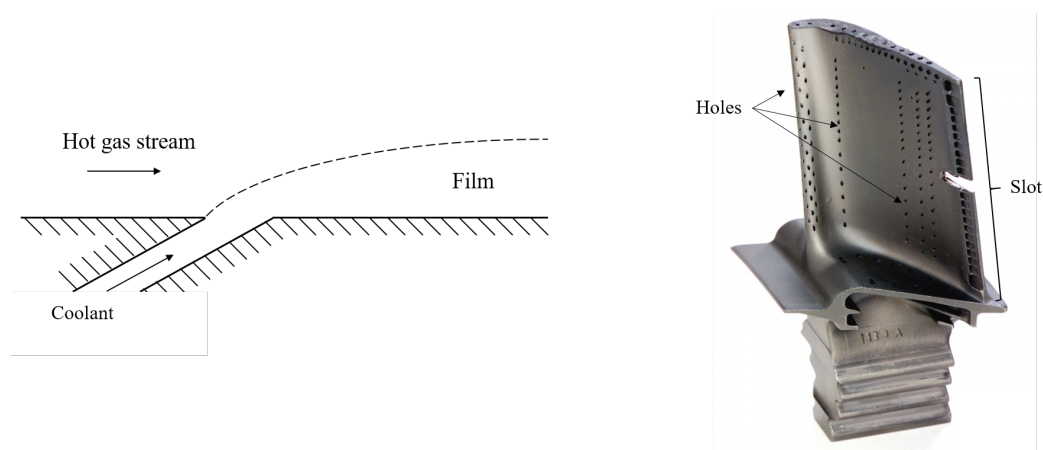


Figure 1.11: Film cooling concept (left side) and high pressure turbine blade protected by film cooling (right side)

Up to date, blades are produced by complex casting processes (e.g., lost-wax casting), in which internal cooling systems are directly obtained (Fig. 1.7). With the ever increasing of the complexity in the cooling system geometry, innovative and advanced manufacturing techniques are being explored to realize blades. In this way, the limitations imposed by the available traditional manufacturing can be overcome by means of additive manufacturing. Anyway, a lot has to be done in order to characterize the manufacturing process and aerothermal performances. The accurate design of the cooling scheme of the high-pressure turbine blades plays a crucial role to ensure performance and lifespan of the gas turbine engine. In the operation and design of these cooling devices, it is of fundamental importance to be able to predict their thermal and fluid dynamic performances. The combined knowledge of the thermal field and the flow field allows developing the best cooling configuration. However, the geometric complexity and working conditions of these devices make the thermodynamic study very complex and challenging. In the past, design engineers could avail themselves of empirical correlations and they exploited the experience gained from previous cooling systems to design new cooling schemes. Today, the information technology progress and the development of better calculation codes have led to the widespread use of numerical simulations favouring the cooling systems design. Indeed, numerical simulations offer new possibilities to dominate the complexity increases allowing engineers to quickly investigate new solutions and offering a design contribution.

However, experimental investigations are necessarily required to validate and to verify the numerical models. Experimental tests are a fundamental method to obtain information concerning surface temperatures distribution and heat flux distribution, as well as the flow field that is established inside the cooling system. For this reason, there are a large number of experimental investigation methods that are continually under development in order to provide information with ever greater resolution and accuracy.

1.2.1 Effect of rotation in internal channel cooling

The effect of the rotation strongly influences the flow field that develops into the cooling channels of the rotor blades and, consequently, it influences the heat transfer distribution too. Therefore, it is important to know which are the main consequences produced by the rotation. The latter can be divided into:

- Stabilizing or destabilizing effects on the boundary layer;
- Coriolis forces effects;
- Centrifugal forces effect.

Johnston [24], Tritton [51], Hart [20] and Speziale [47, 48] extensively treat the secondary vortices and stabilization/destabilization effects on the boundary layer. The vorticity induced by the rotation of the channel Ω significantly impairs the vorticity associated with the turbulent boundary layer.

With reference to Fig. 1.12, the vorticity of the boundary layer is expressed as:

$$\psi = -\frac{du}{dy} \quad (1.3)$$

To quantify the stabilizing/destabilizing effects it is useful to define a dimensionless parameter as:

$$S = \frac{2\Omega}{\psi} \quad (1.4)$$

If the induced vorticity vector and the turbulent boundary layer vorticity have the same orientation ($S > 0$), they will lead to stabilizing effects on the boundary layer, with a decrease of the turbulent kinetic energy and the Reynolds stresses.

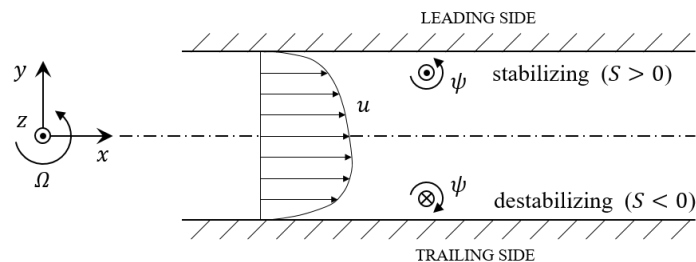


Figure 1.12: Stabilizing/destabilizing effects on the boundary layers

On the contrary, in the case that the two vorticity vectors have opposite orientations ($S < 0$) there will be destabilizing effects, with the increase of turbulent kinetic energy and Reynolds stresses. The increase of turbulent activity at the trailing side leads to an augmentation of the air mixing and, consequently, to the enhancement of the heat transfer.

The fictitious Coriolis force F_c by definition has the relation:

$$\mathbf{F}_c = -2m\boldsymbol{\Omega} \times \mathbf{u} \quad (1.5)$$

where \mathbf{u} is the relative velocity of the fluid flowing in the channel. The Coriolis force can be decomposed into the two main components (Fig. 1.13-a): one orthogonal to the flow, directed from the leading side to the trailing side, and one parallel to the flow.

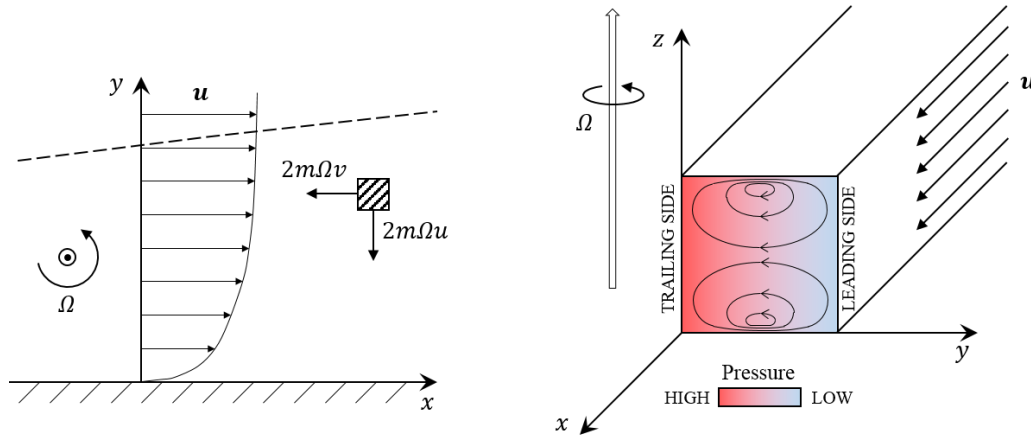


Figure 1.13: Coriolis effects in smooth rotating channel: components of the Coriolis force, from Johnston et al. [24] (left side) and secondary vortices in a rotating channel, from Speziale [47] (right side)

A constant pressure gradient is established along the height of the channel in order to balance the first component of the Coriolis force. The velocity profile is not uniform on the channel section due to the development of the boundary layer near the wall; it results that the Coriolis force will have variable effects along the channel height. Specifically, lower Coriolis forces establish within the boundary layer and the magnitude of those forces are not enough to counteract the pressure gradient. This imbalance leads to the development of a fluid motion from regions with greater pressure (trailing side) towards regions with lower pressure (leading side). The motion is arranged according to a structure, composed of two counter-rotating vortices, that moves the fluid from the boundary layer to channel core (Fig. 1.13-b). The establishment of the secondary vortices gives rise to the second component of the Coriolis force, as a result of the velocity component v presence. This component of the Coriolis force produces an acceleration of the fluid at the boundary layers near the lower and upper channel walls, while it causes a slow down of the core fluid in the centre of the channel.

The component of the Coriolis force in the direction of the main flow leads to the establishment of different forms of instability, according to the rotation regime (Fig. 1.14):

- *low rotation regimes*: the velocity profile is almost parabolic with the formation of a vortex structure near the walls;
- *intermediate rotational regimes*: the instability leads to the formation of multiple cellular vortex structures arranged longitudinally, making the velocity profile wavy;
- *high rotation regimes*: there is a stabilization of the flow with the establishment of a Taylor-Proudman regime, which corresponds to a flat velocity profile. With the exception of the regions near the wall, where the secondary vortices are present.

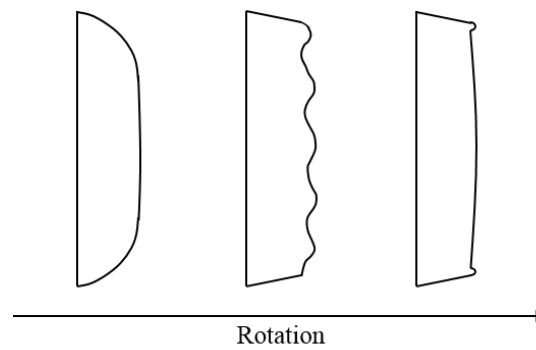


Figure 1.14: Formation of instability and the subsequent establishment of the Taylor-Proudman regime, from Hart [20]

In a flow within a rotating channel, the fluid particles are also subjected to the fictitious centrifugal forces:

$$\mathbf{F}_r = m\Omega^2 \mathbf{r} = (\rho V)\Omega^2 \mathbf{r} \quad (1.6)$$

In Eq. 1.6 it is shown how centrifugal forces depend both on the radial position \mathbf{r} and on the fluid density ρ . Considering two fluid particles with the same radial coordinate, if they have a diverse density they will receive centrifugal forces different in magnitude. The variation of the fluid density into a rotating channel generates particular effects on the flow, these effects are classified under the name of buoyancy effects.

The cooling channel effectiveness is commonly enhanced by promoting the flow mixing and the establishment of certain flow structures. Such behaviours are accomplished by employing a large variety of turbulence promoters. Evidently, the presence of the turbulence features has a considerable influence on the generation of the secondary structures.

1.2.2 Heat transfer model and measurement techniques

The heat transfer that occurs between the coolant and the channel walls is essentially led by forced convection phenomena. Therefore, the heat transfer in a cooling channel could be modelled through the relation:

$$q = h(T_w - T_{aw}) \quad (1.7)$$

The heat transfer rate q coming out from the channel wall at temperature T_w is conditioned by the possibility to exchange with the fluid, on account of the adiabatic wall temperature T_{aw} , and the factor h that is the heat transfer coefficient (HTC). The heat transfer coefficient was assumed dependent on the local geometry and flow condition.

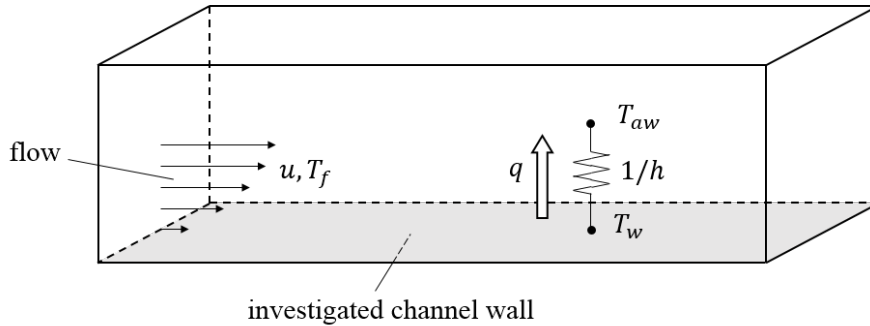


Figure 1.15: Lumped model of heat transfer in a cooling channel

Although there are several ways to construct the temperature driving potential term ($T_w - T_{aw}$), the adiabatic wall temperature T_{aw} is commonly referred to the adiabatic mixing temperature of the flow, also known as bulk temperature:

$$T_{aw} = \frac{\int_A T_f \rho u c_p dA}{\int_A \rho u c_p dA} \quad (1.8)$$

The engineers are interested to investigate the distribution and values of the local heat transfer coefficient. This information can only be obtained through indirect measurement methodologies, that can be applied on real engine cooling components or on scale models. The real operating conditions of the cooling schemes are extremely critical to replicate in the laboratory and they wouldn't easily allow achieving accurate heat transfer coefficient distributions. To overcome this problem, the dimensional analysis shows how it is possible to reproduce the same phenomenon if the dimensionless parameters governing the phenomenon are preserved (they will be presented in Par. 1.2.3).

Anyway, the measurement methodologies can be divided into two categories:

- *Steady-state method.* The inner walls of the channel are kept heated with a known and constant heat flux, while in the channel the coolant is forced to pass. Once the stationary thermal regime of the system is reached, the flow temperature and the channel wall temperature are measured and the

heat transfer coefficient can be evaluated. This technique requires a long time to reach the steady-state and an accurate estimation of the conduction thermal dispersions in the heated walls.

- *Transient method.* Starting from an isothermal condition between the air-flow and the channel walls, a sudden temperature change is imposed on the airflow. The evolution of the wall temperature and the flow temperature are measured so that the heat transfer coefficient is mathematically evaluated using the solution of the transient conduction equation written for the channel wall. This technique requires less time than the steady-state method; moreover, it reduces the influence of lateral conduction as a source of error.

In both methods, it is necessary to measure fluid and solid surface temperatures. The fluid temperature measurement is generally performed by thermocouples immersed in the flow because they represent a cost-effective solution. These devices are also available in miniaturized versions in order to affect the flow field as little as possible and have a fast time-response to the temperature variation.

On the other hand, different techniques can be applied to evaluate the wall temperature. They can be classified according to the spatial distribution of the information they can carry out. There are *two-dimensional indicators*, so-called because they present the temperature distribution on a surface in a continuous way; or *discrete indicators*, since they make available the temperature information only at certain points in the measurement domain. Among the discrete temperature indicators, it can be mentioned thermocouples and thin-film resistance thermometers. Thin-film resistance thermometers are generally preferable in transient measurements since they have a fast time response, while thermocouples have the advantage of smaller dimensions than the resistance sensor.

The most common two-dimensional temperature indicators used are:

- *Thermo-sensitive paints.* The paints are made of substances that are released when it is reached a specific temperature, causing an irreversible colour change. In this way, the isochromatic curves represent isothermal contours. These indicators have low precision and their use is expensive, both in terms of time and economic point of view, because of their irreversible nature.
- *Phase change paints.* They are provided in the form of a suspension in a volatile solvent and they are deposited on the surface, previously painted in black. When a certain temperature is achieved, they show a clear phase change becoming transparent. This creates a contrast with the regions in which the painting has not reached the phase change. This indicator, like the previous one, is irreversible with relatively low precision and high cost.
- *Infrared thermography.* Infrared thermography is a technique which detects infrared energy emitted from an object, converts it to temperature and displays image of temperature distribution. It is possible to obtain temperature maps with high resolution and time response. The main problems

are the estimation of the surface emissivity and the optical accesses, that have to be transparent to the IR radiation. Many materials, that are transparent to the visible spectrum, are opaque to IR radiation (e.g. PMMA, common glass). Therefore, it is usually required to have very expensive quartz windows.

- *Thermochromatic liquid crystals.* It provides one of the most convenient, accurate and consequently popular technique to evaluate wall temperatures, in both experiments carried out in transient or steady-state method. Its convenience is due to the reversible and repeatable behaviour of the liquid crystals. They are painted on the investigated surface and they show a colour change as a function of the temperature at which they are. Knowing the relationship between colours play and temperatures, it is possible to obtain surface temperature distribution with a high resolution.

1.2.3 Similarity parameters for heat transfer in cooling channel

The dimensionless parameters that will be introduced in this section are commonly used to present and discuss the heat transfer that occurs in cooling channels with turbulence promoters. They are collected through the dimensional analysis, according to the Buckingham π theorem, under the assumption of low speed and incompressible flow.

The Nusselt number is accomplished by expressing the heat transfer coefficient in dimensionless form and it represents the relative importance of energy convection against energy conduction:

$$Nu = \frac{hD_h}{k} \quad (1.9)$$

The hydraulic diameter D_h is taken as the characteristic length and it is defined by:

$$D_h = \frac{4A}{P_w} \quad (1.10)$$

where A is the cross-section channel area and P_w the wetted perimeter. The Nusselt number expresses the absolute level of the heat transfer rate but doesn't say very much about the relative heat transfer enhancement earned by the use of the turbulence promoters. For this reason, the Nusselt number is generally presented in a normalized form through the definition of the enhancement factor:

$$EF = \frac{Nu}{Nu_0} \quad (1.11)$$

The denominator Nu_0 is the Nusselt number of a fully-developed turbulent flow within a smooth circular section tube by Dittus-Boelter [11]:

$$Nu_0 = 0.023 Re^{0.8} Pr^b \quad (1.12)$$

In Eq. 1.12 the exponent b is equal to 0.4 for the fluid being heated (wall hotter than the fluid) and 0.3 for the fluid being cooled (wall colder than fluid).

The Prandtl number Pr expresses the ratio of molecular diffusivity of momentum to molecular diffusivity of heat:

$$Pr = \frac{\mu c_p}{k} \quad (1.13)$$

In a static cooling channel, the Nusselt number is a function of the Prandtl number and the Reynolds number $Nu = Nu(Pr, Re)$. The ratio of inertia forces to viscous forces is taken into account by the Reynolds number Re :

$$Re = \frac{\rho u_b D_h}{\mu} \quad (1.14)$$

The Reynolds number is composed by the physical properties of the fluid: the density ρ and the dynamic viscosity μ , by the characteristic length of the channel D_h , and by the bulk velocity of the flow u_b . As stated, when a cooling channel is under rotation, it develops secondary flows that influence the heat transfer. The impact of the rotation effects on the heat transfer is provided by the Rotation number:

$$Ro = \frac{\Omega D_h}{u_b} \quad (1.15)$$

The Buoyancy parameter characterizing the effect of the centrifugal forces that act on the particles with different density is defined as:

$$Bo = \frac{T_w - T_f}{T_f} Ro^2 \frac{r}{D_h} \quad (1.16)$$

where T_w is the temperature of the channel wall, T_f is a representative temperature of the airflow and r is the radius position for which the parameter Bo is evaluated.

1.3 Scope of the present work

The main objective of the present thesis is to further develop and validate the test methodology and facility of the Turbomachinery and Energy Systems Laboratory of the University of Udine, which employs the liquid crystal thermography (LCT) in transient approach in order to evaluate the heat transfer coefficient inside rotating cooling channels.

The facility has been designed and developed to its early stage by Pagnacco et al. [39, 40] for the specific purpose of achieving detailed thermal performances of an internal cooling channel of a high-pressure gas turbine blade. However, several questions concerning measurement accuracy and methodology reliability have not yet been settled, such as:

- Estimation of uncertainty;
- Best methodology for the liquid crystal calibration;
- Effects of buoyancy forces on the results during a transient test.

About uncertainty estimation, the application of standard and well-established approaches (such as Kline & McClintock method) to transient LCT is complicated by the non-explicit form of the equation used to compute the heat transfer coefficient. Therefore, a way to provide a reliable estimation of the measurement uncertainty is necessary to develop and establish.

The LCT experimental approach makes use of liquid crystals (LC) with activation temperature below a standard laboratory environmental temperature. This means that the LC stay for most of their life in the melted phase above the clearing point temperature and are employed during cooling in test phases. Several contributions in literature might suggest a different colour response on cooling and heating for the LC with activation temperature above the environmental temperature [1, 2, 25], on top of this, no contributions are available about the behaviour of LC with activation time close to 0°C . Therefore, an investigation about the best calibration and exploitation strategy is essential to get reliable temperature indications out of them.

Concerning the last point, the transient LCT methodology imposes a temperature step on the coolant flow to initiate the heat transfer process and considers the heat transfer coefficient constant during the test. This assumption may be not strictly true under rotation condition. Indeed, the channel walls undergo continuous cooling, which induces variable buoyancy effects that in turn could affect the heat transfer coefficient over time. Therefore, heat transfer performances were accomplished in a simple rotating channel using the well-known liquid crystal thermography in steady-state approach, in which the buoyancy effects are time-stable, in order to validate the experimental data carried out with the LCT in transient approach. Even if a very common and simplified cooling channel geometry has been chosen as case study, as it will be further commented when presenting the results, the data available in the open literature for validation are pretty much scattered [12, 33, 35], confirming the complexity to reach reliable experimental data when heat transfer measurements are concerned.

Furthermore, the effects of uneven heating conditions within the steady-state LCT technique on the heat transfer have been investigated. Indeed, only the investigated surfaces are commonly heated during steady-state LCT tests [33–35], even if the wall heating condition can cause different buoyancy effects that affect heat transfer. Nevertheless, few contributions in literature have addressed this issue with only averaged heat transfer distribution [41], investigation on smooth channel [45], or numerical approach [52].

In view of the considerations of the above, it should appear clear enough the need for dedicated research activity to validate the test methodology and facility. This can only be achieved by a cross-comparison of reliable data obtained with the better-established LCT in steady-state approach. However, this latter requires a careful approach to the heat losses estimation that indeed will be also addressed in this work.

Chapter 2

Liquid crystal thermography

2.1 General introduction to liquid crystal

The name liquid crystal could appear as an oxymoron: indeed the word liquid it is commonly used to indicate a no long-range molecular order, conversely the word crystal specify a long-range three-dimensional molecular order. However, there are such substances which exhibit intermediate structure with associated molecular order less than that of the crystalline state, but more than that of isotropic liquid. These substances, called “liquid crystals”, were first observed in 1888 by the Austrian botanist F. Reinitzer. He noticed an unusual melting phenomenon of the cholesteryl benzoate that appeared to have two distinct melting points: the first in which the solid melted into an opaque liquid and on further heating, the opacity disappeared. The German physicist O. Lehman conducted descriptive observations of the properties of liquid crystals and he showed how the opaque intermediate phase contained regions that seem to have a crystal-like molecular arrangement.

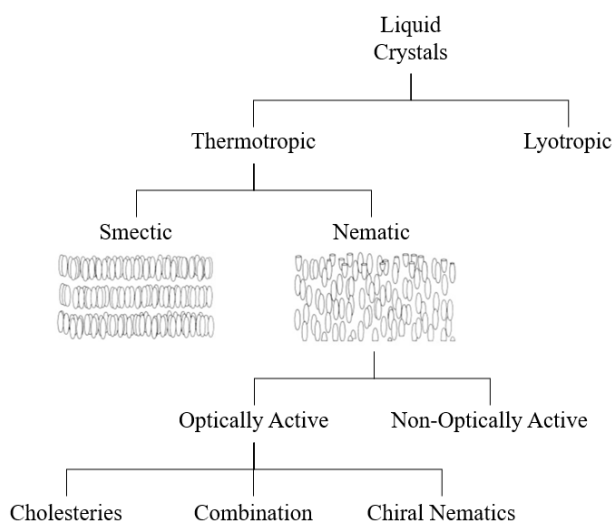


Figure 2.1: Schematic representation of the classification of liquid crystals, adapted from [30]

Nowadays, the accepted classification and nomenclature of liquid crystals is based almost on works conducted by the French mineralogist and crystallographer George Friedel. He was the first to use the term mesophase to indicate the intermediate phase of liquid crystal substances. Many different types of liquid crystal exist as shown in Fig. 2.1 and on them, it can be done the first classification according to the principal means of breaking down the complete molecular order of the solid: lyotropic and thermotropic liquid crystals.

When lyotropic substances are treated with solvent, they exhibit mesophase states. Instead, in thermotropic liquid crystals, the mesophases are thermally activated and related properties change can be used to extrapolate temperature information. It becomes clear that only thermotropic substances shall be used as temperature indicators in order to perform thermography; on the other hand, lyotropic materials have biological interest. For this reason, only thermotropic materials will be discussed furthermore.

Thermotropic liquid crystal class is moreover subdivided in smectic and nematic since the residual molecular ordering of the mesophases has different nature and extent. Spindly and elongated molecules, similar in shape to cigars, form liquid crystals. In smectic mesophase molecules have the long axis parallel and their centres of gravity are layering in planes; differently in nematic mesophase, the molecules remain substantially parallel, but no discrete molecular layer can be identified. In nematic mesophase the molecules centres of gravity are free to move in three directions, so the degree of randomness of nematic molecules is greater than in smectic.

Up to this point, liquid crystals have been classified on the base of the causes that give rise to mesophases and according to the molecular order. Another important distinction within nematic liquid crystals derives from the optical properties of the structure. The nematic mesophase may be optically active (cholesteric or chiral nematic) or not optically active (generally referred to as simply nematic). A nematic phase not optically active have a uniform orientation of the long axis of the molecules (the molecular director). Otherwise, in the mesophases optically active, the molecules are arranged in a stack of thin layer with the director in each layer slightly twisted with respect to those adjacent to it (Fig. 2.2), with the effect of an overall helicoidally architecture.

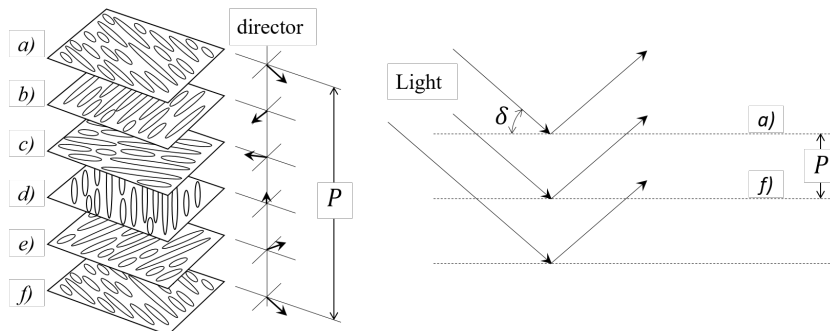


Figure 2.2: Helicoidally architecture of the cholesteric liquid crystals (left side) and constructive interference phenomena (right side)

This is responsible to an unusual optical property: constructive interference phenomena are observed when a white incident light passes through the material, as a result of the reflection by different layers with the same direction of the molecules long axis. According to Bragg's law, the selectively reflected light wavelength λ depends on refractive index n , pitch of helicoidally structure P and the angle δ between incident light direction and the surface:

$$\lambda = nP \sin(\delta) \quad (2.1)$$

In Eq. 2.1 the refractive index is assumed constant (truly it varies with the direction), but the formula remains valid to understand the parameters that affect the phenomena. Temperature variation of the material will modify weak interactions between molecules and so the pitch length of helicoidally structure, which will correspond to a different preferential reflected wavelength light and the displayed colour will be changed (qualitative representation in Fig. 2.3).

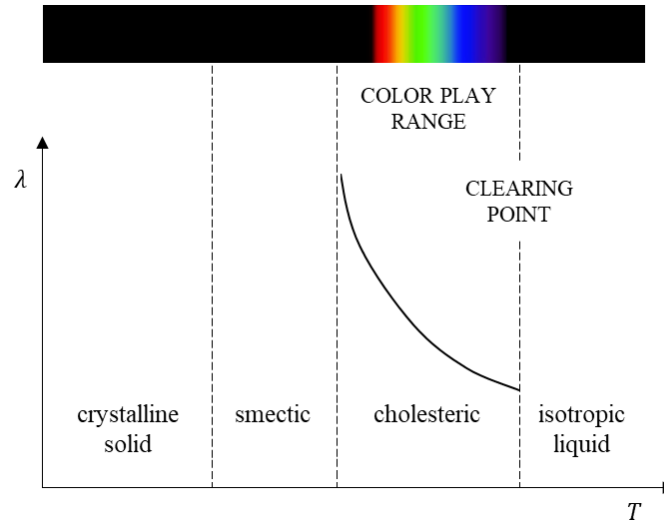


Figure 2.3: Selectively reflected light as a function of temperature

As it had been said, the first compound to exhibit this behaviour was a derivative of cholesterol and the mesophase has historically been called cholesteric. However, other substances have the same mechanism by which changes colour and are not related to cholesterol or other sterol and they are called chiral nematic. Cholesteric and chiral nematic mesophase differ in chemical and physical properties. The different liquid crystal type and its composition affects the selective light reflection behaviour and it makes possible to produce liquid crystals with different temperature ranges in which the colour transition occurs (colour play range). According to the temperature bandwidth where light is reflected in the visible colour range, the liquid crystal can be:

- *Narrow banded*: the entire colour transition occurs within a temperature range closer to 1°C ;
- *Wide banded*: the colour play range is generally from 5 to 20°C .

The liquid crystals (LC) have a repeatable and reversible temperature sensing ability as long as the material is not damaged, so thermochromic LC can be calibrated in order to obtain the relationship between temperature and colour. However, the optical properties can be altered by temperature as well as other factors; in particular: mechanical stress, pressure, chemical environment, electric fields and UV light can modify or destroy colour play. The undesired effects shall be reduced when liquid crystals are encapsulated in gelatine spherical walls of a few tens microns in diameter. In this way, encapsulated LC are available to operate in the temperature range -30 to 115°C , up to a pressure of 133 bar and they are more chemically stable. Moreover, encapsulation reduces the dependence by incident light direction but has the drawback to reduce the intensity of the reflected light.

The liquid crystals are commonly painted onto a surface to perform a non-intrusive measurement of spatially resolved temperature. Therefore, the LC thermography is involved in numerous purposes, for instance: biomedical diagnostic imaging (identification of oedema, micro-nodules, macro-nodules, skin diseases, and other problems associated with vasculature [50]), dissipation estimation and overheating identification of electronic board components, and thermal-fluid mechanics studies. Moreover, the liquid crystals can be dispersed in the fluid to become classical seeding tracers for the flow visualization and, at the same time, local fluid temperature indicators. Regarding the thermal performance evaluations of the blade cooling systems, the LC thermography is performed not only to achieve the temperature surface distribution, but also to deduce other relevant quantities such as the effectiveness of film cooling and the heat transfer that occurs in external and internal cooling schemes. In the following paragraph two methods will be described in which are employed the LC thermography to accomplish the heat transfer distribution in internal cooling channel:

- LC thermography in steady-state approach (Par. 2.3).
- LC thermography in transient approach (Par. 2.4);

During an experiment that involves LC thermography, the accuracy of the temperature evaluation is influenced by the physical and optical properties of liquid crystals. In the steady-state method, the difference between the real temperature of the investigated surface and the temperature indicated by the upper surface of the LC film depends on the wall heat flux, layer thickness and thermal conductivity. In a realistic testing condition, with a heat flux equal to $800\text{ W}/\text{m}^2$, a typical layer thickness of $25\ \mu\text{m}$, and a LC thermal conductivity of $0.2\text{ W}/(\text{Km})$, the temperature difference across the film is about 0.1 K . When liquid crystals are used in transient state method, they have an inevitable delay in time-response to temperature variation of the surface on which they are placed. On this issue, Ireland and Jones [22] report that the accuracy of the temperature evaluation depends on the temperature rate of the surface, layer thickness and LC thermal diffusivity. Anyway, the reaction time of liquid crystals in transient experiments is within the order of milliseconds, therefore with no significant effect on the measurement accuracy.

2.2 Colour digital description

When liquid crystals are used as surface temperature indicators, one or more digital images are necessary to acquire while the liquid crystals are in the colour activation range. Knowing the relationship between colour and temperature, that is obtained in a previous calibration phase, the images can be post-processed in order to evaluate the surface temperature distribution. The digital representation of the real colours is done in the so-called colour space. A colour space is the combination of a colour model and an appropriate mapping function. The mathematical representation of colours is given by the colour model and in the present thesis the following colour models have been used:

- RGB colour model;
- HSL colour model.

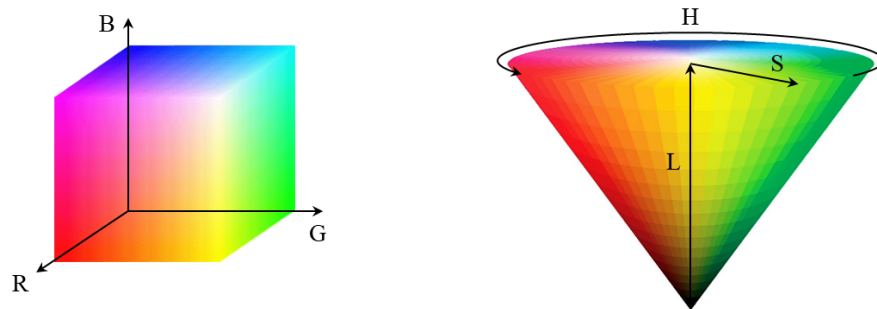


Figure 2.4: Representations of RGB colour model (left side) and HSL colour model (right side)

The RGB colour model is an additive colour model where different kind of colours result from the combination of the three primary colour: red, green and blue. Whereas the HSL colour model is also an additive but the colours are obtained from the other three parameters that are: hue, saturation and lightness. The RGB colour model can be represented in Cartesian space, where the axes are the three primary colour; instead, a pseudo-cylindrical coordinates system is useful to represent HSL colour model as sketched in Fig. 2.4.

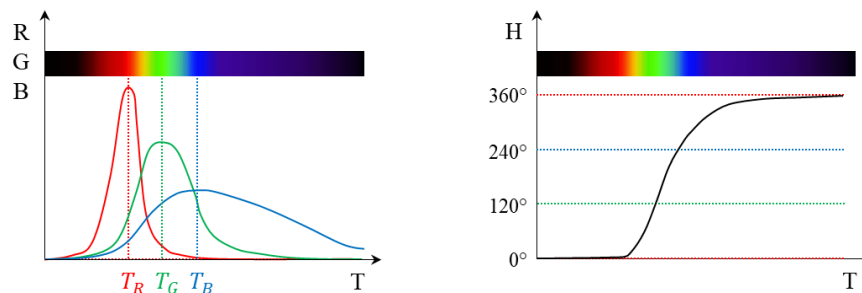


Figure 2.5: The two calibration methods of liquid crystals: maximum intensity method (left side) and hue method (right side)

Since temperatures are measured indirectly, an accurate relationship between temperature and colour shown by liquid crystals has to be found. Two main methods are commonly used to obtain the calibration, depending on where thermography is exploited (Fig. 2.5). One is to assign distinct temperatures at the points where are reached the maximum intensity of the single primary colours. The other one is the hue method, in which hue values from the HSL colour space are correlated continuously with the temperature information. Hue method allows to evaluate surface temperatures within the range of the colour play of the liquid crystal; instead, maximum intensity method can provide less temperature information but it is more accurate and much more sensitive for weak signals than hue method.

2.3 Thermography in steady-state method

The internal boundaries of the channel are heated by means of resistive heating element and simultaneously the air continuously flows in the channel. The resistive heating element is supplied by a DC power supply and dissipates a constant and known heat as a result of the Joule effect. Commonly, the heater element is a foil of conductive material and it is applied to the channel wall by means of an adhesive layer. Then black paint and liquid crystals are deposited on the foil surface. The heater foil can be applied only onto surfaces with single curvature, this reduces the possible regions where the HTC could be investigated by means of the steady-state method. The foil's thickness is chosen as low as possible in order to minimize the lateral conduction; furthermore, the material of the heater must have a low temperature-dependent resistivity in order to generate a uniform heat flux. The heat transfer coefficient could be evaluated through the following energy balance:

$$q_{joule} - q_{loss} = q_{conv} = h(T_w - T_f) \quad (2.2)$$

The heat transferred by forced convection q_{conv} is the net balance between the heat generated q_{joule} and the heat loss q_{loss} .

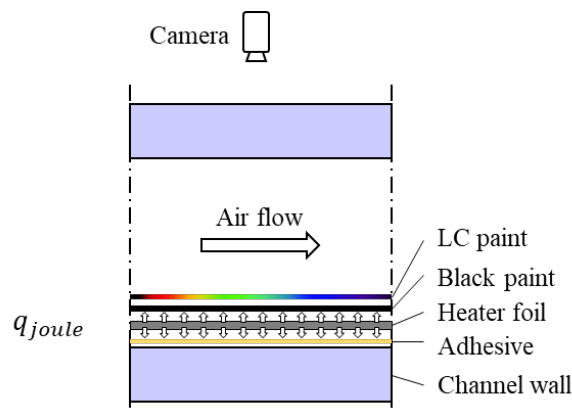


Figure 2.6: LC thermography applied in steady-state method

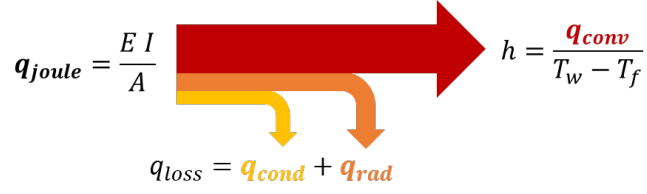


Figure 2.7: Heat fluxes balance

Since the heater foil is supplied by a constant electric voltage E and a constant current I , the Joule heat flux can be expressed as:

$$q_{joule} = \frac{EI}{A} \quad (2.3)$$

where A is the surface area of the heater element. The heat loss can be decomposed into two contributions: the heat conduction loss q_{cond} through the channel wall and the heat radiation loss q_{rad} between the hotter wall surface and the other surrounding channel walls:

$$q_{loss} = q_{cond} + q_{rad} \quad (2.4)$$

The heat conduction loss is due to the establishment of a temperature gradient along the thickness d of the channel wall. Under the assumption of one-dimensional conduction, the conduction term could be evaluated as:

$$q_{cond} = -k_{mat} \frac{\Delta T}{d} \quad (2.5)$$

The heat conduction loss can be minimized by using non-conductive material for the walls and also by applying external extra thermal insulation to the channel (e.g. polyurethane foam). The radiative heat transfer that leaves the surface i and strikes the surface j depends on the surface temperatures (T_i, T_j), the surface emissivities ($\varepsilon_i, \varepsilon_j$), and the view factor $F_{i \rightarrow j}$:

$$q_{rad} = q_{i \rightarrow j} = \frac{1}{A_j} \frac{\sigma(T_i^4 - T_j^4)}{\frac{1 - \varepsilon_i}{A_i \varepsilon_i} + \frac{1}{A_i F_{i \rightarrow j}} + \frac{1 - \varepsilon_j}{A_j \varepsilon_j}} \quad (2.6)$$

Finally, the heat transfer coefficient is calculated from the energy balance as:

$$h = \frac{q_{joule} - q_{cond} - q_{rad}}{T_w - T_f} \quad (2.7)$$

The good estimations of heat generated and heat loss have fundamental importance in order to have good accuracy on the heat transfer coefficient measurements. It is not trivial to correctly evaluate the heat loss and to do this numerical or experimental approach can be used. The steady-state HTC evaluation is a time-consuming method, hence the demand to investigate large surface areas with the fewest number of tests. For this reason, wide-banded liquid crystals are commonly used in this method; moreover, HSL colour model is adopted in order to have a continuous temperature representation of the liquid crystals colour.

2.4 Thermography in transient method

This method is based on the temperature time-response of the channel wall to a sudden change in flow temperature. At initial condition $t < 0$ the wall is at uniform temperature T_0 and in thermal equilibrium with the airflow. At time $t = 0$, a temperature step change is imposed to the airflow from T_0 to T_f .

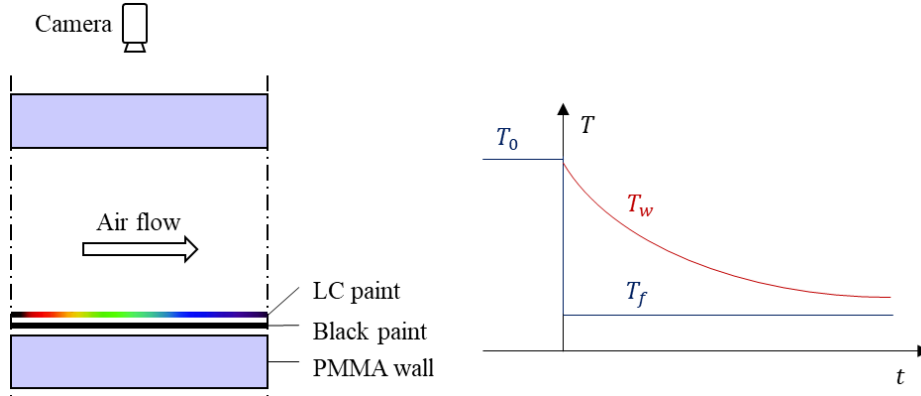


Figure 2.8: LC thermography applied in transient method

It is assumed that pure forced convection with a constant heat transfer coefficient is established. The usual way to evaluate the heat transfer coefficient for the transient method is from the step change solution of the so-called semi-infinite-plate problem [44]. This problem is governed by the Fourier's 1D equation:

$$\frac{\partial T}{\partial t} = \alpha_{mat} \frac{\partial^2 T}{\partial z^2} \quad (2.8)$$

It describes the one-dimensional conduction inside the channel wall domain during a transient regime, considering the material behaviour through the thermal diffusivity α_{mat} . The one-dimension conduction and the semi-infinite assumptions are taken to be valid as long as the testing time is short such that:

- the conductive heat flux is significantly lower than the convection heat flux;
- the penetration depth of heat into the channel wall is small compared to the lateral distance concerned (Kingsley-Rowe et al [26] provide an approximated bidimensional methodology in order to estimate the error committed neglecting the lateral conduction contributions).

In practice, considering a channel wall with a finite thickness d , the penetration time τ is defined as the time taken for the back surface of the channel wall to change temperature by a given amount. The penetration time is used in order to provide the maximum duration of the transient test. According to Schultz et al. [46], the rule of thumb to calculate the maximum testing time is:

$$t_{max} \leq \tau = 0.1 d^2 \frac{\rho_{mat} c_{mat}}{k_{mat}} \quad (2.9)$$

The outcome value of Eq. 2.9 corresponds to the time taken for the back surface to change temperature by the 1% of the term $(T_w - T_0)$ in response to a step-change from T_0 to T_w of the front surface. From Eq. 2.9, it is also possible to deduce that channel walls made of low conductivity materials are the best choice in order to have enough testing time without too thickness.

The initial and boundary condition of Eq. 2.8 for the semi-infinite solution are:

$$\begin{cases} T = T_0 & t = 0 \\ q_{conv} = -k_{mat} \left(\frac{\partial T}{\partial z} \right)_{z=0} = h(T_f - T_w) & t \geq 0 \\ T = T_0 & z \rightarrow +\infty \end{cases} \quad (2.10)$$

The compact form T_w is adopted instead of $T(t, z = 0)$ to indicate the wall solid temperature.

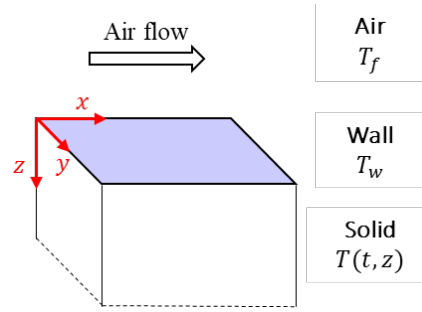


Figure 2.9: Semi-infinite-plate problem: reference system of the solid domain

It is convenient to rewrite the problem in a dimensionless form introducing the *Biot number* and the *Fourier number*, which are defined by:

$$Bi = \frac{hL}{k_{mat}} \quad Fo = \frac{k_{mat} t}{L^2} \quad (2.11)$$

The Biot number expresses the ratio between internal and external thermal resistance, while the Fourier number represents a dimensionless time given by the relationship between physical time and system's internal time constant [10]. The Fourier's 1D equation (Eq. 2.8) becomes in dimensionless form as:

$$\frac{\partial \theta}{\partial Fo} = \frac{\partial^2 \theta}{\partial \zeta^2} \quad (2.12)$$

where the dimensionless coordinate ζ and the dimensionless temperature θ are defined as:

$$\zeta = \frac{z}{L} \quad \theta = \frac{T - T_0}{T_f - T_0} \quad (2.13)$$

The initial and boundary conditions in Eq. 2.10 can be rewritten in the dimensionless form also:

$$\begin{cases} \theta = 0 & Fo = 0 \\ \left(\frac{\partial \theta}{\partial \zeta} \right)_{\zeta=0} = Bi(1 - \theta_w) & Fo \geq 0 \\ \theta = 0 & \zeta \rightarrow +\infty \end{cases} \quad (2.14)$$

The general solution could be expressed in the dimensionless form by:

$$\theta = \theta(\zeta, Fo, Bi) \quad (2.15)$$

According to Pountney et al. [8], the solution at $\zeta = 0$ ($z = 0$) of Eq. 2.12 under the boundary conditions given by Eq. 2.14 provides the analytic temperature evolution of the wall surface:

$$\theta_w = \frac{T_w - T_0}{T_f - T_0} = 1 - \exp(\chi^2)\text{erfc}(\chi) \quad (2.16)$$

where erfc is the complementary error function and χ is defined by:

$$\chi = Bi\sqrt{Fo} = h\sqrt{\frac{t}{\rho_{mat}k_{mat}c_{mat}}} \quad (2.17)$$

From Eq. 2.16 it is possible to evaluate the heat transfer coefficient knowing the material's physical and thermal properties (ρ_{mat} , k_{mat} , c_{mat}), the initial equilibrium temperature T_0 , the flow temperature step change T_f , and the time t when it is reached the wall temperature T_w . Therefore, it is of fundamental importance to know accurately the temperature indicated by the liquid crystal thermography at a precise temporal moment. Because of that, it is favourable to use the narrow-banded liquid crystals, which are calibrated in order to know the temperature when the green maximum intensity is reached.

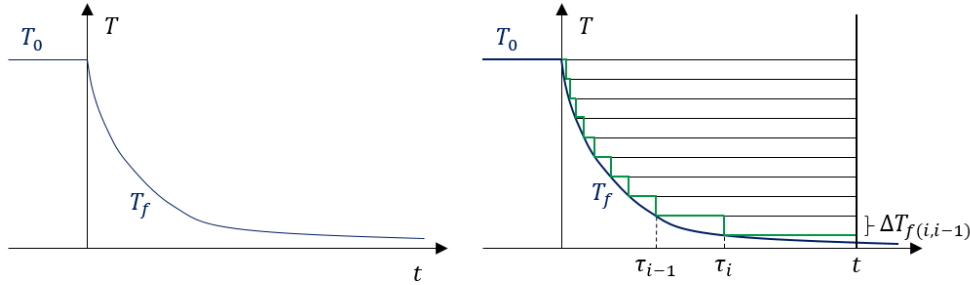


Figure 2.10: Discretization of fluid temperature variation in order to apply Duhamel's superposition theorem

The heat transfer coefficient cannot be analytically calculated by Eq. 2.16, so it is necessary to adopt an iterative method (e.g. Newton-Raphson method). In most experiments, the temperature change imposed on the airflow cannot be considered as an ideal step, therefore the solution in Eq. 2.16 is not directly applicable. As it was done by D.E. Metzger [36], a general temperature evolution can be approximated by a succession of N steps that take over at different times τ_i (as shown in Fig. 2.10) and the wall temperature evolution can be obtained by applying the Duhamel's superposition theorem:

$$T_w - T_0 = \sum_{i=1}^N [1 - \exp(\chi^2)\text{erfc}(\chi)] \Delta T_{f,(i,i-1)} \quad (2.18)$$

In Eq. 2.18, $\Delta T_{f(i,i-1)} = T_{f,i} - T_{f,i-1}$ and χ is now defined by:

$$\chi = h \sqrt{\frac{t - \tau_i}{\rho_{mat} k_{mat} c_{mat}}} \quad (2.19)$$

Owen et al. [38] shown how the uncertainties in transient heat transfer measurements with liquid crystals can be minimized by selecting the appropriate range of colour play. An experimenter should limit the dimensionless wall temperature range to:

$$0.3 < \theta_w < 0.7 \quad (2.20)$$

in order to have a good accuracy for the heat transfer coefficient evaluation.

Chapter 3

Experimental setup

3.1 Case description

The HTC measurements with different LCT approaches are performed on a simple case study, which is a simplification of an internal cooling passage of a turbine blade. The channel geometry is shown in Fig. 3.1 and its spatial orientation is reported in Fig. 3.2. The channel model has a magnification factor of about 20 that allows the accomplishment of detailed HTC spatially distributions, in similarity operating conditions. The channel has a length of 1000 mm with a constant square cross-section of $50 \times 50\text{ mm}^2$, which corresponds to a hydraulic diameter of 50 mm . At one side, 16 squared ribs are placed after the first 200 mm where the channel wall is smooth. The ribs are parallel with an angle of attack of $\varphi = 90\text{ deg}$, the blockage ratio is $e/D_h = 0.1$, and the rib pitch-to-height ratio is $P/e = 10$. The reference frame based on the channel has the x -axis perpendicular to the ribbed wall, the y -axis towards the stream-wise direction, and the z -axis parallel to the ribs. The model rotates with angular velocity Ω around the Z -axis, this axis belongs to the global reference coordinate system. The ribbed wall acts as trailing side when the rotation takes place. The channel geometry has been chosen to allow smooth implementations of both measurement approaches. Moreover, the selected geometry can be considered a good case study because its behaviour is rather documented in the literature.

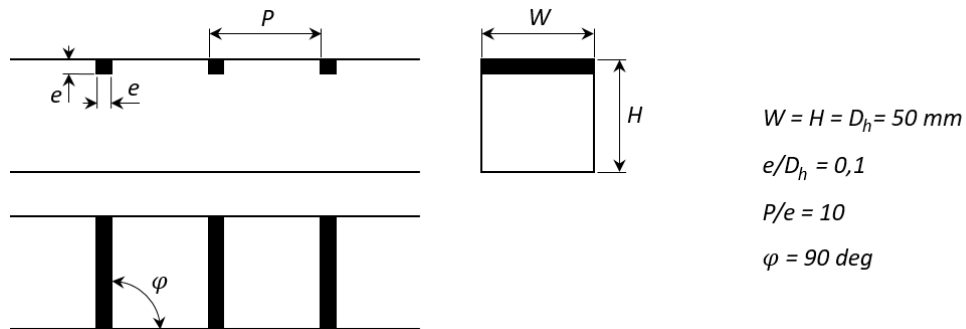


Figure 3.1: Main dimension of the ribbed channel model

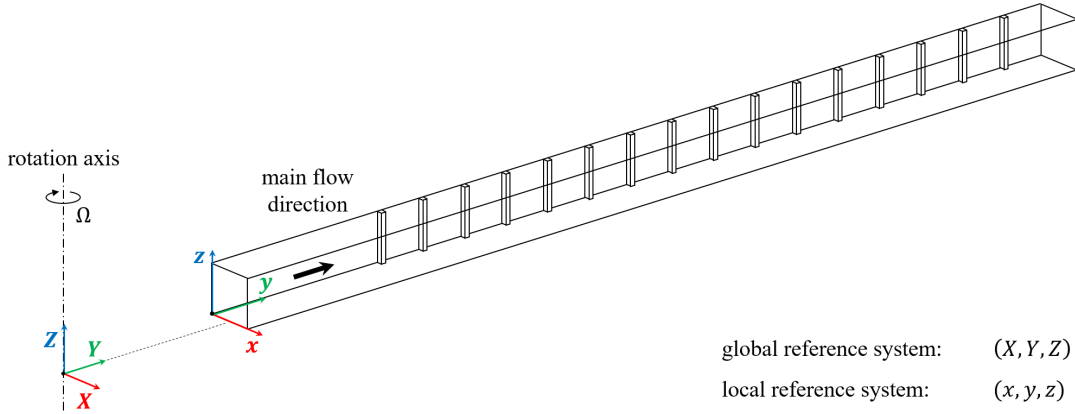


Figure 3.2: Test section relative coordinate system

Coletti et al. [9] and Casarsa et al. [7] performed flow field investigations by means of the PIV technique. Furthermore, in Çakan's work [6] the thermal performances of the static channel are studied with steady-state LC thermography and Mayo et al. [33, 35] apply the same measurement technique on a rotating channel with similar geometry.

The representative inlet conditions are set to Reynold number $Re = 20000$, and the measurements have been performed in both static $Ro = 0$ and rotating condition $Ro = 0.1 \div 0.3$. The nominal values of the representative test parameters are summarized in Tab. 3.1. The transient experiments require testing times of a few minutes, whereas the steady-state ones take several hours to reach a stable thermal conditions and therefore to perform the measurements. For this reason, the steady-state tests are carried out up to rotating condition of about $Ro = 0.2$. Otherwise, the long stay at a higher rotational speed would adversely impact on the electric motor that drives the rotation, which would overheat beyond its maximum allowable operating temperature.

Table 3.1: Test matrix of HTC evaluations with LC thermography approaches

| Re | 20000 | | | | | |
|--|-------|-----|------|------|------|------|
| Ro | 0 | 0.1 | 0.15 | 0.20 | 0.25 | 0.30 |
| Transient approach | | | | | | |
| Steady-state (1 heated wall) | | | | | | |
| Steady-state approach (3 heated walls) | | | | | | |

In addition to the general comparison between the two TLC techniques, different measurement setups are implemented within the two approaches. In the transient tests, two different liquid crystals with different starting temperature are employed in conjunction. Since the 2 colour transitions occur at different moments, the heat transfer can be assessed in two distinct times for each experiment. On the other hand, the steady-state approach requires the imposition of heat flux at the surface where the heat transfer has to be evaluated, therefore at least the ribbed surface should be heated in the current case (1 heated wall). This rep-

resents the common way to perform the TLC steady-state method. This work also starts the investigation of the effect of uneven wall heating conditions on the heat transfer, producing reliable experimental data useful to further numerical study aimed to analyse thermal and flow behaviour under multiple walls heating. Therefore, tests are carried out in which also the two sidewalls supply heat to the flow (3 heated walls). In any case, since steady-state and transient approach required different setup to perform the heat transfer evaluations, two different channel models have been built. Both channels have connecting flanges at either end that allow the installation on the same test facility. The channels are made of PMMA chosen for its relatively low cost, good machinability, and it is a material optically transparent, more lightweight, and more shatter-resistant than glass.

3.1.1 Channel model for transient approach

The channel model consists of four walls made of PMMA sheets 15 *mm* thick and PMMA ribs that are firmly glued to one wall. In order to exactly evaluate the heat transfer coefficients during the thermal transient tests, the PMMA thermo-physical properties have to be accurately known. For this reason, two material samples were sent to a specialized laboratory for match and analysis. The group of Materials Science and Technology of the University of Perugia [28] measured the thermal conductivity k and the specific heat c through differential scanning calorimetry, while the density ρ was indirectly calculated by weighting the samples and estimating the volume from their geometries. The analysis results are reported in Tab. 3.2. At this point, the thermo-physical properties and the wall thickness are used in Eq. 2.9 which gives maximum duration allowed to carry out the transient tests, estimated about 170 *s*.

Table 3.2: Material properties of PMMA

| | | |
|--------|-------|-----------|
| ρ | 1200 | kg/m^3 |
| c | 1250 | $J/(kgK)$ |
| k | 0.198 | $W/(mK)$ |

The thermal and flow field are expected to be symmetrical with respect to the median plane orthogonal to the ribbed wall, given the symmetry of the channel geometry considered. For this reason, two types of LC narrow-banded with different starting temperatures are applied in the two surface regions divided by the median plane. Regarding Fig. 3.3, the R13C1W Hallcrest LC mixture is sprayed on the lower region, meanwhile the R3C1W Hallcrest one on the upper area. In this way during any experiment, the evaluated HTC given by two kinds of liquid crystals can be compared between homologous locations.

The flow driving temperature is provided by the indications of 8 K-type thermocouples immersed in the core flow. They are located on the symmetry plane at distinct space positions reported in Tab. 3.3 to monitor the evolution of the flow along the channel. The thermocouples have the hot-junction diameters of 0.075 *mm*, which makes them suitable to measure sudden temperature variations.

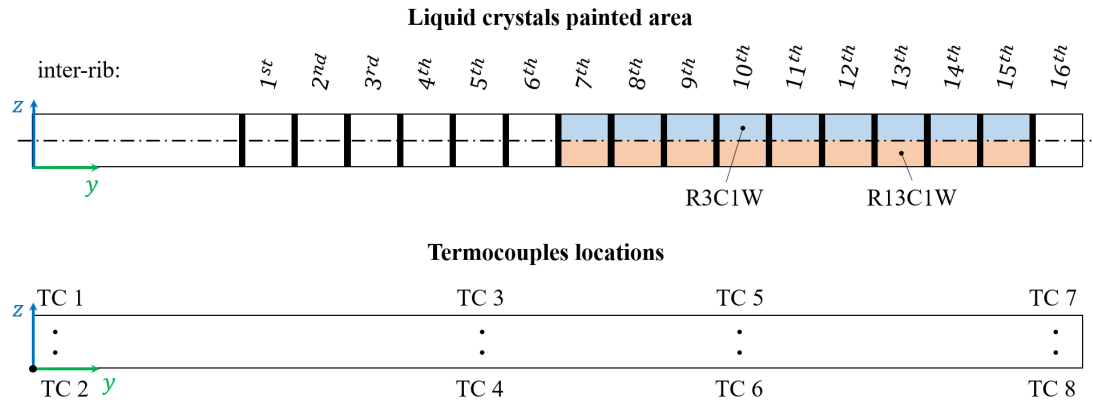


Figure 3.3: Liquid crystals painted surface (top) and locations of fluid thermocouples (bottom) for the transient channel model

Table 3.3: Location of the thermocouples immersed in the flow

| TC | y [mm] | z [mm] | TC | y [mm] | z [mm] |
|----|-------------|-------------|----|-------------|-------------|
| 1 | 25.0 | 33.4 | 5 | 680.0 | 16.6 |
| 2 | 25.0 | 16.6 | 6 | 680.0 | 33.4 |
| 3 | 440.0 | 33.4 | 7 | 975.0 | 16.6 |
| 4 | 440.0 | 16.6 | 8 | 975.0 | 33.4 |

The low inertia of the hot-junction indeed ensures high speed of response, avoiding the negative impact of measuring lag. Because of the minute size and low stiffness of thermocouples, they are inserted in thin plastic tubes that are used as supports to keep them in position, as illustrated in Fig. 3.4.

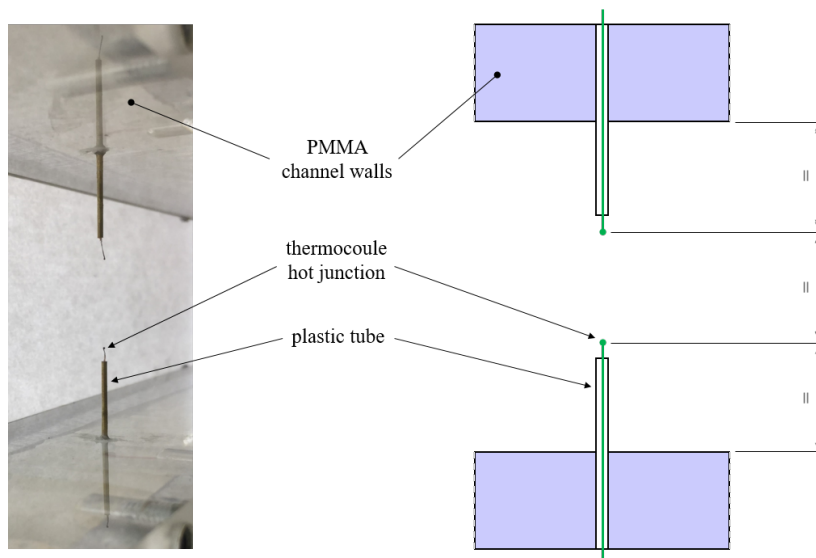


Figure 3.4: Detail of the fluid thermocouple installation

3.1.2 Channel model for steady-state approach

The channel is formed by PMMA walls of 12 mm thickness, which can be disassembled to ease the heater foils installation and the liquid crystals deposition. Three $25\ \mu\text{m}$ thickness equal foils made of Inconel alloy 665 provide the required heat flux. They are attached on the ribbed and the two neighbouring walls by means of an adhesive layer, then the PMMA ribs are set on Inconel surface. The Inconel material is chosen because the temperature does not strongly affect the electrical resistivity and it is commercially available in thin sheets. Indeed, the Inconel electrical resistivity varies by $0.1 \div 0.2\%$ every 10°C in the test operating temperature range (Appendix A). The heater elements have 48 mm of width compared to an internal channel dimension of 50 mm to give gaps, hence avoid electrical contact between the foils installed on adjacent walls. Copper bars strongly soldered at both ends of each foil helps to uniformly distribute the electrical current, thanks to the high electrical conductivity.

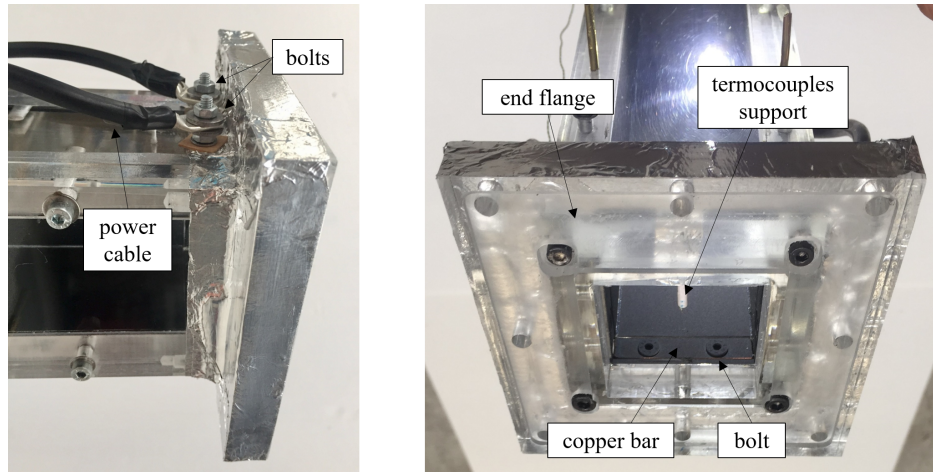


Figure 3.5: Inconel foils location and connection

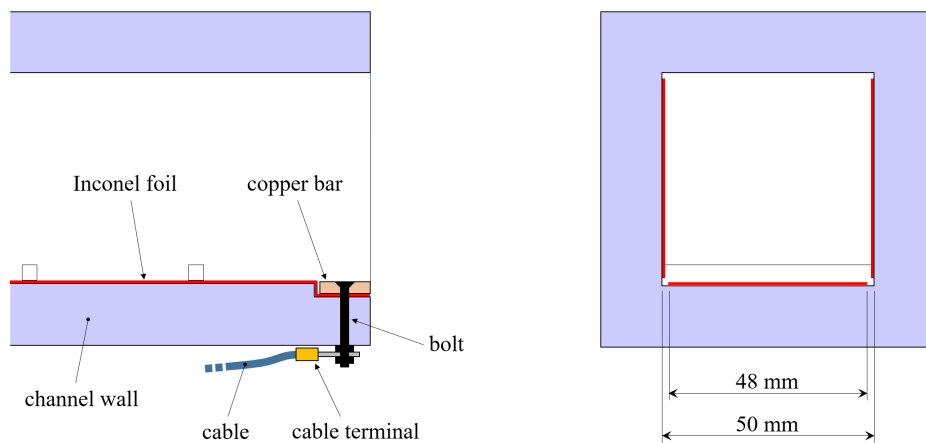


Figure 3.6: Inconel foils location and connection

The bars are secured by bolts into niches, milled in the channel walls, so that they are at the same level of the internal surfaces, as showed in Fig. 3.6. The bolts are externally connected at the power cables to fed the heater elements.

The heater sides of the channel are externally covered by a 50 *mm* layer of polyurethane to minimize the conductive heat losses. Two K-type thermocouples monitor the outer surface temperature of the thermal coat.

All Inconel surfaces are stained with black paint that reduces reflections and brings out the liquid crystals colour. Fourthly, the ribbed walls are wholly sprayed with R35C7W Hallcrest liquid crystals, which nominally presents a starting temperature of about 35°C and a bandwidth of about 7°C.

The inlet and outlet temperature conditions of the flow are taken by two K-type-thermocouples, which are installed in the centre of the respective channel section in a similar manner as done for the thermocouples of the transient channel.

3.2 Test facility

The Energy and Environmental Engineering Laboratory of the University of Udine has a test facility by which is possible to accomplish detailed aerothermal performances of internal cooling system models of the gas turbine blade.

Its first version dates back to 2010, and then it has been notably developed over the years. Initially, it has been developed the methodology to investigate the flow field inside rotating test sections by means of particle image velocimetry operated in the phase-locked mode: the measurement system is kept fixed and it is synchronized with the periodical passage of the test section [3]. This allowed performing PIV flow field measurements inside a smooth trailing edge cooling passage under static and rotating conditions, in which the coolant enters the passage at the blade hub and it is exhausted at both the tip and at the trailing edge [4]. Then a new channel configuration provided with inclined ribs was equipped on the test facility and analyzed, extending the previous results and providing an overall review of the aerothermal performance of the considered passage [37]. After that, the test facility was upgraded by replacing the electric motor and making improvements to the loading structure. The focus was moved on the characterization of the flow in a rotating smooth radial channel with a triangular-shaped cross-section, pertaining to the leading edge passage of a gas turbine blade [42]. Perpendicular ribs were placed on both leading and trailing sides of the channel with the aim to investigate the interaction between the effects of rotation and those induced by turbulence promoters [15]. Moreover, it was possible to achieve the characterization of the flow field inside a leading-edge cooling channel characterized by multiple internal impinging jets [16]. The last facility upgrade ahead of the current thesis was done in 2016 in order to allow rotating test for heat transfer measurements on internal cooling passages [39]. Spatially resolved heat transfer data were performed through transient thermochromic liquid crystals technique on realistic multi-pass geometry in static and rotating conditions [40]. However, at that time the test procedure was just been developed and a lot was still to be done to verify data accuracy.

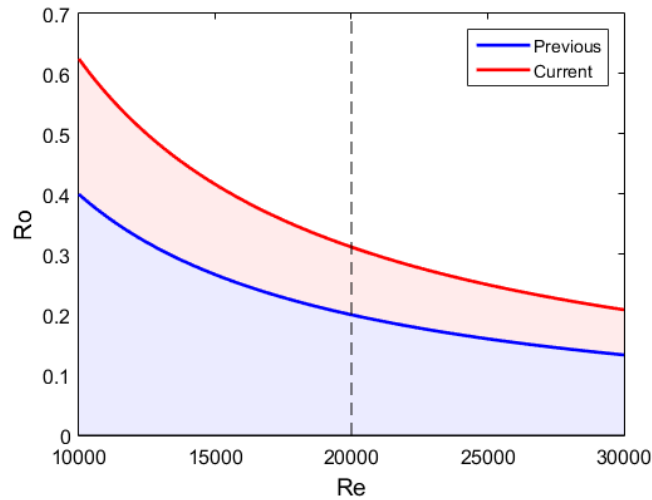


Figure 3.7: Comparison of operational range between the previous and the present facilities

The current thesis work developed the last update of the test facility, which has mainly made possible to reach higher rotation number and to ensure greater structural stability. Figure 3.7 proposes the operational range comparison between the previous and the present facilities, with reference to a hydraulic diameter of the test section of 50 mm . Others significant upgrades have been made on the test facility to improve the management of the experiments and the accuracy of the data acquired, as it will be clarified in the following.

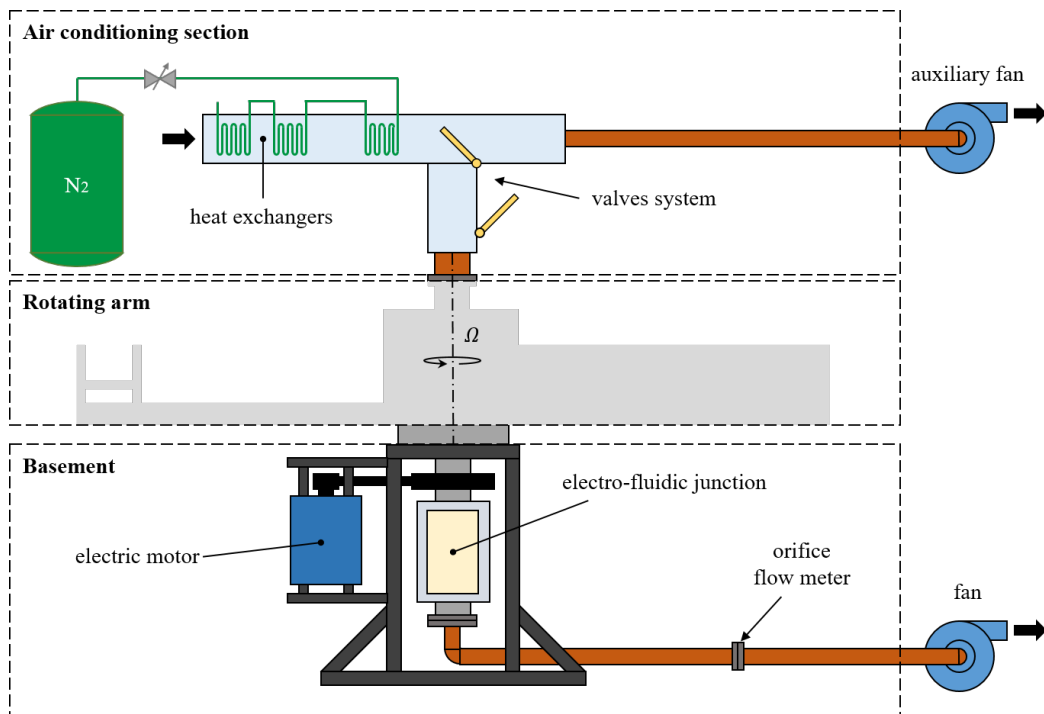


Figure 3.8: Test facility sketch

As shown in Fig. 3.8, three main sections of the test facility can be identified; starting from the ground: the basement, the rotating arm, and the air conditioning section. The air is treated by the air conditioning section only during the transient tests, otherwise is taken directly from the ambient for the steady-state measurements. The flow is forced into the channel model and then it leaves the rotating arm, passing through the electro-fluidic junction installed in the basement. The air is sucked out by a six-stage centrifugal fan, located downstream the flow measurement.

For the sake of clarity, each facility section and their functions will be explained in detail in the following paragraphs. Moreover, the control systems and other secondary equipment will be described.

3.2.1 The basement

The basement consists of a frame of extruded steel tubes that are welded together. It is constrained to the ground through bolts and performs the function of loading structure: it supports the rotating arm and transmits static and dynamic loads to the ground, which are generated by the rotation of the arm. An electric motor with a maximum power of 11 kW drives the arm rotation through a transmission belt, looped over the arm pulley. The electric motor is bolted on a support structure that can slide on two fixed guides. Thanks to the guides, the horizontal position of the electric motor can be adjusted ensuring the correct tension of the transmission belt. The driven pulley is keyed on the hollow shaft, which is integrally connected to the rotating arm. The shaft is hollow so that the process fluid coming from the rotating test section can pass through it.

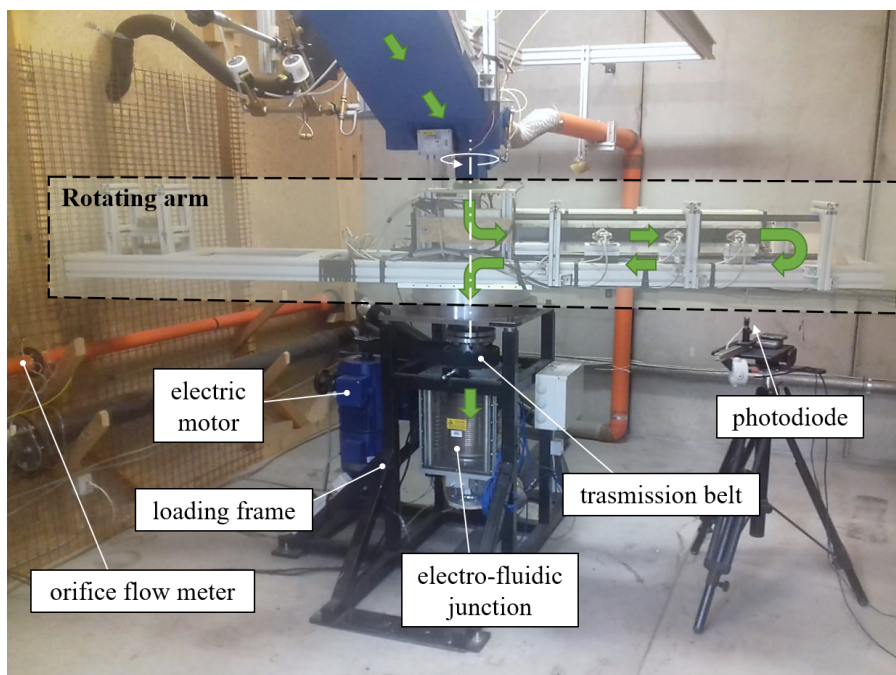


Figure 3.9: Test facility with the main basement items

An electro-fluidic joint completes the basement and it ensures the electrical and fluid connection between the stationary and rotating parts. It has 32 slip rings that give the electrical supply and signal connection for the rotating arm; moreover, connects the rotating hollow shaft and the stationary air pipeline employing a seal.

3.2.2 The rotating arm

The rotating arm must have a structural frame that withstands at the high mechanical stress arising during the rotation and safely ensures the channel model, the onboard instruments, and the other additional elements that compete in order to carry out the experiments.

The frame is formed by commercial extruded aluminium profiles that are joined by threaded insert connections. The rotating arm is constrained to the basement frame by the slewing bearing, which allows the arm to rotate and it remains sturdy even in the case of severe rotational imbalances. The slewing bearing is a kind of rolling bearing typically installed in conventional cranes.

The airflow enters along the rotation axis and has to turn of 90-degree to get into the channel model that is installed on one side of the rotating arm. A settling chamber feeds the test section in a way that avoids the flow field distortions that would be introduced by a simple 90-degree pipe. The air runs inside the test section and then is collected by the returning pipeline, which conveys the airflow into the hollow shaft to discharge it from the rotating arm.

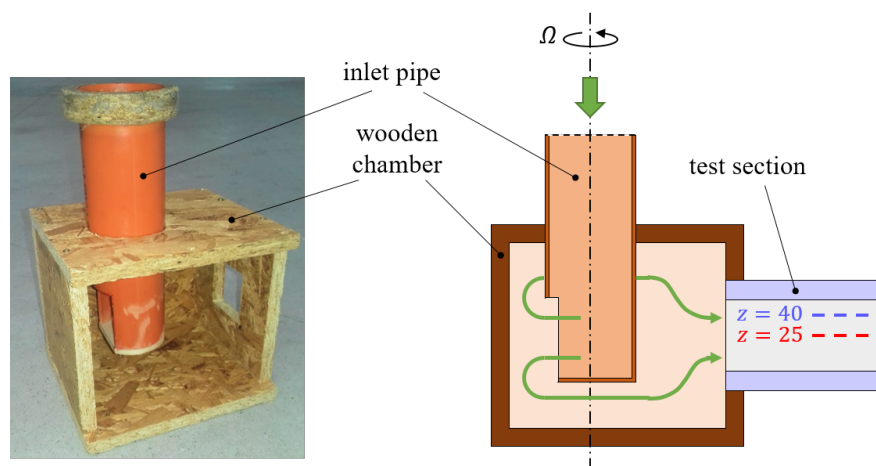


Figure 3.10: Settling chamber sketch (right side) and its photo during the assembly phase (on left)

Figure 3.10 illustrates what the settling chamber looks like: the inlet pipe ends inside a wooden cavity and, opposite to the wall where the test section is inserted, an opening is housed in the tube. The inlet conditions resulting from the settling chamber were verified by means of the PIV technique implemented in static and rotating conditions. The flow fields were investigated in two planes parallel to the $X - Y$ plane: at 25 mm and 40 mm .

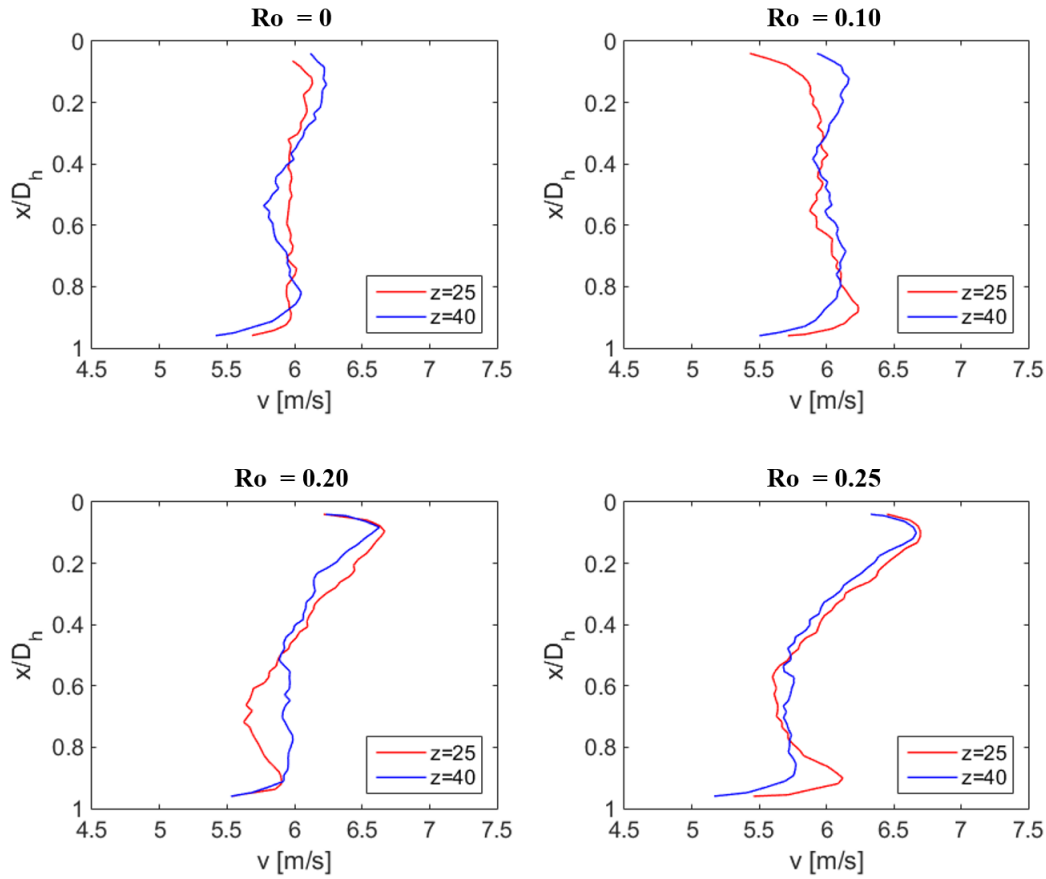


Figure 3.11: Velocity profiles of the inlet flow

The measured inlet conditions are given in Fig. 3.11, which collects the velocity profiles extrapolated 100 mm downstream the channel inlet. Almost flat velocity profiles occur at low Rotation number. In the regions near the walls, the air-flow velocity then grows with increasing angular speed as a consequence of the secondary vortices that are developed by the rotation. These measurements ultimately prove the good flow field at the inlet of the channel resulting from the use of the settling chamber.

Onboard instrumentations

The acquisition system that is on board the rotating arm has the tasks to acquire the images of liquid crystals evolution, to scan the thermocouples that provide the airflow temperatures, and to send all the collected data to an on-ground computer. Figure 3.12 presents the components wiring scheme.

A correspondence between images and thermocouple readings is required in order to accurately evaluate the heat transfer coefficients during transient approach tests. Any bias on the acquisitions would lead to an erroneous reconstruction of the surface and fluid temperatures evolutions. The NI myDAQ unit generates a trigger signal of 25 Hz frequency to synchronize the two acquisitions.

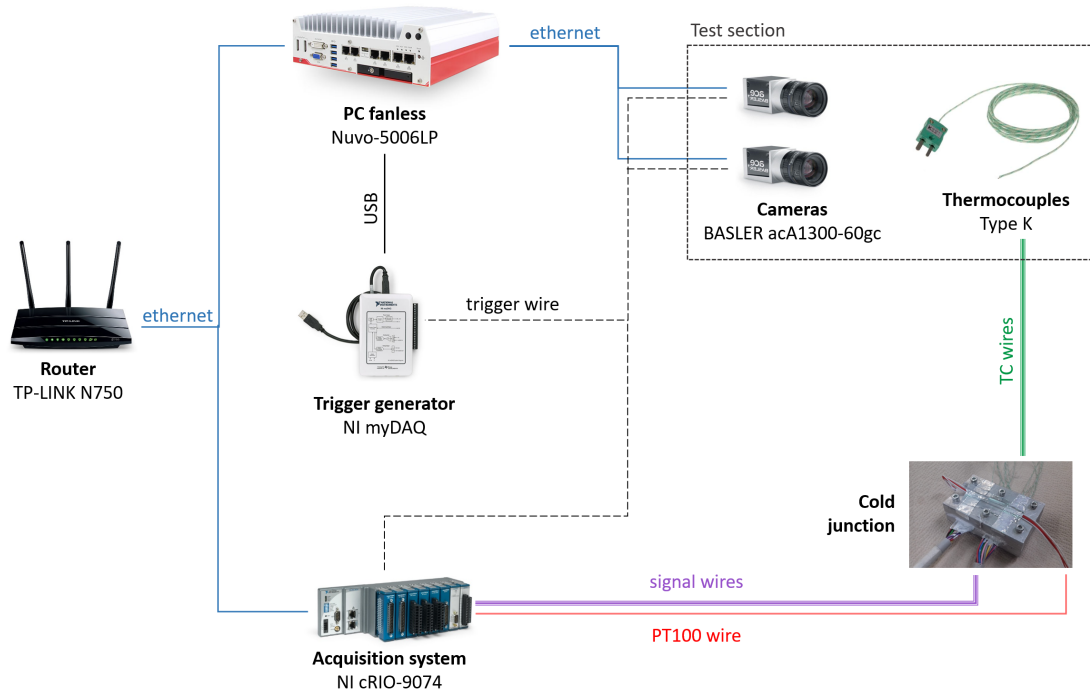


Figure 3.12: Onboard data acquisition system

The fluid temperature achievement is demanded to the NI cRIO-9074 device equipped with three modules. Thermocouple signals are read by means of the NI 9213 module and the NI 9217 module acquires the reference temperature to perform the cold-junction compensation. The last module NI 9401 reads the trigger signal and determines the temperature acquisition.

The following key features of the image recording equipment are required:

- The overall dimensions of the cameras have to be as small as possible to minimize the weight to carry on the rotating arm. Furthermore, the cameras must tolerate the forces caused by the rotation;
- The short distance between the channel model and the cameras leads to the use of wide-angle lenses;
- The overall field of view of the cameras shall extend at least 9 inter-rib of the channel;
- The frame grabbing has to be triggered in order to be synchronized with temperature data;
- A large amount of recorded data must be stored in real-time in a memory device without loss of information;
- The framed surface of interest has to be properly illuminated avoiding shadows, reflections, image saturation, and any other factor that would affect image quality.

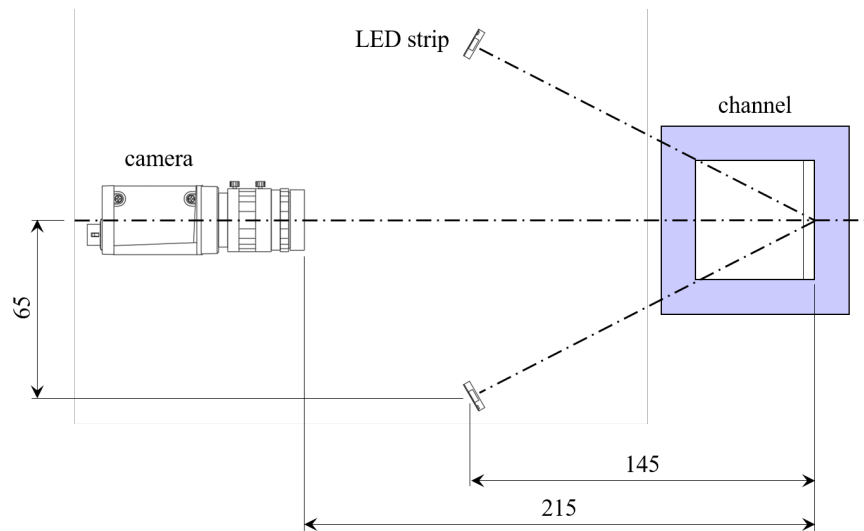


Figure 3.13: Relative position of the vision system items

These requirements are met with two BASLER acA1300-60gc camera with the NAVITAR $6\text{ mm } 1:1.4\text{ C } 1/2''\text{ M}30.5$ camera lens, while a Nuvo-5006LP fanless computer deals with the storage of the acquired images and runs the control camera software developed in LabVIEW. The cameras are connected via Ethernet cables to the computer, which has dedicated network cards up to four cameras. Two led stripes 1 m of length with 120 led/m , 24 W/m , and 4000 K of colour temperature determine the illumination of the liquid crystals painted surface. The two stripes are aligned parallel to the channel model and Fig. 3.13 shows the relative position of the items that compose the vision system setup.

The NI cRIO-9074 device and the fanless computer transfer the entire acquired data to an on-ground computer via a networking device. Two TP-LINK N750 routers implement the wireless local area networking of the onboard system and the on-ground computer. The on-ground computer is also used to control and monitor data acquisition. The thermocouples acquisition device, the router, and particularly the fanless computer are installed as close as possible to the rotation axis to minimize the magnitudes of centrifugal forces, hence preventing any possible failure.

Weight balance procedure

The static and especially the dynamic stability of the whole arm are guaranteed to carry out the rotating tests in safety conditions and avoid critical stresses, which would cause damage or even failure of the test facility. Of course, the balancing phase is done before to put in service the test facility. Several metal plates are installed on the opposite side of the test section properly, and they play the role of counterweight. In order to perform the counterweight determination, the masses and locations of all the components are registered during their installation on the rotating arm. Then a faithful tridimensional virtual model is created using the commercial software SolidWorks (Fig. 3.14).

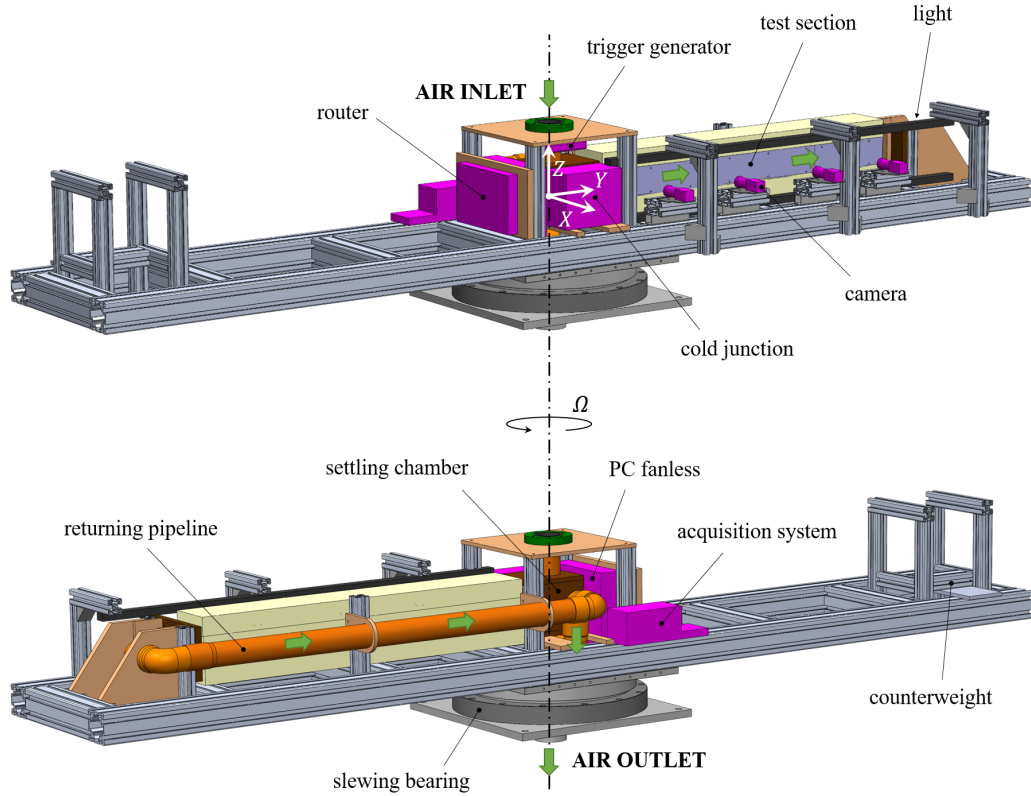


Figure 3.14: Virtual model of the equipped rotating arm

Thanks to the virtual model, the position (X_{cw}, Y_{cw}, Z_{cw}) and the mass m_{cw} of the counterweight are estimated through the following equations:

- *Static balance*: balance of turning forces acting along the direction of the gravity acceleration vector (Z -axis):

$$\sum_{left} (m_i g) Y_i + (m_{cw} g) Y_{cw} = \sum_{right} (m_i g) Y_i \quad (3.1)$$

$$\sum_{left} (m_i g) X_i + (m_{cw} g) X_{cw} = \sum_{right} (m_i g) X_i \quad (3.2)$$

- *Dynamic balance*: balance of turning centrifugal forces generated by the rotation:

$$\sum_{left} (m_i \Omega^2 Y_i) Z_i + (m_{cw} \Omega^2 Y_{cw}) Z_{cw} = \sum_{right} (m_i \Omega^2 Y_i) Z_i \quad (3.3)$$

The three equations (Eq. 3.1, 3.2, and 3.3) compose an algebraic systems that can be solved in the four unknowns $(X_{cw}, Y_{cw}, Z_{cw}, m_{cw})$ choosing the value of one unknown and consequently evaluating the others.

Once the counterweight configuration is defined, the actual balancing of the system under rotation has to be verified. Two optical systems provide the qualitative estimation and quantitative evaluation of the proper balance procedure.

An on-ground colour camera frames the rotating arm, in which a black target is glued on one of the short sides of the rotating structure, as shown in Fig. 3.15. It is possible to evaluate the effectiveness of the counterweight by analyzing the video recorded during low-speed rotation: the black target must always be at the same height at each passage in front of the camera.

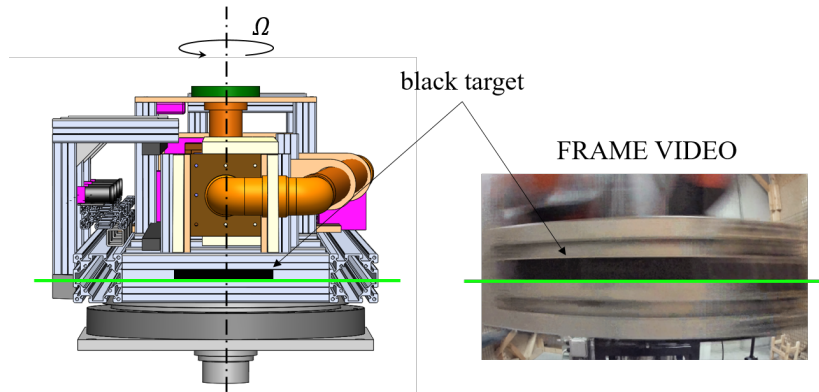


Figure 3.15: Qualitative estimation of rotating arm diplacements

Once the qualitative test is passed, the balance verification procedure continues at higher rotational speed monitoring the basement shifts. A laser system coupled with the high sensitivity camera 'Sensicam PCO' allows to measure the displacements. The laser system emits a horizontal light plane that strikes the upper metal plate of the basement structure. Consequently, the reflection outlines the corner profile of the metal plate (Fig. 3.16). The shifts in two orthogonal directions are derived through the post-processing of the images recorded by the camera. Moreover, they are correlated with the angular positions of the rotating arm because the camera acquisitions and the rotation frequency are in synch.

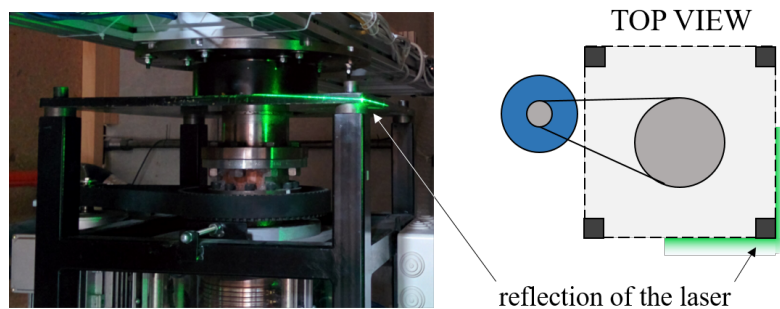


Figure 3.16: Basement corner displacements evaluation through the laser system and high-sensitive camera

The experience attests that the creation of a detailed and accurate virtual model leads to set a precise weight and location for the counterweight. However, the latest optical system allows to refine the counterweight configuration.

3.2.3 The air conditioning section and the heater foil supply system

In the transient LC thermography experiment, as the name implies, a thermal transient state has to be established. Since in the real cooling schemes the coolant temperature is below that of the channel walls, a forced negative variation of the flow temperature is required during the tests. In other words, the airflow undergoes a sudden cooling to satisfy the similarity operating conditions. This goal is achieved by using the air conditioning system, which is immediately above the rotating arm and it is shown in Fig. 3.17.

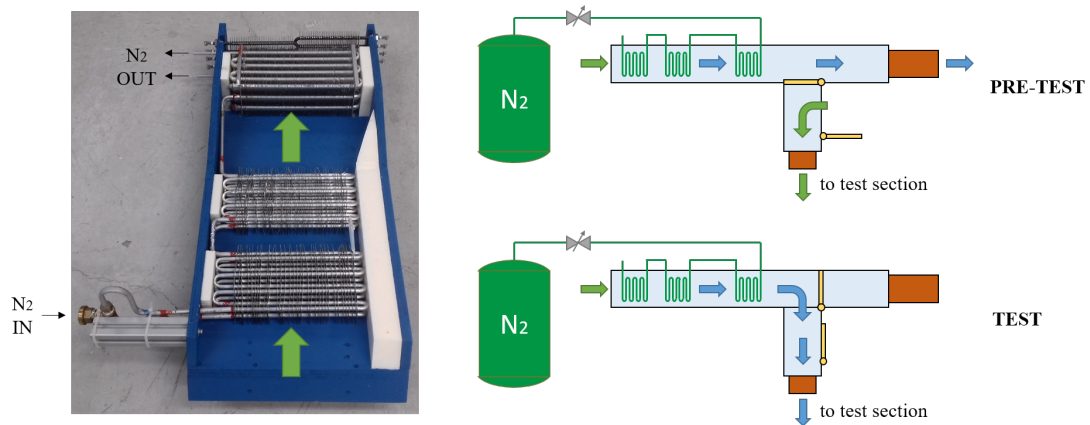


Figure 3.17: Nitrogen-air heat exchangers (left side) and valves system operating scheme (right side)

The air conditioning section is composed of a series of air-nitrogen heat exchangers used to cool down the ambient air and of two valves that allow operating in two different modes, which correspond to the two main phases of the transient test:

- *Pre-test phase.* Air at room temperature is routed into the channel model to maintain the isothermal condition with it. Meanwhile, an auxiliary fan sucks air through the heat exchangers in order to reach the target conditions for the experiments, monitoring the temperature at heat exchange outlet. The airflows that run in the two circuits have the same flow rate.
- *Test phase.* When the desired condition of the airflow is reached, the two valves are switched and the auxiliary fan is turned off. Consequently, the cooled air coming from the heat exchangers is sent to the channel.

The choice of a nitrogen-based cooling system instead of a more conventional chiller units has to be found in the wider range of working conditions, easily achievable with lower cost. The drawbacks are the customized system that has to be designed and the necessity to manage the liquid nitrogen.

A liquid nitrogen reservoir supplies the heat exchangers and a needle manual valve adjusts the flow rate. A remotely controlled gate valve allows to shut down the delivery of coolant at any time. The nitrogen phase transition commonly

occurs across the heat exchangers and the resulting gas is discharged inside the very large volume of the laboratory. A solenoid valve toggles the butterfly valves that are pneumatically driven. The shutters of the butterfly valves are wooden plates that rotate around an edge, obstructing the air passage. Fig 3.18 reports two accomplished temperature evolutions at the channel inlet. These temperature profiles are achieved by the set of different parameters of the air conditioning system, such as different nitrogen flow rates and outlet heat exchangers' temperatures.

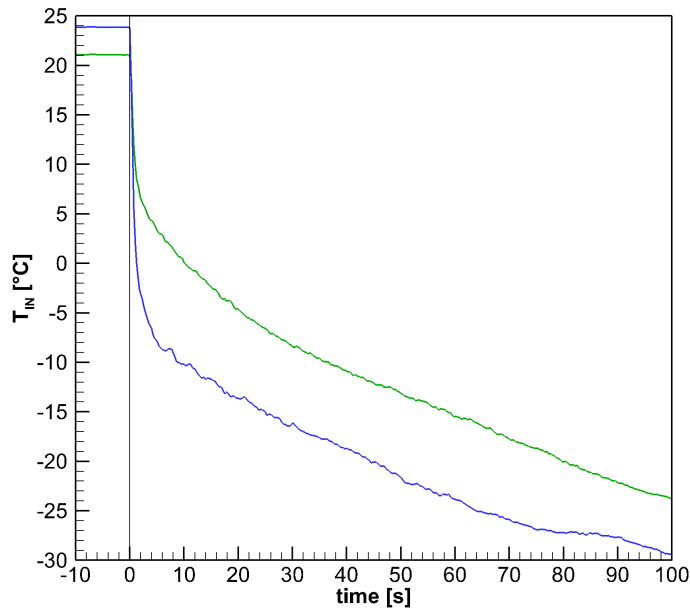


Figure 3.18: Example of inlet temperatures achievable

The cooling system is bypassed when the steady-state LC thermography is performed because there isn't demand for cooled air, and ambient air flows inside the test section. As stated in Par. 3.1.2, three Inconel foils provides the necessary surface heat flux. The heater foils are fed by a DC power supply, which has a maximum output power of 2400 W (up to an electrical voltage of 16 V and an electrical current of 150 A). The power supply is located in an on-ground cabinet and the power cables pass through the electro-fluidic junction. The three foils are electrically connected in parallel for a twofold reason. Firstly, the supplied elements can be selected acting on switches without changing the wire connections. The second reason is the limited voltage capacity of the DC power supply.

An onboard voltmeter continuously measures the voltage drop across the heater foils, thereby the power supplied is monitored and can be remotely regulated during the test. Preliminary, the uniform electric potential of the copper bars has been verified and the electrical resistance of each heater foil have been measured. The measures prove that the foils have equal electrical resistance, hence in the three circuit branches will pass the same current. Therefore, the same power will be dissipated for each heater.

3.2.4 Control system

In order to correctly accomplish the heat transfer evaluations, the control system has the following tasks:

- To set, monitor and, regulate the reference Reynolds number Re^* and rotation number Ro^* , in all the tests;
- To monitor the outlet heat exchanger temperature T_{HE} and control the butterfly valves, in the tests with the transient thermography;
- To monitor the voltage drop across the heater foils ΔV and set the electric power supplied, during the tests carried out with the steady-state approach.

Figure 3.19 gives a general overview of the control system. Several NI modules plugged in the NI cDAQ-9178 support acquire all the raw data and generate the output control signal. The NI cDAQ device is connected to the on-ground computer, where an in-house developed LabVIEW software is installed to monitor, elaborate, and set the output feedback signals.

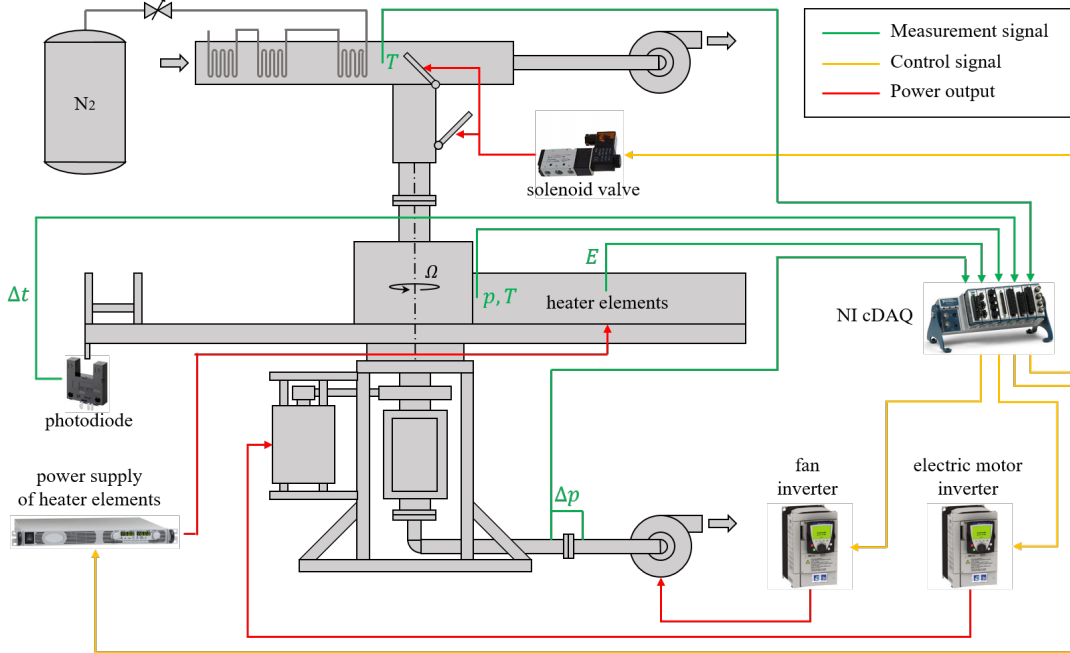


Figure 3.19: Diagram of the control system connections

Reynolds and rotation number control

The experiments are defined by the two main parameters evaluated in the inlet section of the channel model, which are the Reynold number and the rotation number. Their definition formulas are rewritten for the reference section, indicated with the superscript (*), as:

$$Re^* = \frac{\dot{m}}{\mu^* D_h} \quad Ro^* = \frac{\rho^* \Omega D_h^3}{\dot{m}} \quad (3.4)$$

From Eq. 3.4, the reference Reynolds and rotation number can be experimentally evaluated knowing:

- the test section geometry (D_h);
- the channel inlet air condition (ρ^* , μ^*);
- the air flow rate that runs through the channel (\dot{m});
- the angular speed of the rotating arm (Ω).

The air dynamic viscosity and density depend on the channel inlet temperature and static pressure. The viscosity is a function of the temperature as provided in Eq. A.2 of Appendix A, while the density is calculated by applying the ideal gas law:

$$\rho^* = \frac{p^*}{R_{air}T^*} \quad (3.5)$$

An onboard differential pressure transducer is connected to a pressure tap drilled in the channel wall and it allows to evaluate the static pressure at the inlet. Meanwhile, a K-type thermocouple immersed in the core flow provides the intake air temperature.

The orifice flow meter located upstream the fan provides the air mass flow rate. According to the ISO 5167-2 international standards [23], the mass flow is calculated on the based of the density and the pressure drop across the orifice, which is measured by a calibrated capacitance differential pressure transmitter.

An on-ground tripod holds s photodiode and at one end of the rotating arm is located a metal plate. At every revolution, the metal plate acts as a shutter for the photodiode. The PXI-6608 high-precision NI module samples the photodiode signals to time the period Δt , hence the angular speed can be calculated just once a time at revolution using the well-know relation:

$$\Omega = \frac{2\pi}{\Delta t} \quad (3.6)$$

The Reynolds and rotation number can be varied by using two power inverters: one runs the electric motor of the rotating arm, the other drives the fan motor hence determines the flow rate.

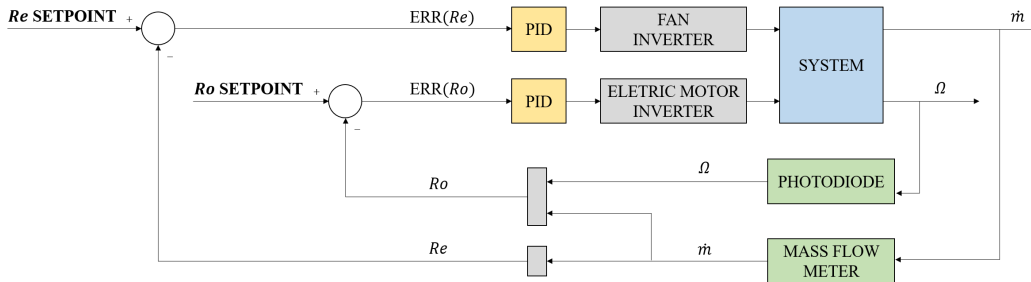


Figure 3.20: Close loop control

The two dimensionless parameters have to be kept constant throughout the experiment. This is quite simple to accomplish for the HTC measurement with a steady-state approach, conversely when is used the transient approach. In thermal transient tests, the air temperature change causes the time-variation of inlet condition. In addition, the Reynold and rotation number can't set independently to each other because they have common dependence terms in their definitions. To overcome the problem, a close-loop control has been implemented as reported in Fig. 3.20. The control loop consists of two PID controllers that automatically applies the responsive correction to the inverter power frequencies in order to adjust the Reynolds and rotation numbers. In a preliminary phase, the proportional, integral, and derivative gains of both PID controllers were tuned to have an accurate dynamic response without any danger instability. Figure 3.21 presents a typical behaviour of the test parameters of an HTC measurement with transient approach. As it can be seen, the Reynold and rotation number are always very close to the setpoint despite a small overshoot right after the testing start, which is caused by the sudden inlet temperature change. For all the experiments the amplitudes of the overshoots are always within the 1% of the setpoint values.

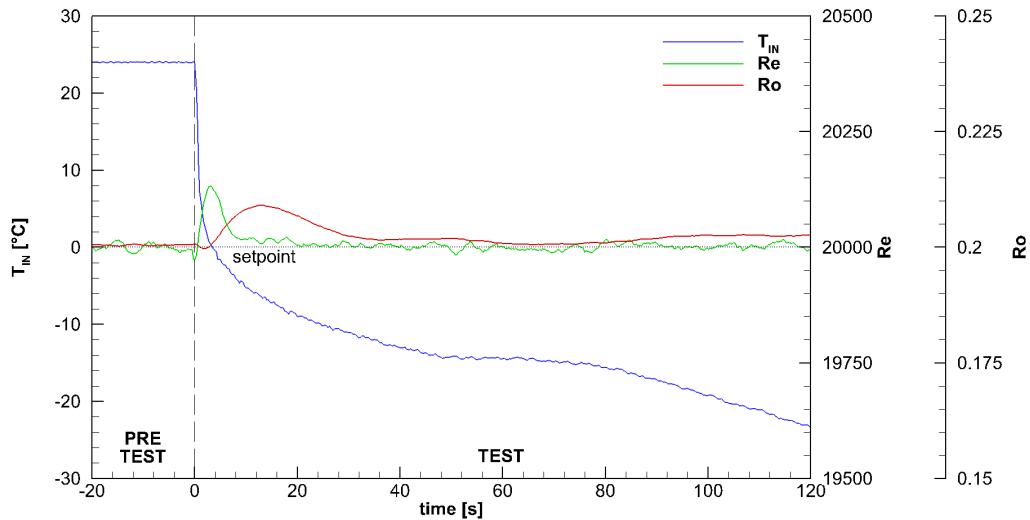


Figure 3.21: Trends of the main parameters during a transient test

Other test parameters control

The remaining parameters to monitor and control are those specific to the measurements approach used:

- *Transient thermography*

The control system allows monitoring the flow condition outcoming from the air conditioning section. A thermocouple located downstream the last heat exchange provides the temperature information T_{HE} during the pre-test phase. The pre-test phase starts with the opening of the gate valve of the liquid nitrogen, and the airflow is consequently cooled. When the air

temperature falls below a setpoint temperature defined by the experimenter, the control switches the pneumatic solenoid valve that toggles the butterfly valves and starts the test phase. Once the transition of the liquid crystal occurs all over the investigated surface, the butterfly valves return to the initial position, and the gate valve shuts down the nitrogen supply.

- *Steady-state thermography*

The number of the heater foils powered is manually selected by acting on the electrical switches, before the start of any test. The experimenter set the first attempt value for the power and then waits for the channel warming. The eventual rotation takes place after that. The thermal condition of the channel is continuously evaluated on the base of the images acquired by the cameras. The steady-state condition is reached when the liquid crystals colours shall be considered stable in the space for at least a 10-minute interval. The power can be remotely adjusted in order to have the liquid crystals optically active in the desired location. The heat dissipated P_{joule} is calculated by the voltage drop E across the Inconel foils measured during the rotation:

$$P_{joule} = \frac{E^2}{R} \quad (3.7)$$

where R is the total electrical resistance of the heater elements.

3.3 Calibration facilities

The heat transfer measurement approaches used in this work required different types of liquid crystals. The steady-state thermography employs wide-banded LC, while narrow-banded LC gives the temperature indications in the transient thermography. Anyway, a preliminary liquid crystals calibration procedure is required to correlate the colour displayed to the temperature at which they are. The temperature for which the maximum intensity of the green colour is reached (peak intensity temperature) has to be accomplished for narrow-banded LC; while a continuous relationship between the temperatures and the colour hue information is needed for wide-banded LC.

A first calibration facility can carry out both calibration types by means of the temperature gradient approach. In this calibration setup, the liquid crystals undergo a stable temperature spatial distribution that reveals all their colour change (temperature gradient approach). Then the desired calibration can be obtained depending on how the acquired image is post-processed. A significant amount of waiting time is necessary to attain steady-state conditions (about 2-3 hours), hence the calibration through this approach is a time-consuming practice. Moreover, it implies also long stay in the liquid crystals colour activation range, which could lead to problems including alterations or rapid ageing of the liquid crystals. A second calibration facility was developed to overcome the significant time spent on the previous one, and on the other hand to provide a further independent calibration procedure. The new setup firstly cools down the liquid crystals and then

brings them back to the starting temperature within about 35 minutes. In this method, named temperature evolution approach, the liquid crystals colour transition occurs over time. Only the liquid crystals used in the transient thermography has been calibrated in this latter facility.

3.3.1 Temperature gradient approach

The facility is sketched in Fig. 3.22 and mainly consists of a rectangular aluminium slab of $600 \times 150 \times 3 \text{ mm}^3$, on which the liquid crystals are sprayed on the top surface that is previously painted black. Two Peltier cells set different temperatures at the slab ends, hence establish a stable and almost one-dimensional temperature gradient. The cold sides of the Peltier cells are in contact with aluminium, and at the same time, two water exchangers remove heat from the hot sides. The slab is thermally insulated: expanded polyurethane covers the bottom and lateral sides to minimize conduction losses; also a PMMA plate of 15 mm of thickness avoids the natural convection from the upper surface. All around the PMMA plate, there is a continuous shim to maintain a 1 mm gap of still air, that avoid the contact of the plate with the aluminium slab. Along the centre-line of the metal slab, 12 K-type thermocouples equally spaced are acquired by the Agilent 34970A system to find out the resulting temperature profile. The thermocouples are housed in blind holes, with a diameter of 1 mm and 2.75 mm depth, filled with a conductive paste. The vision system is similar in components, relative distance, and illumination to the one installed on the rotating arm. This way prevents possible calibration errors or issues related to the different viewing angle and illumination.

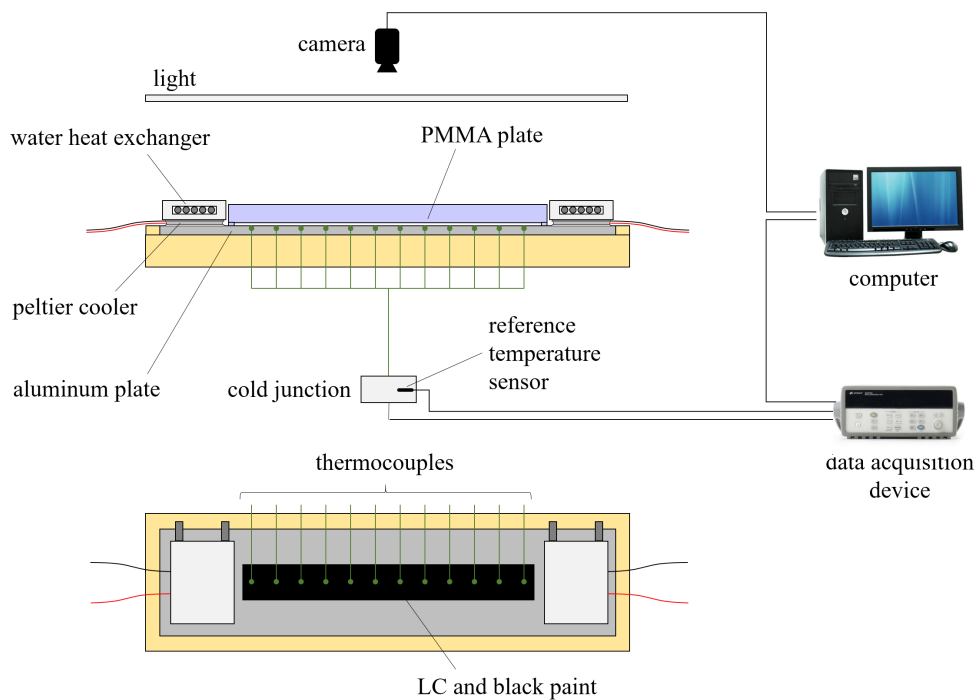


Figure 3.22: Calibration facility sketch, for temperature gradient approach

3.3.2 Temperature evolution approach

A frame made of PMMA presses a copper plate $35 \times 35 \times 4 \text{ mm}^3$ on an aluminium basement through 8 bolts, as illustrated in Fig. 3.23. A removable PMMA window allows the optical access and simultaneously reduces the natural convection. The liquid crystals are painted on the top surface of the copper plate.

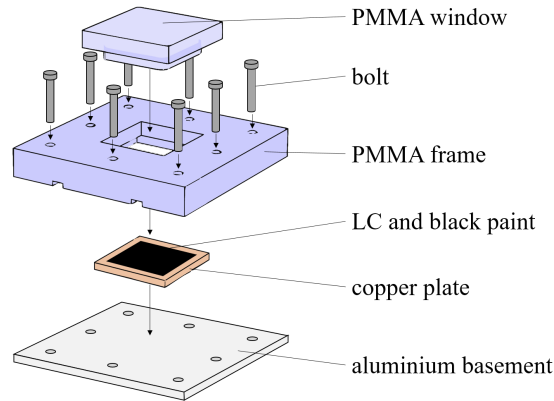


Figure 3.23: Calibration plate for the temperature evolution approach

A water heat exchange located just below the aluminium basement performs the required cooling rate and the successive warming of the copper plate. The heat exchange is part of a water closed circuit, where the mass flow ratio is maintained constant and a Peltier cell regulates the water temperature that enters in the heat exchanger. The Agilent 34970A system acquires the signals of two K-type thermocouples to monitor the copper surface temperature, hence the liquid crystals one. A thermocouple is situated onto the painted surface, and the other one is inserted in a blind hole with 0.5 mm of diameter in the opposite side. The hole is drilled to such a depth that the thermocouple is 0.25 mm just below the top surface. Conductive paste ensures good interfaces between the copper material and the thermocouple hot junctions.

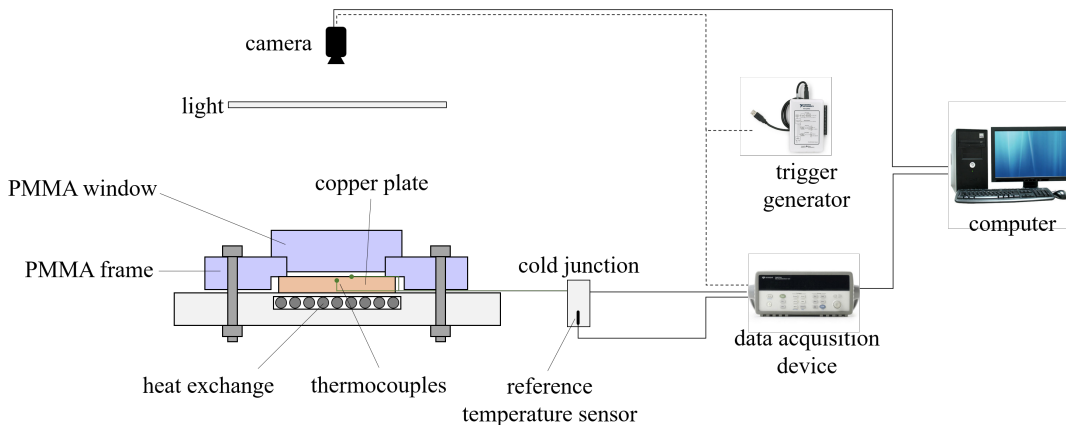


Figure 3.24: Calibration facility sketch, for temperature evolution approach

The vision system is equivalent to that of the facility for the calibration via the temperature gradient approach. Different thing is the trigger generator that synchronizes the acquisition of the images and temperatures. Thus allows to correctly associate the information about temperature and colour, and to obtain an accurate liquid crystals calibration.

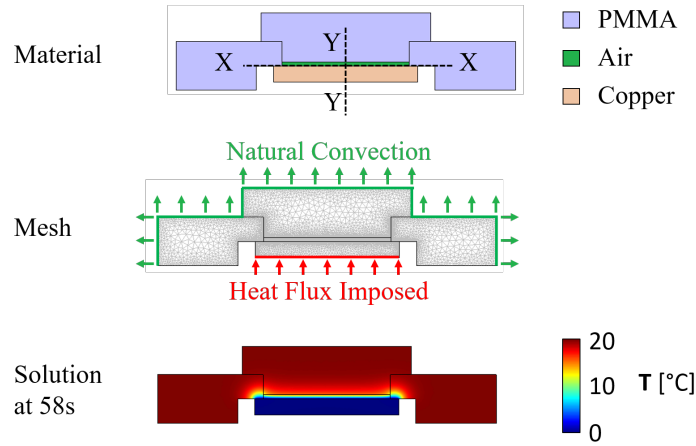


Figure 3.25: Two-dimensional model for Comsol simulation

The calibration facility is designed in order to have an almost uniform temperature distribution in the calibration plate. For this reason, the calibration plate is made of a very conductive metal with high thermal diffusivity, such as copper. To verify the quasi-isothermal plate behaviour, several two-dimensional simulations were performed in a transient regime using Comsol MultiphysicsTM. The Comsol model is composed of three subdomains obtained from the cross-section of the facility, as shown in Fig. 3.25. The simulation has been carried out for 60 s with a time-step of 0.1 s, under the following boundary conditions:

- natural convection on all the outer walls;
- outgoing heat flux in the lower face of the copper plate.

The values of the parameters used for the simulation are summarized in Tab. 3.4.

Table 3.4: Boundary condition parameters of Comsol transient simulation

| | | |
|---------------------------|-----------|--------------------------------------|
| heat transfer coefficient | h | $4 \text{ W}/(\text{m}^2 \text{ K})$ |
| ambient temperature | T_{amb} | 20°C |
| initial temperature | T_0 | 20°C |
| heat flux | q | $5000 \text{ W}/\text{m}^2$ |
| heat transfer area | A | $35 \times 35 \text{ mm}^2$ |

From the resulting solution at time 58 s (Fig. 3.26) the copper plate seems almost at the same temperature. In order to quantitative argue, the maximum temperature difference across two planes is evaluated at each time steps.

The planes are identified in Fig. 3.25:

- X-X plane is coincident with the top surface of the plate;
- Y-Y plane is orthogonal to X-X plane and passes through the symmetry line of the plate.

During the simulated calibration test, the maximum temperature difference ΔT_{max} never exceeds 0.03°C as can be seen in the Fig. 3.26. Moreover, the cooling rate considered during the simulation (about $0.35^\circ\text{C}/\text{s}$) is much greater than the one of the calibration tests (about $0.01^\circ\text{C}/\text{s}$ as will be seen later on). These considerations lead to consider a uniform temperature inside the plate.

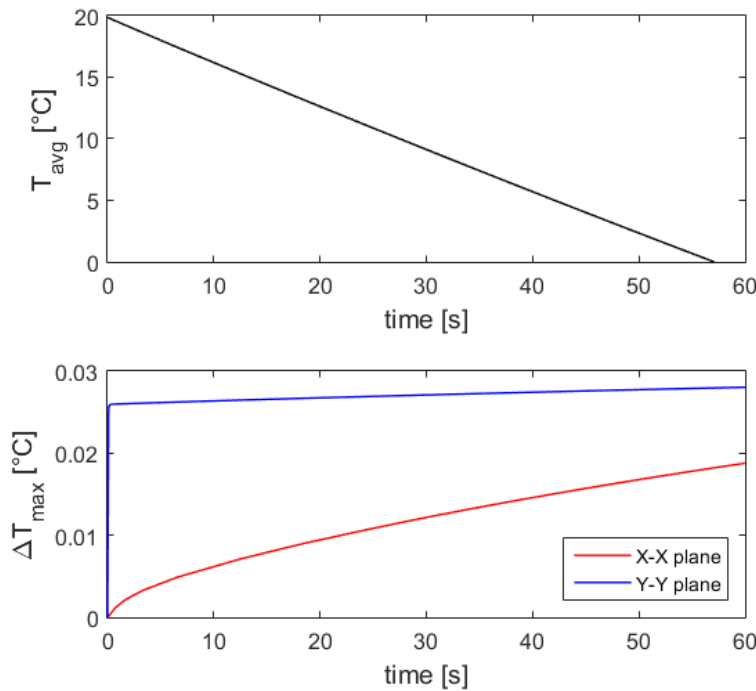


Figure 3.26: Transient copper plate simulation results: average temperature evolution (top) and maximum temperature differences onto X-X and Y-Y planes (bottom)

3.4 Liquid crystals surface preparation technique

The surface where the liquid crystals will be applied has to be clean. Therefore all surfaces are firstly washed with a degreaser, next with distilled water, and left to dry later. Besides, the calibration plates made of metal are primarily polished by using fine grain sandpaper. Finally, the black paint (SPB100, Hallcrest) and the liquid crystals can be applied waiting for about 12 hours between them, this to be certain of the correct drying of the black background before depositing the LC mixture.

The liquid crystal mixture preparation and application method chosen is close to that proposed by D.J. Farina et al. [13]. The method is made up of four steps:

1. *Coarse mixing.* The relative large clumps of material that could be found in a bottle of microencapsulated LC are broken up into small scale. The compound is mixed by hand until a uniform consistency is obtained.
2. *Dilution.* The compound is diluted with distilled water at a rate of 10:1, this reduces its overall viscosity.
3. *Filtering.* A proper filtration system is used to break up any remaining clump resulting after the two previous phases. This step allows having a more uniform liquid crystal compound in order to minimize the clogging of the airbrush and to produce smoother surfaces.
4. *Spraying.* The mixture is sprayed with an airbrush (Airbrush-BD 105) equipped with a mixing nozzle 0.3 mm of diameter and supplied with 2 bar compressed air. The airbrush smoothly follows a regular path and it is continuously kept about $30 \div 40\text{ cm}$ away from the surface. The liquid crystals mixture is sprayed in several thin coats. Spraying and drying are repeated until the desired colour intensity is reached.

The calibration surfaces are prepared at the same time as the test surfaces of the channel model to ensure consistent performance. However, the surfaces can be used at least one day after their treatment. They are stored always in the same dark dry place at room temperature when not in use. This reduces any possible different degradation between calibration plates and model walls and protects the painted surfaces against contamination or exposure to UV radiation.

Chapter 4

Data reduction

4.1 Camera calibration

A method to calibrate cameras is almost essential whenever in the measurements a vision system is implemented. The twofold aim of the camera calibration is:

- *Color calibration.* Setting the image acquisition parameters in order to have the same colours perception of the cameras that are employed in the different facilities (i.e., calibration facilities and test facility);
- *Spatial calibration.* Definition of the function that links image to real space (i.e., where is actually located in space a pixel of the image).

The camera calibration procedure has been done systematically for all the vision system configurations employed in the present work.

4.1.1 Color calibration

In this thesis work, the liquid crystal thermography is implemented in two different methods. In both cases, the wall temperature is taken from the colour indication provided by the liquid crystals, which have to be previously calibrated in order to obtain a relationship between temperature and appeared colour. The consistency of the temperature information pretty depends on the configuration of the vision systems that are used during the test and calibration phases. As stated, the vision systems have to be as similar as possible to avoid unwanted influences from lighting conditions or the viewing angle.

In the transient method, the colour vision setting doesn't significantly affect the accuracy of the measurements since the thermography provides the temperature information searching the maximum of the green colour. Whereas in the steady-state approach, the temperature indications suffer greatly from different arrangements of the vision systems. Indeed, the colour description is based on the hue parameters, which depends very much from the viewing angle and the colour temperature of the light source. Consequently, accurate colour calibration of all the cameras is required.

The colour calibration phase consists of:

1. Positioning of the same coloured target on all the surface to calibrate;
2. Acquisition of the images;
3. Evaluations of the colour in the images;
4. Setting new camera parameters;
5. Verification of the correct colour vision.

The coloured target is composed of three equal stained stripes that provide the three primary colour and is taped on the surfaces. The three images acquired by the cameras used for the steady-state thermography are reported in Fig. 4.1.

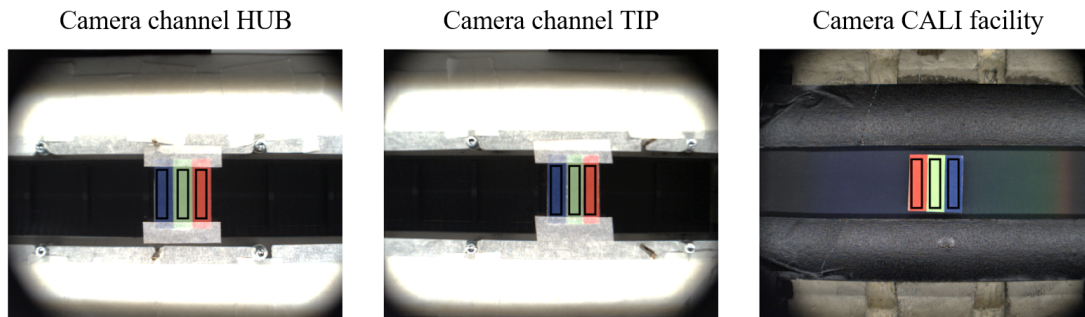


Figure 4.1: Images acquired by the cameras used in the steady-state thermography

For each image, the hue is averaged within the interrogation windows, which are identified by the black line boxes in Fig. 4.1. The averaged values are then compared in histograms, such as reported in Fig. 4.2. The colour calibration is successfully achieved if all the bars have the same height. Otherwise, the colour gains of the cameras have to be adjusted.

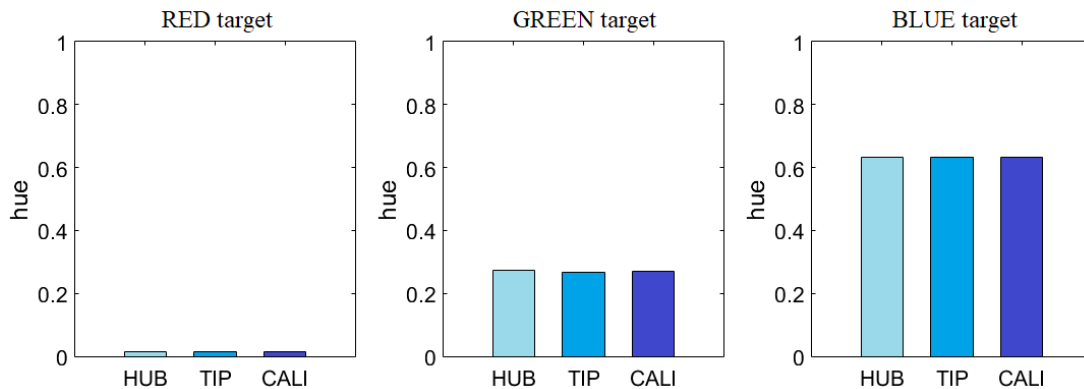


Figure 4.2: Colour evaluation of the camera images

4.1.2 Spatial calibration

The perspective, the refraction, and the distortions, associated with a camera and its optics, make tricky to determine the space transformation (e.g., the lens cause radial, tangent, and linear distortion). Several calibration procedures are available in the literature: from simple empiric correlations to methods in which the calibration is accomplished through the identification of corresponding points between the video acquired during the movement of the camera and the frame of a static scene. Since the relative position between cameras and investigated plane is fixed in the liquid crystals thermography, the adopted calibration procedure includes the following steps:

1. Positioning of a target pattern on the surface to calibrate;
2. Acquisition of the camera images;
3. Pattern recognition and definition of the space transform functions.

The pattern target is a sheet of paper printed with a grid of equally spaced black dots. Once the patter grid is positioned onto the surface of interest and is properly illuminated, the cameras take the digital images. After that, an in-house Matlab routine analyzes the acquired frames to extrapolate the relationships between the image reference systems and physical reference systems.

For clarification purposes, the spatial calibration of one camera of the test facility is taken as an example in order to explain the procedure. Three reference systems are defined to perform the calibration and they are illustrated in Fig. 4.3:

- Channel reference system (y, z) ;
- Local physical reference systems (a, b) , it has the axis direction parallel to those of the channel reference system and it is defined during the spatial calibration;
- Image reference system (i, j) .

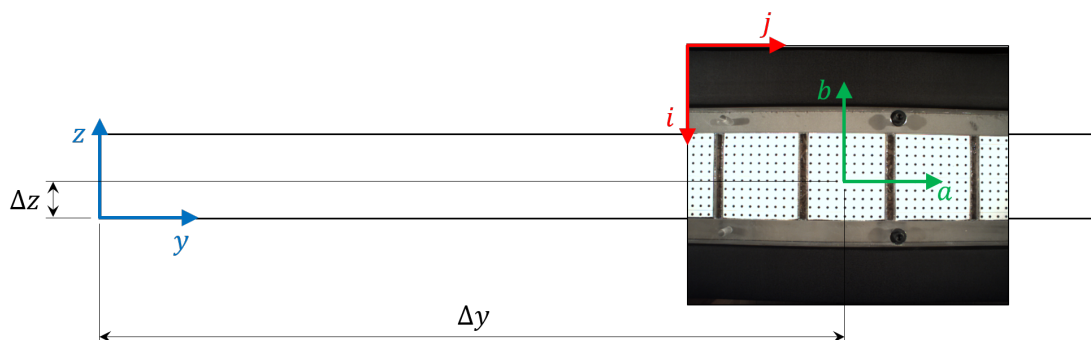


Figure 4.3: Reference systems during the spatial calibration

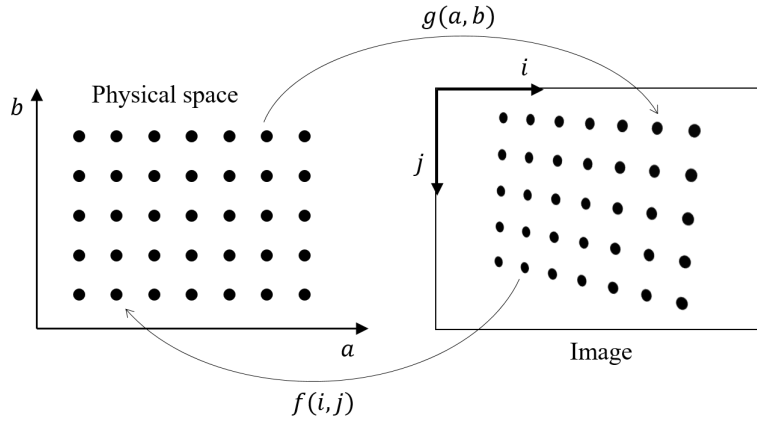


Figure 4.4: Space transformations

The dots are recognized by means of cross-correlation with a reference dot and their positions are consequently obtained in the image reference system. The software computes the space transformation from the image reference system to the channel reference system in two steps:

- From (i, j) to (a, b) , defining the mapping function that take into account of the optical aberrations and of the magnification factor;
- From (a, b) to (y, z) , using a isometric translation.

The software firstly associates at each dots the corresponding physical coordinates, which are relative to the user-defined local physical reference system; then evaluates the mathematical mapping function that allows the passage from image space (i, j) to local physical space (a, b) :

$$f : (i, j) \longrightarrow (a, b) \quad (4.1)$$

The mapping function f is a polynomials equation up to degree four, which is written as:

$$f : \left\{ \begin{array}{l} a = k_{a0} \\ \quad + k_{a1}i + k_{a2}j \\ \quad + k_{a3}i^2 + k_{a4}ij + k_{a5}j^2 \\ \quad + k_{a6}i^3 + k_{a7}i^2j + k_{a8}ij^2 + k_{a9}j^3 \\ \quad + k_{a10}i^4 + k_{a11}i^3j + k_{a12}i^2j^2 + k_{a13}ij^3 + k_{a14}j^4 \\ b = k_{b0} \\ \quad + k_{b1}i + k_{b2}j \\ \quad + k_{b3}i^2 + k_{b4}ij + k_{b5}j^2 \\ \quad + k_{b6}i^3 + k_{b7}i^2j + k_{b8}ij^2 + k_{b9}j^3 \\ \quad + k_{b10}i^4 + k_{b11}i^3j + k_{b12}i^2j^2 + k_{b13}ij^3 + k_{b14}j^4 \end{array} \right. \quad (4.2)$$

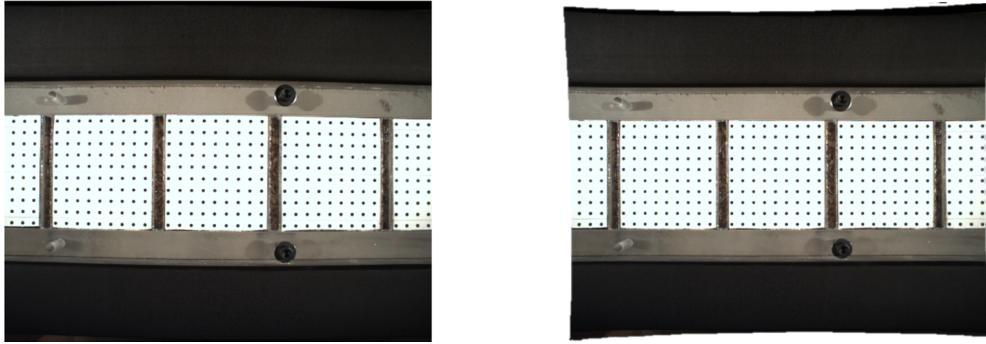


Figure 4.5: Acquired (left side) and dewarped image(right side) of the transient model channel

The polynomial coefficients k in 4.2 are evaluated using the least-squares method and are valid only for the vision configuration employed at the moment of the calibration phase. Any change in the setup that violates the mapping information compromises the accuracy of the calibration.

Finally, the knowledge of the relative position between the local reference system (a, b) and the channel reference system (y, z) , i.e. the distance Δy and Δz , lets to complete the space calibration:

$$\begin{cases} y = \Delta y + a(-1)^{Y_{rev}} \\ z = \Delta z + b(-1)^{Z_{rev}} \end{cases} \quad (4.3)$$

where Y_{rev} and Z_{rev} can be 0 or 1 depending if the axes of the channel and local reference systems are parallel or antiparallel.

Figure 4.5 shows the comparison between the acquired image and the relative post-processed image in which it is implemented the mapping function. From the reconstructed image, it is possible to appreciate the good de-warping capacity of the polynomial function.

4.2 Transient experiments data processing

In the tests with the transient approach, the heat transfer coefficient distribution is computed knowing for each location:

- The evolution of the fluid temperature;
- The time instant at which the liquid crystals have reached the max green colour intensity (that is the only moment in which the wall temperature is known).

However, these information are not readily available from the experimental data, therefore a proper elaboration is required.

4.2.1 Fluid temperature evaluation

The inlet air temperature is not constant during the test, and furthermore, the fluid flowing into the channel continuously acquires energy from the warmer walls. Therefore, the bulk temperature depends on both space and time.

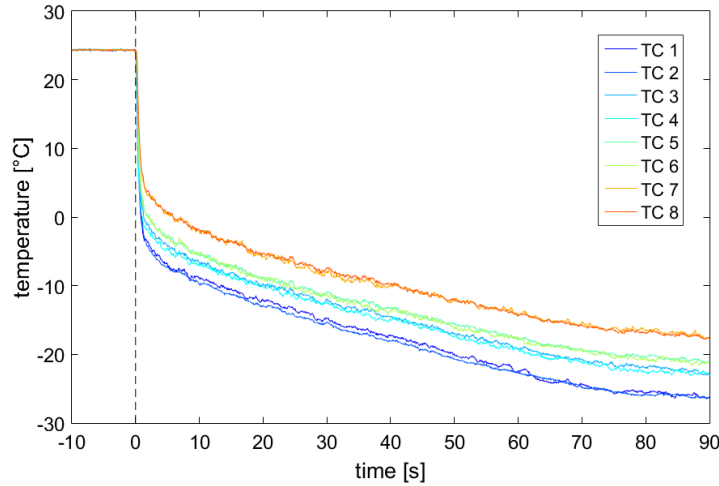


Figure 4.6: Thermocouples signals acquired during a transient test

At different discrete position, the temperature time-evolution is obtained from the application of a low-pass filter to the signals of the thermocouples immersed on the core flow, which are shown in Fig. 4.6. Then at each time step, a spatial interpolation scheme is implemented. As done by R. Poser et al. [43], the fluid temperature distribution is described by the Laplace equation:

$$\nabla^2 T_f = 0 \quad (4.4)$$

More precisely, this differential equation describes the steady-state conduction in a solid; however, it is nevertheless used as diffusion model here for interpolation purpose only. The temperature values at the thermocouple positions are the inner boundary conditions of Eq. 4.4; while a zero heat flux is imposed at the walls, inlet and outlet of the channel ($\partial T_f / \partial \mathbf{n} = 0$, with \mathbf{n} normal surface vector). Equation 4.4 is numerically solved using a finite element method. As shown in Fig. 4.7, the computational grid is formed by 3-node triangular cells that are very common in unstructured grids. Anyway, this type of grid is not the most suitable for this geometry but allows to create grids on even very complex domains for potential further applications.

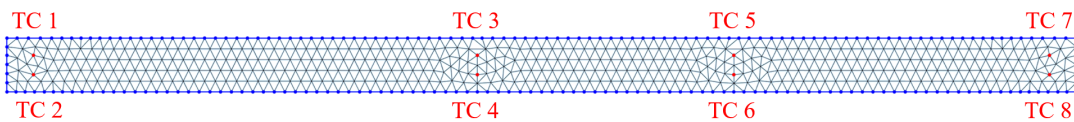


Figure 4.7: Computational grid for fluid temperature interpolation

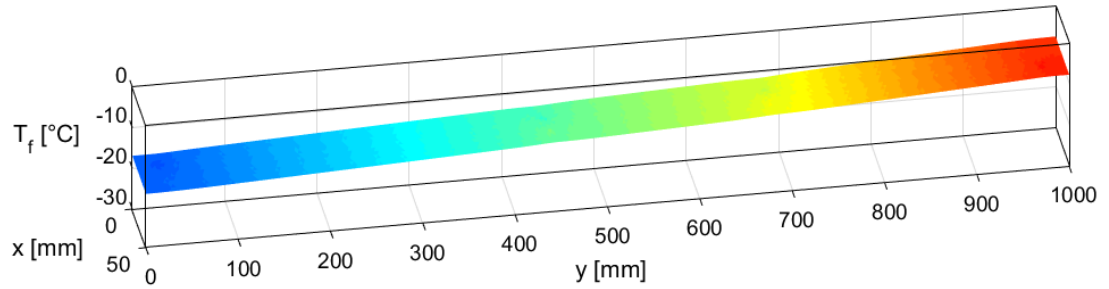


Figure 4.8: Interpolated spatial distribution of the fluid temperature at one time instant

4.2.2 Surface temperature evaluation

The indications of the surface temperatures are available only within the time interval in which the liquid crystals are active (i.e., when they are in the colour play range). The moment at which the liquid crystals reaches the maximum intensity of green is called ‘activation time’ and at this time is assigned the surface temperature obtained from the calibration phase. An in-house Matlab routine performs the analysis of the image sequence acquired by the cameras in order to detect the activation times. The procedure consists of five steps:

1. Image sequence loading;
2. Background subtraction;
3. Signal filtering;
4. Peak finding;
5. Activation time validation and liquid crystals association;

1. Image sequence loading

The images are stored in TIFF raster format with 1.3 megapixel resolution (1280×1024 pixels) and are described by the RGB colour model. The colour depth is 24-bit, hence 8-bits for each colour channel that determines $2^8 = 256$ intensity levels. The image loading is limited to a region of interest (ROI) that excludes the areas where the activation times are not meant to be found (in Fig. 4.9 is given an example of ROI definition). This approach is obviously beneficial in terms of computer memory taken.

The Matlab routine reads the colour information contained in the ROI and consequently occupies a memory space M_{ROI} in the volatile memory of the computer (RAM) that can be evaluated in bits as:

$$M_{ROI} = N(W_{ROI} \times H_{ROI})d_{bit} \quad (4.5)$$

where W_{ROI} and H_{ROI} are the width and height of the ROI, d_{bit} is the bit colour depth of the image, and N is the number of frames of the acquired sequence.

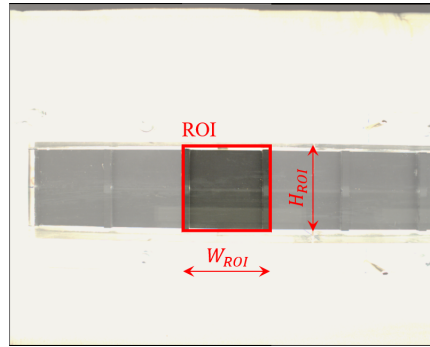


Figure 4.9: Example of ROI of the 9th inter-rib

All the data contained in the ROI can exceed the RAM available on the computer M_{RAM} , therefore the ROI is loaded in several information packs, called ‘sub-domains’. The number of sub-domains n_{sd} is valued as the next integer number resulting from:

$$n_{sd} = \frac{M_{RAM}}{M_{ROI}} \quad (4.6)$$

Each sub-domain is loaded, analysed and uncached one by one. At the end of this step, the time-evolutions of the three primary colour are made available for each pixel belonging to the ROI.

Figure 4.10 reports several relevant frames extracted from a transient thermography video (the frames correspond to the ROI defined in Fig. 4.9). The colour transitions performed by the two types of liquid crystals are possible to appreciate: on the lower half of the channel, the liquid crystals with the greater starting temperature reveals the colour play first. Furthermore, Fig. 4.10 reports the colour history extracted for a pixel. A peak is clearly recognizable for each colour channel evolution even if the signal is quite noisy.

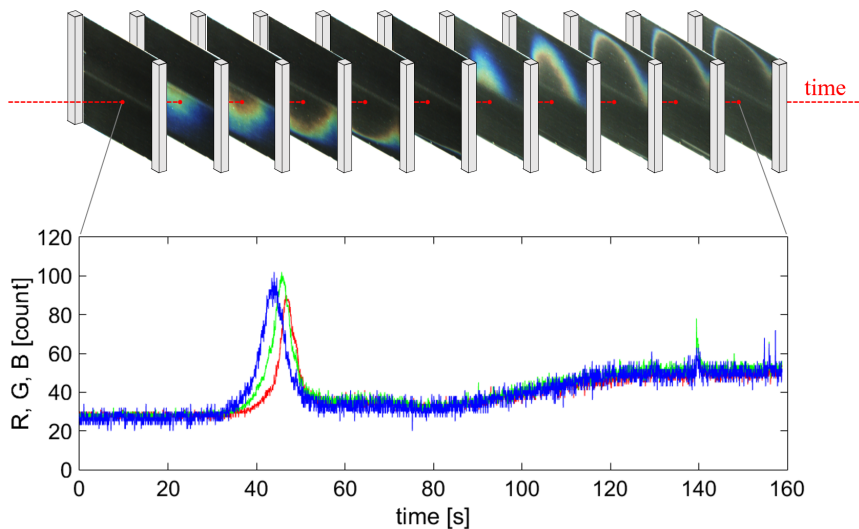


Figure 4.10: Image sequence reduction of acquisition for a transient thermography test and example of the colour history of a pixel

2. Background subtraction

The background image is created by averaging the colour information over the first 25 frames acquired (first second of acquisition), in which the liquid crystals certainly are not in the visible colour range. The background is then subtracted from the other images so that the colour channel signals come to about zero when the liquid crystals are not visible. This will simplify the definition of the thresholds that will be used in the peak finding step. Figure 4.11 gives an example of the background subtraction of the colour signals of Fig. 4.10.

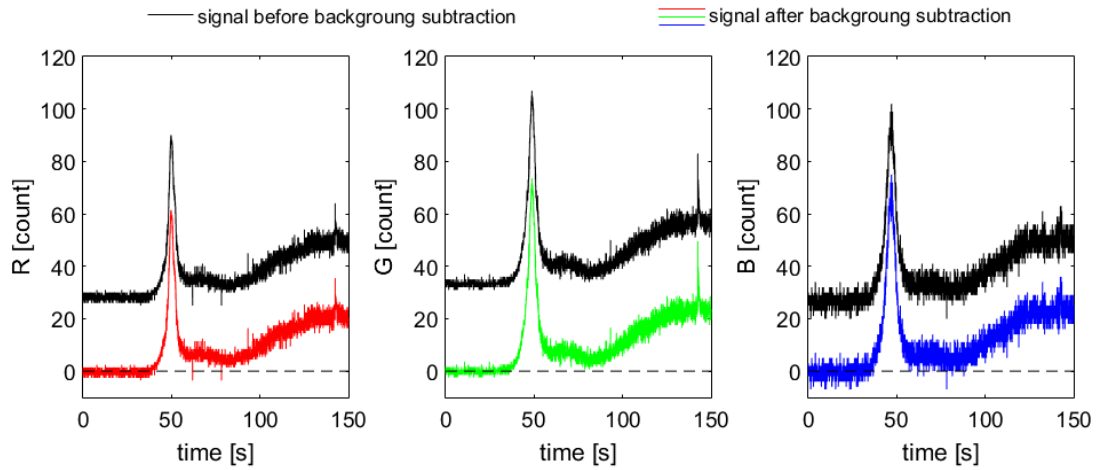


Figure 4.11: Background subtraction

3. Signal filtering

The colour signals are filtered to attenuate the unavoidable noise that is mainly due to the CCD sensors of the camera and liquid crystals local instabilities. A no suitable filter or even the no attendance of filtering would compromise the precision of the peak finding step, hence the accuracy of the heat transfer evaluation.

The implemented filter is based on the frequency-domain analysis of the signal. The generic signal defined in the time-domain $s(t)$ is decomposed into exponential functions through the application of the Fourier transform:

$$S(f) = \mathcal{F}[s(t)] \quad (4.7)$$

Since the signal is sampled, the discrete Fourier transform is applied. Fig. 4.12 shows the frequency spectrum of the green channel signal of Fig. 4.11. As the image sampling frequency is 25 Hz , the spectrum is helpful up to 12.5 Hz (Nyquist frequency). The spectrum is characterized by a high information content at low frequency, whereas at the other frequencies the magnitude is close to zero. The latter frequency range is accountable for the noise content, so a low-pass filter is suitable for the noise reduction.

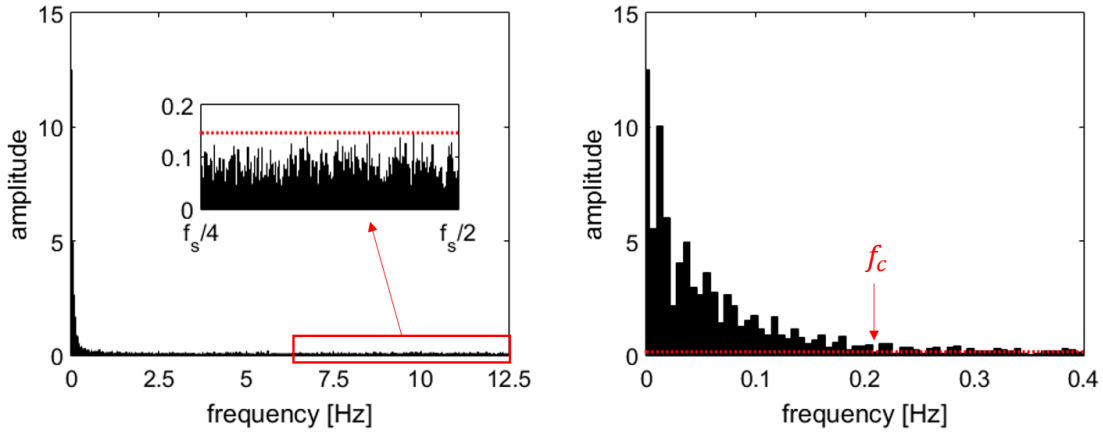


Figure 4.12: Frequency spectrum

The filter forces the magnitude values above a determinate cutoff frequency to zero and then the inverse discrete Fourier transform is implemented to build the filtered signal. The cutoff frequency is defined as the lower frequency with the magnitude less than a certain noise threshold, which is define as the maximum value of the magnitude in the frequency range within $f_s/4$ and $f_s/2$, where f_s is the sampling frequency. In summary, the signal filter $s_f(t)$ is obtain by:

$$s_f(t) = \mathcal{F}^{-1}[S(f)] \quad \text{with} \quad S(f_c \leq f \leq f_s) = 0 \quad (4.8)$$

In Eq. 4.8, the time-continuous notation is used for the sake of clarity, however the discrete approach is required to perform the filtering phase.

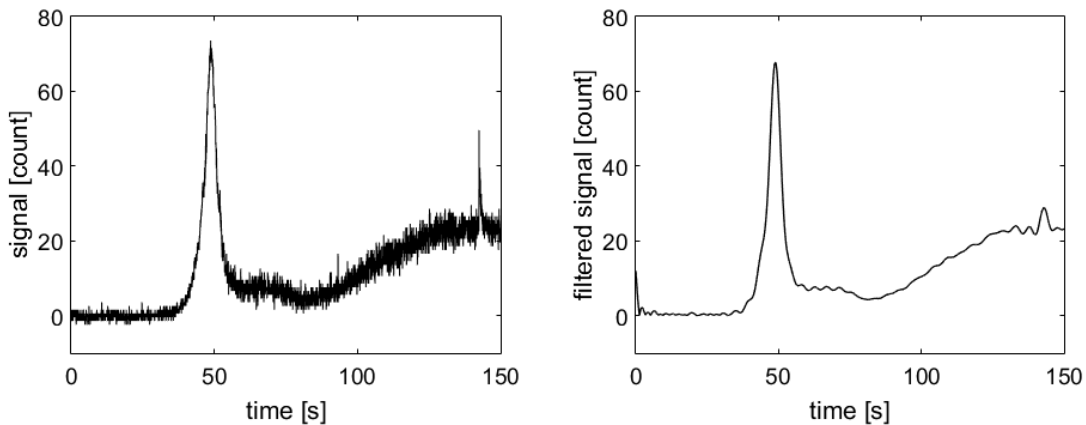


Figure 4.13: Raw starting signal (left side) and relative filtered signal (right side)

Fig. 4.13 shows the comparison between the original signal (on the left) and the resulted signal (on the right) after the implementation of the filter based on the Fourier analysis. The filtered algorithm as is implemented is characterised by reliability and robustness, without having to set any threshold since the cutoff frequency is auto-tuned.

4. Peak finding

The activation time corresponds to the time at which the green signals reach the local maximum, or in other words, the instant when the top of a peak is reached. The peak searching is carried out for each colour channel anyway, therefore at the end of this phase, the three positions of the colour signal peaks will be available. The searching routine starts with the evaluation of the first derivative of the filtered signals s_f using the central finite scheme as:

$$\dot{s}_{f,i} = \frac{s_{f,i+1} - s_{f,i-1}}{2\Delta t} = (s_{f,i+1} - s_{f,i-1}) \frac{f_s}{2} \quad (4.9)$$

Fig. 4.14 shows the filtered signal s_f and the normalized derivative of the filtered signal \dot{s}/\dot{s}_{max} . The figure also highlights several points, which are identified by the searching algorithm.

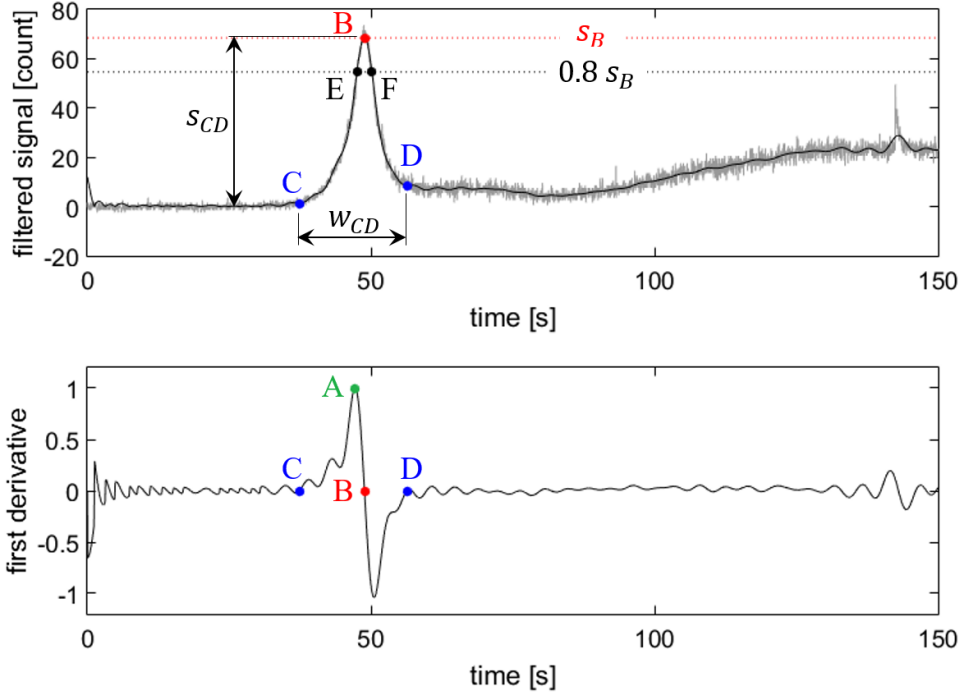


Figure 4.14: Derived points in the peak finding procedure

The algorithm identifies the maximum of the first derivative (point A) and then scan rightward in order to get the point in which the first derivative is zero (point B). Two more points are identified with zero derivative value (points C and D), before and after point B. These points detect the foot of the peak and are adopted to evaluate the time width of the peak w_{CD} . The least width threshold w_{min} is set to reject the liquid crystals colour transition that hasn't a reasonable time length concerning the considered transient test:

$$w_{CD} \geq w_{min} \quad (4.10)$$

Then the algorithm verifies if the value of the raw signal in B is greater than a height threshold s_{min} defined by the user:

$$s_B \geq s_{min} \quad (4.11)$$

The height threshold is used in order to avoid fake peak and no longer consider peak with low signal-to-noise ratio. If both conditions of Eq. 4.10 and 4.11 are true, the procedure determines others two points (points E and F) that are obtained from the intersection of the raw signal with a horizontal line at ordinate equal to the 80% of point B height. The stencil of points within the range E-F is used to refine the maximum location: the raw signal is interpolated by a quadratic function and at its maximum is assigned the position of the peak top as illustrated in Fig. 4.15

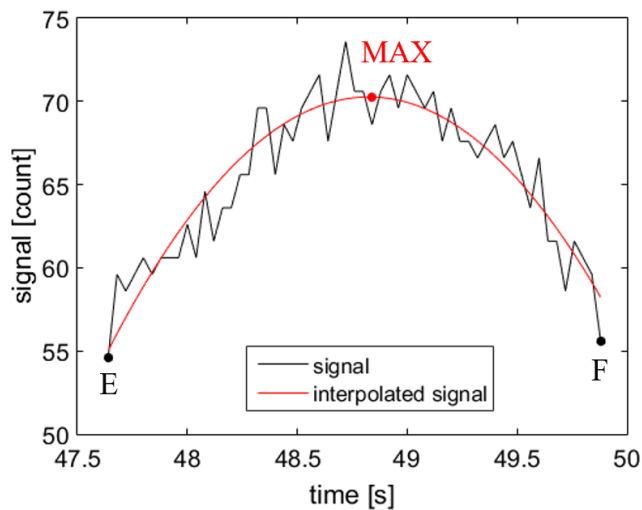


Figure 4.15: Peak finding refinement

5. Activation time validation and liquid crystals association

The previous step finds out all the peaks for each colour channel of the pixels that belong to the ROI. The activation time of a pixel is defined once both the following requirements are fulfilled:

1. *Existence*: one peak is found for each colour channel;
2. *Proper order*: the three peaks pertaining to the primary colours are in the expected timeline.

If a pixel hasn't a peak for each colour channel that respects the peak finding thresholds, then the first condition is not satisfied and no activation time will be assigned to that pixel. Besides, the colour history of a single channel can have more peaks. In this case, the algorithm selects the most probable peak that has better characteristics in terms of signal-noise ratio, time-width and closeness to the peaks of the other colour channels. After this selection, a flag is assigned at this pixel to report the presence of multiple peaks.

The activation time is assigned as long as the second condition is satisfied as well. In the transient thermography, the channel walls are cooled hence their temperature will go down. The optical behaviour of the liquid crystals ensures that the colour transition will go from the blue to the red, passing through the green colour. Therefore, the software routine verifies if the time sequence of the peaks are blue, then green and finally red. If the proper order requirement is not fulfilled, then no activation time will be given at the pixel.

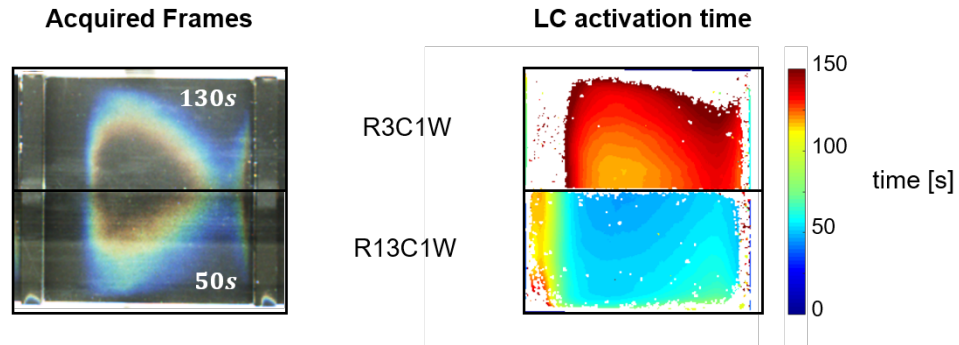


Figure 4.16: Halves of two frames acquired during transient test of the 9th inter-rib at different time (left side) and relative liquid crystals activation time map (right side)

The investigated surface includes two areas that are sprayed with different types of liquid crystals paints. In order to assign the proper wall temperature, a simple and straightforward solution is adopted: two ROI are manually defined for the two different liquid crystals region. Then, at each ROI is assigned the corresponding liquid crystals calibration temperature value.

4.2.3 Heat transfer evaluation

In the previous paragraphs, it has been described how the information needed to compute the heat transfer coefficient can be obtained. However, this information has not a spatial coherence between them because they are related to two different domains. Indeed, the images sequence analysis provides the activation time for each pixel; meanwhile, the flow temperature evolution is available in the physical space. For each pixel that belongs to the ROI, the activation time associated with the pixel location is hence transferred in the respective physical location by means of the relationship function that has been obtained from the spatial calibration of the cameras. Then the fluid temperature evolution of the nearest node of the computational grid is assigned. Finally, the calculation of the heat transfer coefficient is carried out by means of an iterative method that solves the transient heat conduction equation (as described in Par. 2.4):

$$T_w = T_0 + \sum_{i=1}^N \left[1 - \exp\left(\frac{h^2(t - \tau_i)}{(\rho k c)_{mat}}\right) \operatorname{erfc}\left(h\sqrt{\frac{t - \tau_i}{(\rho k c)_{mat}}}\right) \right] (T_{f,i} - T_{f,i-1}) \quad (4.12)$$

4.3 Steady-state experiments data processing

All the experimental data are collected when the temperature within the system does not change with time. A dedicated Matlab routine processes the information in order to calculate the spatial distributions of the fluid and wall temperatures. Particular attention has been dedicated to the estimation of the heat losses to properly evaluate the heat transfer coefficient.

4.3.1 Fluid temperature evaluation

Under steady-state conditions the temperature within the system does not change with time, therefore the fluid temperature has only a spatial distribution. The airflow enters at channel inlet with a measured temperature of T_{IN} , then it is warmed by the heater elements located on the inner channel surfaces, and it finally leaves the channel with an outlet temperature of T_{OUT} . It is assumed that the flow mean temperature is linearly increasing along the channel length:

$$T_f(y) = T_{IN} + \frac{T_{OUT} - T_{IN}}{1000}y \quad (4.13)$$

The one-dimensional interpolation is a reasonable assumption on the base of theoretical consideration (the uniform Joule heating and the periodical flow condition) and experimental evidence (in the transient test, the spatial evolution of the fluid temperature is indeed almost an inclined plane, as Fig. 4.8 proves).

4.3.2 Surface temperature evaluation

Four images of the different section of the investigated surface are available from the cameras, which are reported in Fig. 4.17. The four cameras frame the entire ribbed surface and so the wall temperature can be computed on the whole surface. A dedicated Matlab routine extracts the hue information from each image and associate to them the surface temperatures, thanks to the calibration curve g (it will be obtained in Par. 4.4):

$$T_w = g(hue) \quad (4.14)$$

After that, the wall temperature distribution is transferred to the channel reference system, according to the space transformation function that has been obtained in the spatial calibration phase.

Figure 4.17 shows the resulting wall temperature map for the steady-state thermography that is carried out in static condition and with only the ribbed wall heated. It is possible to notice that temperatures information are achieved almost over the entire surface. The blank regions are due to the miss of the colour data (no liquid crystals colour transition occurred), or whether the hue values are outside the confidence range provided by the calibration curve.

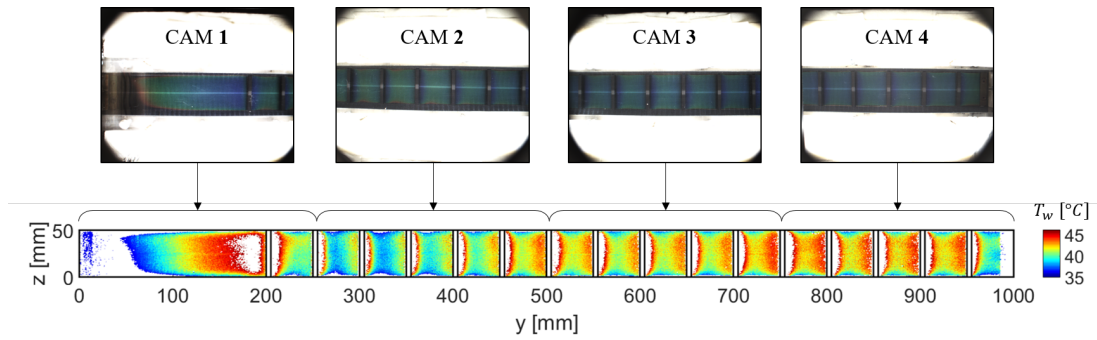


Figure 4.17: Wall temperature distribution evaluated from the acquired images

4.3.3 Heat transfer evaluation

As stated in Par. 2.3, the local heat transfer coefficient can be evaluated by using the following relation:

$$h = \frac{q_{joule} - q_{loss}}{T_w - T_f} \quad (4.15)$$

At this point, the wall and fluid temperature distributions are available from the previous elaborations, and the Joule heat flux can be calculated from the measured power supplied P_{joule} (see 3.7). Since the heating elements are rectangular continuous Inconel foils with a constant thickness and a constant current supplied, they develop an overall uniform electric field and generate each one a heat flux evaluated as:

$$q_{joule} = \frac{P_{joule}}{n_s A} \quad (4.16)$$

where A is the surface area of one foil and n_s is the number of the channel side heated. What remains is to assess the heat dissipated q_{loss} , which, as well known, is the key factor in the accuracy of the heat transfer evaluation. The estimation procedure has hence to take into account the following contributions to achieve faithful heat transfer distributions:

- the radiative heat transfer that is established between the investigated surface and the surrounding ones;
- the transversal conduction in the Inconel layers, which have a high thermal conductivity although their small thicknesses;
- the conduction through the PMMA walls and insulating cover (e.g., the lateral channel walls behave like heat sinks for the ribbed surface);

Moreover, the procedure has to deal with different inner boundary conditions: the configuration with three heated foils leads to a different thermal behaviour compared to the case in which the heat is generated only at the ribbed surface. These requirements and considerations have led to the set up of a numerical analysis. Since the overall heat loss consists of conductive and radiative losses,

two FEM models have been built in ANSYS CFX to consider each contribution. The models are then inserted in an iterative procedure in order to accomplish the heat transfer distribution on the ribbed surface.

Conduction FEM model

The model is a simplification of a section between the 6th ($y = 455 \text{ mm}$) and the 13th rib ($y = 800 \text{ mm}$) of the real test channel, as illustrated in Fig. 4.18. Only a part of the entire channel was considered in order to simplify the process of setting up the wholly iterative procedure and to reduce the computational cost. Three subdomain are present and have the thermo-physical properties of Inconel, PMMA and foam. A cross-section view of the structured mesh used for the computation is shown in 4.19. The Inconel sheet is modelled with a single layer of elements with a surface dimension of $0.5 \times 0.5 \text{ mm}$ and a thickness equal to the Inconel one. This configuration, made of 1'786'420 elements, is the results of a mesh sensitivity analysis that was carried out by reducing progressively the dimension of those elements. The boundary condition are set as follows:

- The Inconel domain generate the Joule power (if the foils are switched off, the internal source of heat is set to zero).
- The cross surfaces are considered as adiabatic because of the periodical behaviour of the inter-rib (this introduce a little approximation);
- A constant temperature is assigned at the outer surfaces. The value is the average of the thermocouples that are located on the outer surface of the insulating cover;
- At the inner surfaces, radiative and convective heat transfer distributions are imposed;

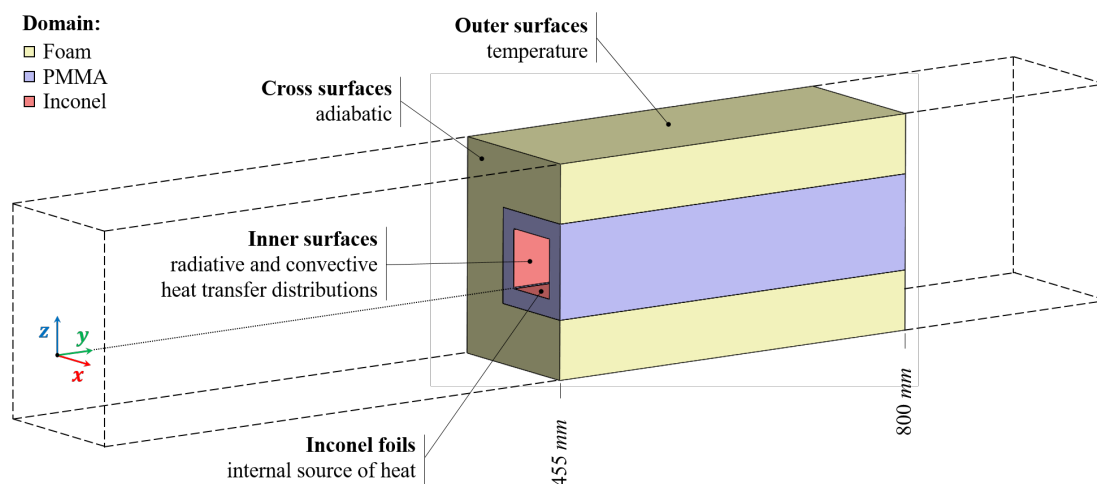


Figure 4.18: Boundary condition for the conduction problem

The latter boundary condition requires further discussion. The radiative heat fluxes set to the inner surface come from the results of the radiative FEM model. The radiative heat distribution is superimposed on the convective heat transfer, which is set by means of heat transfer coefficient and fluid temperature distributions. At the smoothed surfaces, the heat transfer coefficient value is given by the surface averaged enhancement factor for smooth sidewall (equals to 1.6), resulted from the study done by Çakan [6]. Meanwhile, an attempting heat transfer coefficient distribution is applied at the ribbed surfaces (which will be presented on the iterative procedure).

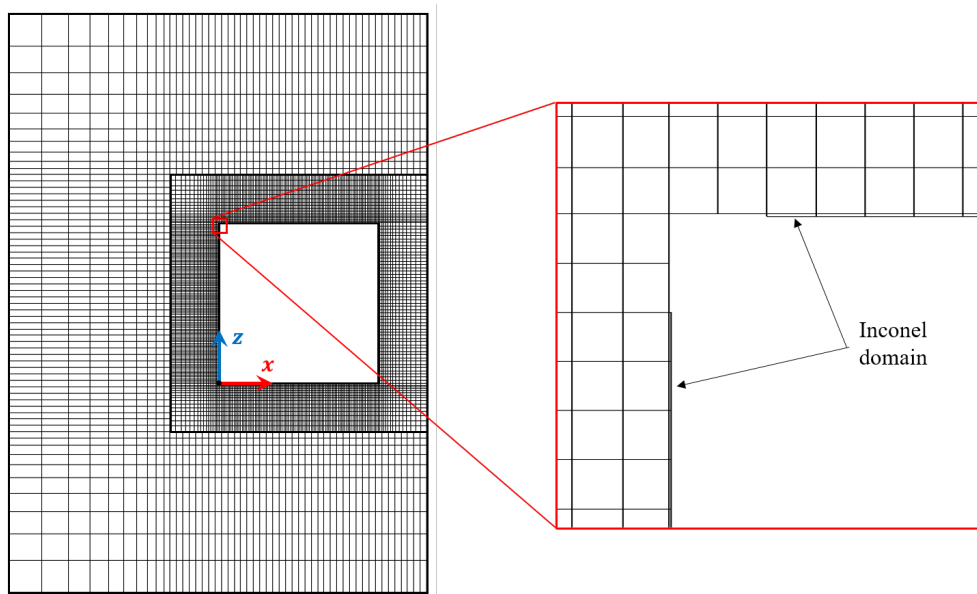


Figure 4.19: Computational mesh used for the conduction problem

Radiative FEM model

Since the PMMA material is opaque to IR, the relevant radiative heat fluxes may occur only between inner channel surfaces. For this reason, the numerical model used to evaluate the radiative heat fluxes is composed of the air volume that is enclosed inside the channel walls, as shown in Fig. 4.20. The air is considered only as a radiative medium, and not with the aim to simulate the flow field inside the channel. Therefore, no buoyancy and turbulence models are applied to the still air, but only the discrete radiative transfer mode surface to surface is set in the ANSYS configuration. In a preliminary phase, all the possible radiative models provided by ANSYS has been tested in a simple benchmark case and the most suitable ones for the present case has been chosen. The computational grid is formed by uniform quadrilateral 0.5 mm size mesh and the boundary conditions are set as follows:

- The cross surfaces are considered as symmetry walls;
- On the walls, temperatures and emissivity coefficients are imposed;

The wall temperatures are extracted from the solution of the conductive FEM model, and the emissivity coefficients are chosen to be equal to 1 for the black wall and 0.96 for the ribbed surface. The latter value is got from Lucas et al. [32], who measured it for encapsulated liquid crystals layer over black ink.

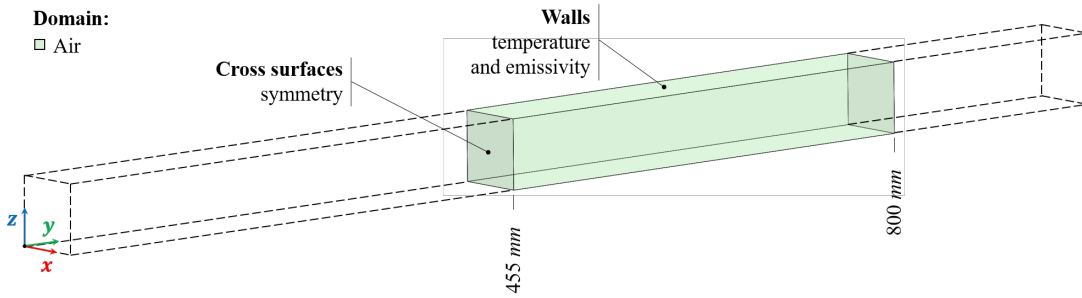


Figure 4.20: Boundary condition for the radiative problem

Iterative procedure

A macro routine written in Matlab deals with calculations, interpolations, execution of FEM simulations, and files management of the iterative procedure that is set up to evaluate the heat transfer performances. Figure 4.21 presents the block diagram of the entire iterative loop.

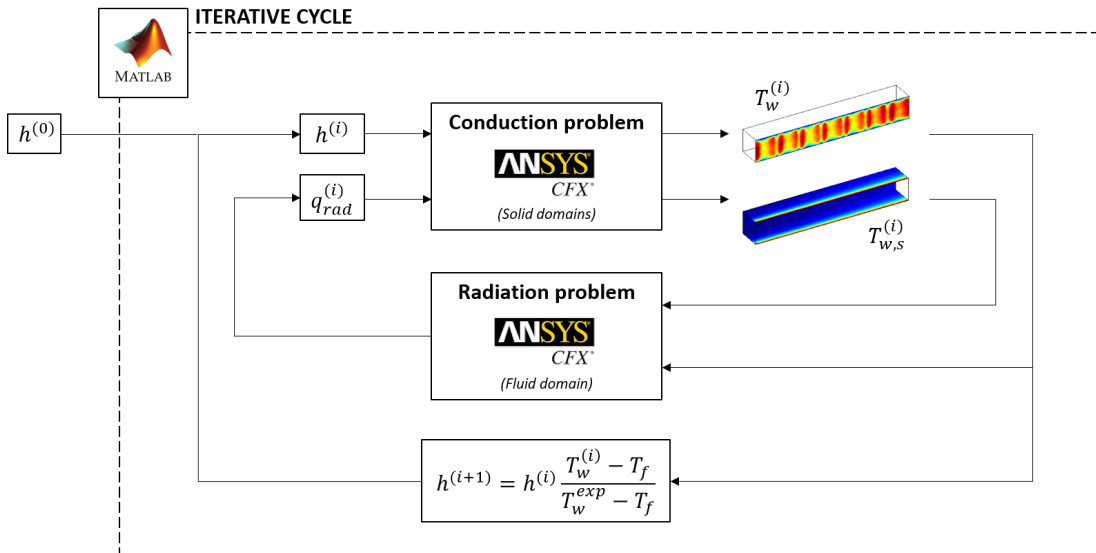


Figure 4.21: Block diagram of the heat transfer evaluation procedure

In the i -th iteration, the attempting heat transfer coefficient distribution of the ribbed wall $h^{(i)}$ is read from a file, and it will be a boundary condition for the ANSYS conduction model. The simulation calculates the temperature distribution at the inner channel surfaces. The temperature distributions of all surfaces are used as boundary conditions for the radiation problem, which evaluates the

radiative surface heat fluxes. These heat fluxes are the ulterior boundary conditions for the conduction problem at $(i+1)$ iteration. Meanwhile, the temperature distribution of the ribbed wall $T_w^{(i)}$ is compared with the one obtained from the thermography T_w^{exp} . Considering a point onto this surface, if the simulated temperature is greater than the experimental ($T_w^{(i)} > T_w^{exp}$), then this means that the attempting value for the heat transfer coefficient $h^{(i)}$ was too low. Therefore, a correction step adjusts the heat transfer value for the next iteration as:

$$h^{(i+1)} = h^{(i)} \frac{T_w^{(i)} - T_f}{T_w^{exp} - T_f} \quad (4.17)$$

The iterative loop continuously modifies the heat transfer distribution as long as a high error between measured and calculated temperature occurs. A perfect convergence can not be obtained because of the noisy nature of the experimental temperature distribution. For this reason, it has been preferred to stop the procedure always after six iterations and check the heat transfer convergence. Figure 4.22 reports the trends of heat transfer coefficient values extracted in three regions of the 9th inter-rib area for the static test with only the ribbed wall heated. The values become almost stable after the third iteration, and similar behaviour can be found in all the elaboration of the other tests.

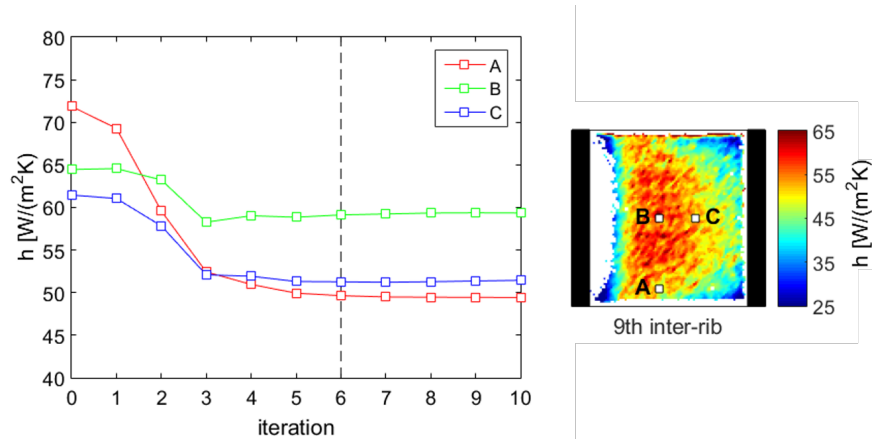


Figure 4.22: Example of the heat transfer coefficient trends over loop iterations

The initial estimation of the heat transfer coefficient $h^{(0)}$ for the ribbed wall neglects the heat losses and is calculated as:

$$h^{(0)} = \frac{q_{joule}}{T_w^{exp} - T_f} \quad (4.18)$$

The thermography delivers the wall temperature in the regions in which the liquid crystals are in the transition colour range, hence $h^{(0)}$ can only be estimated in those areas. On the other hand, the iterative procedure requires a continuous boundary condition. Therefore, constant heat transfer coefficients fill out the blank regions within two consecutive ribs to overcome this issue. The heat transfer coefficient values are extracted from the trend of the nearby known distribution. Besides, the turbulator features are not taken into account in the

conduction model, since the temperatures of their free side are not available from the experiments. Consequently, their behaviour is simulated through the imposition of a heat transfer enhancement factor of about 2, 3. This introduces a little approximation that will be discussed further in Appendix B.2, in which a sensitivity analysis will show the influence of all the assumptions made to define the boundary conditions.

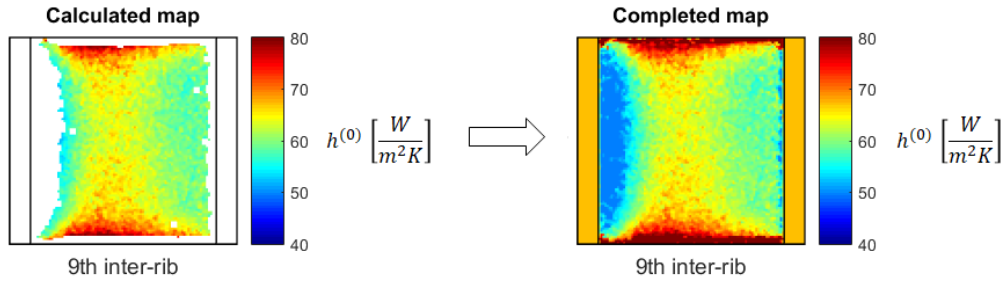


Figure 4.23: Example of heat transfer coefficient distribution for first attempt

Figure 4.23 reports the evaluated heat transfer coefficient distribution for the starting attempt, the distribution is calculated by means of Eq. 4.18 (map on the left) and after that is completed in all the blank areas (map on the right).

4.4 Temperature gradient calibration data processing

The calibration is carried out using the calibration facility explained in Par. 3.3.1. Once the system has reached a stationary condition, the thermocouple signals are acquired at 2 Hz sampling frequency for a period of 10 s . Meanwhile, the camera captures the image of the colour transition of the liquid crystals. The thermocouple readings are averaged over time and afterwards, a quadratic polynomial function spatially interpolate the temperatures in order to obtain the following relationship:

$$T(x) = k_0 + k_1x + k_2x^2 \quad (4.19)$$

A user-ROI is defined in the acquired image and this selection must contain the entire colour band of the liquid crystals, as illustrated in Fig. 4.24. The colour transition reveals an almost one-dimensional gradient in the aluminium slab along the x -direction. Furthermore, the different colour bandwidth between wide and narrow-banded liquid crystals is possible to appreciate. A Matlab routine extracts the red, green, and blue signals for each pixel of the ROI and associates these data to the respective position in the physical space by using the space transformation function. Then, the colour values are averaged in the direction perpendicular to the temperature gradient one.

At this point, the post-processing runs on in different ways depending on which type of liquid crystals (wide-banded or narrow-banded) shall be calibrated.

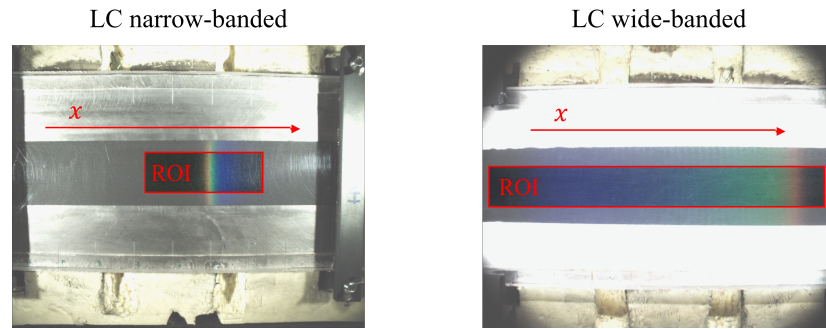


Figure 4.24: Liquid crystals calibration images

Calibration of narrow-banded liquid crystals

The maximum of the green colour signal is searched for the narrow-banded liquid crystals, as illustrated in Fig. 4.25. The peak finding procedure is the same described in Par. 4.2.2, with the difference that the signal in the current case takes place over space instead of time. The calibration temperature of the liquid crystal is evaluated substituting the coordinate of the green maximum intensity in Eq. 4.19:

$$T_w = T(x_G) = k_0 + k_1 x_G + k_2 x_G^2 \quad (4.20)$$

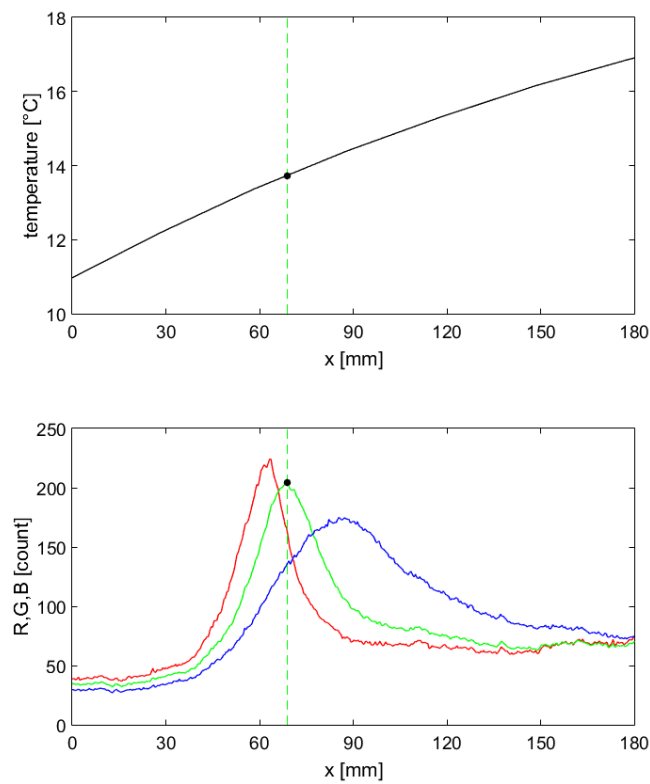


Figure 4.25: Maximum colour intensity method in temperature gradient calibration

Calibration of wide-banded liquid crystals

For the wide-banded liquid crystals, the RGB data set are converted in the HSL colour space [49], and consequently, hue values are extracted. Figure 4.26 reports the temperature and hue distribution along the aluminium slab in a calibration test. The calibration curve g is defined by means of a N -degree polynomial function, in the range in which the relationship hue-temperature has a monotonous trend (confidence range):

$$T_w = g(\text{hue}) = \sum_{i=1}^N k_i \text{hue}^i \quad (4.21)$$

where the coefficient values k_i are calculated applying the ordinary least squares method. The degree of the polynomial is chosen so as better fit the experimental data.

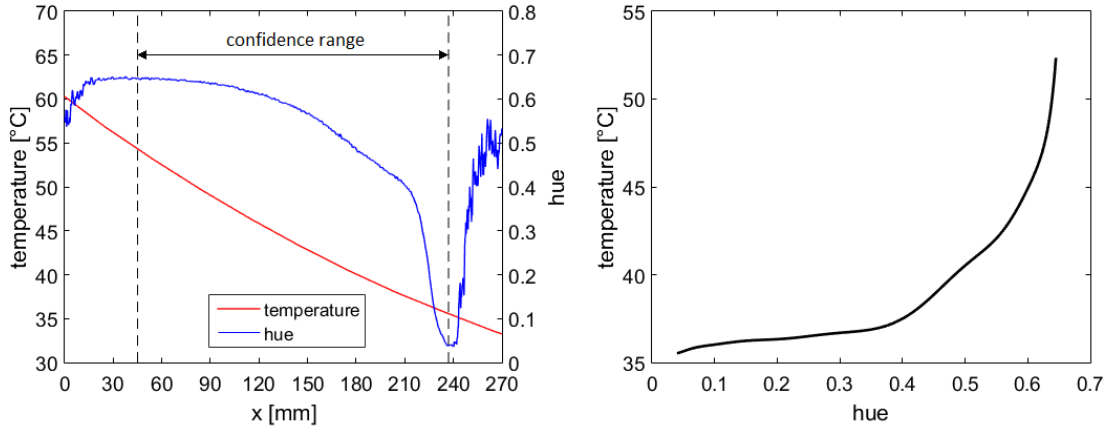


Figure 4.26: Hue method in temperature gradient calibration

4.5 Temperature evolution calibration data processing

Figure 4.27 reports the fluid and wall temperature evolutions during a static transient test, at location $y = 625 \text{ mm}$ and $z = 30 \text{ mm}$ (the considered point is near the middle of the 9-th inter-rib). The fluid temperature is extracted from the interpolated distribution of the thermocouples signals, meanwhile, the wall temperature evolution is computed by using Eq. 4.12.

Furthermore, Fig. 4.27 shows the trends of the cooling rates. The wall cooling rate is always greater than $0.1^\circ\text{C}/\text{s}$ and such consideration can be extended also for the other tests. The value of the wall cooling rate is driven by the fluid temperature, which in turn is imposed by the air treatment section in order to achieve tests that fulfilling the one-dimensional conduction assumption.

The calibration facility described in Par. 3.3.2 allows to monitor and control the temperature evolution of the copper plate. However, the maximum attainable cooling rate is about $0.015^{\circ}\text{C}/\text{s}$ that is lower by one order of magnitude than the rate in the transient tests. Despite the limited cooling rate, the facility allows to pursue the set aims anyway. In a possible further development, the potential effect of different temperature rate on the calibration values may be studied.

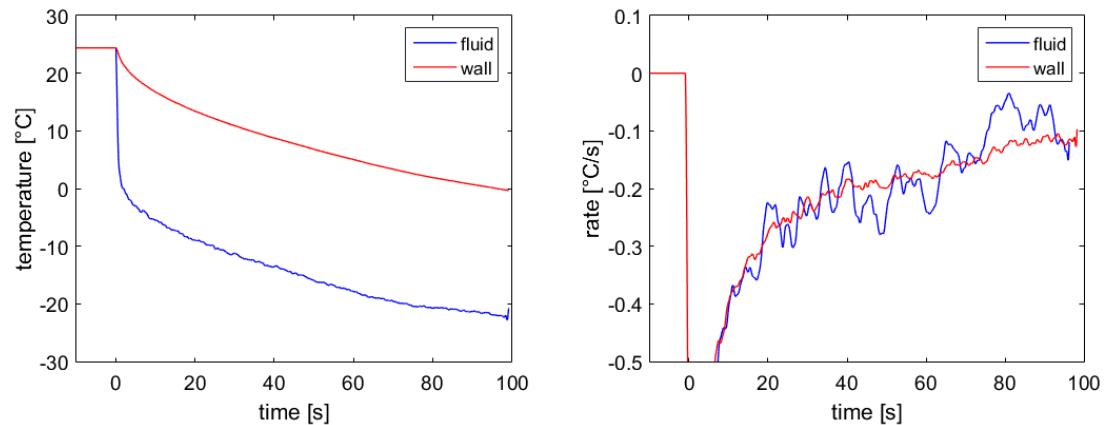


Figure 4.27: Wall and fluid temperature evolutions and relative cooling rates for a transient test

The calibration test starts at ambient temperature then the cooling rate is maintained at about $0.01^{\circ}\text{C}/\text{s}$ until the entire colour transition occurs. After that, the copper plate has been left free to warm again to ambient temperature. The temperatures are read with a sampling frequency equal to 2.8 Hz and the images are recorded in sync only once the colour transition happens to preserve memory. It is expected at least two hours between consecutive calibrations for the temperature evolution approach.

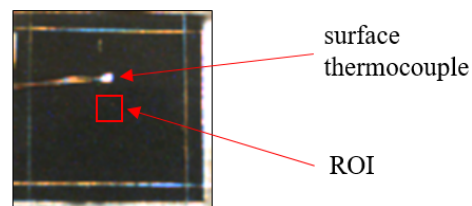


Figure 4.28: Region of interest (ROI) for averaging colour signals in temperature evolution approach

A region of interest of area 10×10 pixels is selected just below the thermocouple used to evaluate the surface temperature, as shown in Fig. 4.28. In the ROI, the colours are averaged to remove spatial noise from the images. An example of the evolution of the primary colours are reported in Fig. 4.29. Since the colour transition of the liquid crystals is passed two times in opposite directions, two peaks for each colour take place. The already described Matlab routine finds the

moments in which the green colour peaks are reached. Then, the surface temperatures at those instants are associated as calibration temperatures, and moreover, the temperature rates are evaluated.

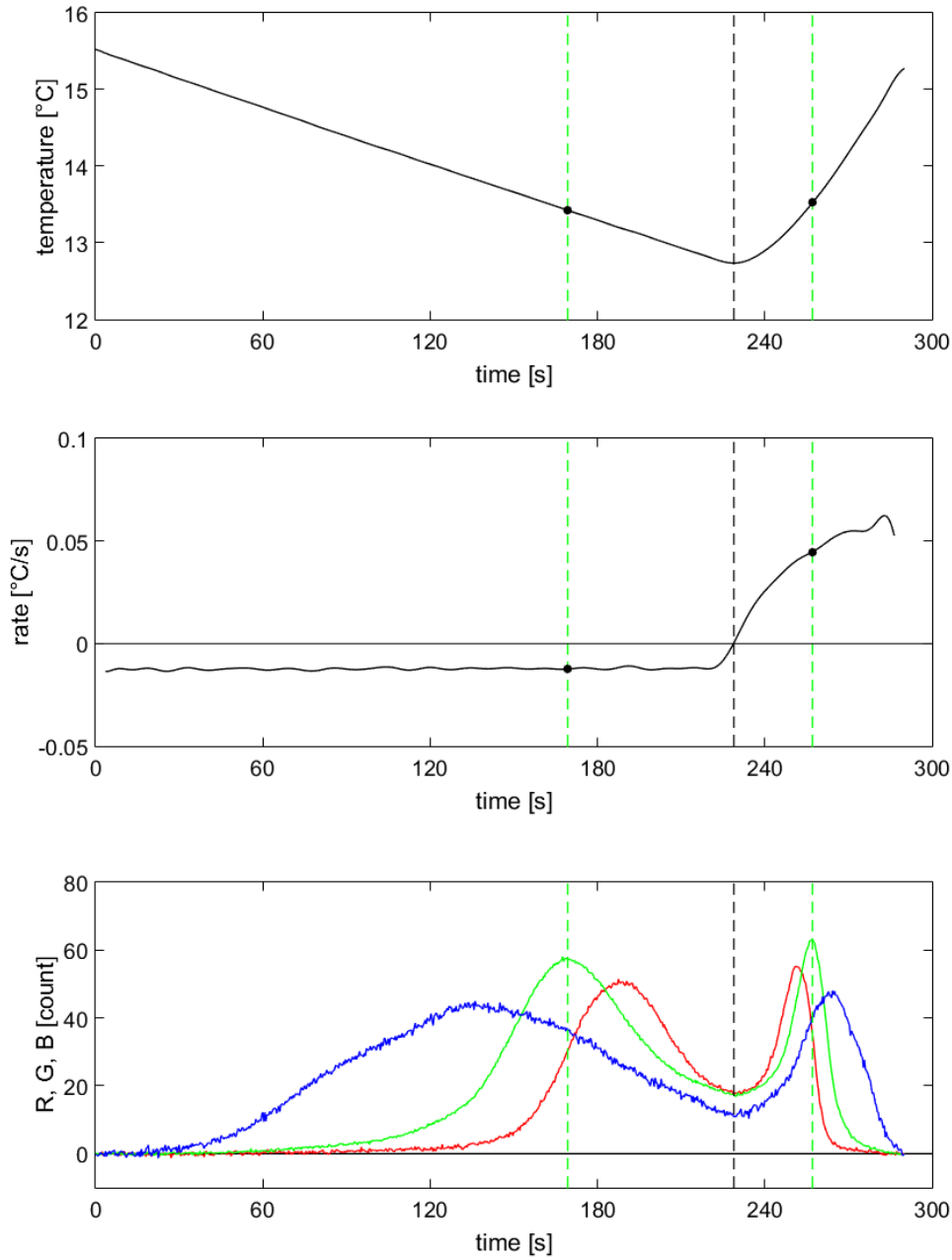


Figure 4.29: Maximum colour intensity method in temperature evolution approach

Chapter 5

Results

5.1 Liquid crystals calibration

5.1.1 Wide-banded liquid crystals

The liquid crystal R35C7W employed in the steady-state thermography was calibrated thanks to the temperature gradient apparatus. Multiple calibrations were performed over time, as reported in Tab. 5.1, in order to study the effect of the liquid crystal ageing on the calibration curve. The calibrations were accomplished the day after the liquid crystal painting, after two weeks, and after the third week. For each day, two calibration curves (indicated with morning and afternoon in Tab. 5.1) were extracted to check the calibration repeatability; at least 6 hours of waiting time were interposed between successive calibrations.

Table 5.1: Calibration tests matrix for R35C7W

| Test number | Day number | |
|-------------|------------|-----------|
| 1 | 1 | Morning |
| 2 | 1 | Afternoon |
| 3 | 14 | Morning |
| 4 | 14 | Afternoon |
| 5 | 21 | Morning |
| 6 | 21 | Afternoon |

Figure 5.1 provides all the calibration results for the wide-banded liquid crystal. The calibration curves collected in the same day are overlapped, therefore they are averaged and interpolated by 15th-degree polynomial functions in the Hue range within 0.05 and 0.65. The right graph of Fig. 5.1 shows the hue-temperature functions of each calibration day. The liquid crystal ageing occurs mainly with the attenuation of the colour intensity, and consequently, with the alteration of the calibration curves. This behaviour results also in the study conducted by Wiberg et al. [53]. In the current case, the ageing does not dramatically affect the hue-temperature function within the three investigated weeks.

In any case, the wall temperatures were evaluated using the calibration curve of the first week, since all the heat transfer coefficients measurements with the steady-state approach were performed in this period.

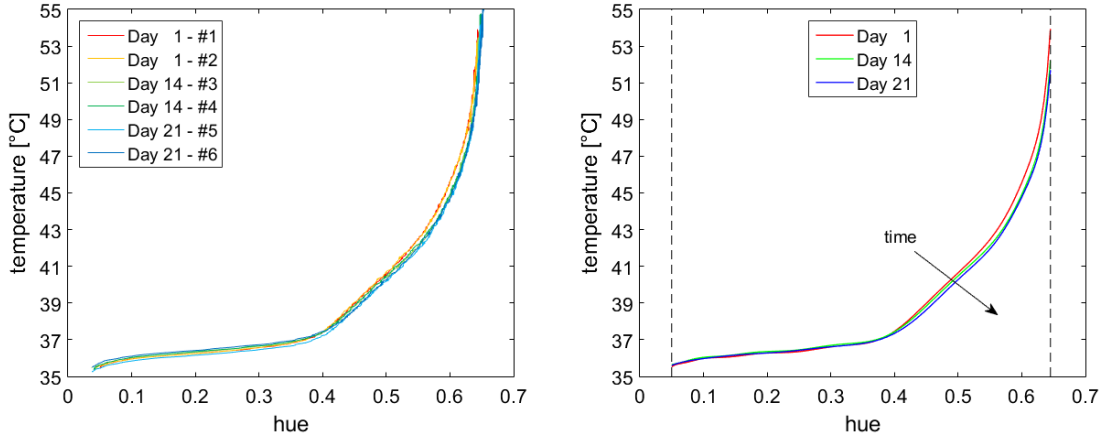


Figure 5.1: Hue-temperature calibration of R35C7W

5.1.2 Narrow-banded liquid crystals

The calibration temperatures values were obtained by means of both calibration facilities and for both types of liquid crystals employed in the transient LC thermography tests.

The R13C1W liquid crystal was sprayed at the same time on the calibration plates of both facilities to ensure consistent performances. After the calibration tests of this liquid crystal, the surfaces of the facilities were cleaned and prepared to calibrate the R3C1W one. For reasons of clarity, the resulting liquid crystals calibrations are presented by facility instead of chronological order.

Several calibrations were performed over four days using the temperature gradient approach and the temperature evolution approach, in order to evaluate possible differences between the two calibration methods and the effect of liquid crystals ageing. The calibration values are reported in Tab. 5.2 for the temperature gradient approach, and in Tables 5.3, 5.4 for the temperature evolution approach.

Table 5.2: Calibration temperature of R13C1W and R3C1W liquid crystals resulting from temperature gradient approach

| Test number | Day number | Calibration temperature | |
|-------------|------------|-------------------------|---------------|
| | | R13C1W [°C] | R3C1W [°C] |
| 1 | 1 | 13.71 | 3.69 |
| 2 | 2 | 13.80 | 3.90 |
| 3 | 3 | 13.77 | 3.92 |
| 4 | 4 | 13.79 | 3.60 |

Table 5.3: Calibration temperature of R13C1W liquid crystal resulting from temperature evolution approach

| Test number | Day number | COOLING | | HEATING | |
|-------------|------------|-------------------|-------------------------|-------------------|-------------------------|
| | | Rate | Calibration temperature | Rate | Calibration temperature |
| | | [$^{\circ}C/s$] | [$^{\circ}C$] | [$^{\circ}C/s$] | [$^{\circ}C$] |
| 1 | 1 | -0.012 | 13.58 | 0.050 | 13.66 |
| 2 | | -0.012 | 13.62 | 0.048 | 13.70 |
| 3 | | -0.011 | 13.64 | 0.049 | 13.72 |
| 4 | | -0.012 | 13.66 | 0.049 | 13.74 |
| 5 | 2 | -0.011 | 13.69 | 0.051 | 13.80 |
| 6 | | -0.012 | 13.71 | 0.050 | 13.80 |
| 7 | | -0.012 | 13.72 | 0.051 | 13.80 |
| 8 | | -0.012 | 13.69 | 0.050 | 13.79 |
| 9 | 3 | -0.012 | 13.69 | 0.049 | 13.78 |
| 10 | | -0.012 | 13.70 | 0.049 | 13.79 |
| 11 | | -0.012 | 13.71 | 0.049 | 13.80 |
| 12 | 4 | -0.012 | 13.73 | 0.049 | 13.83 |
| 13 | | -0.012 | 13.74 | 0.050 | 13.82 |
| 14 | | -0.012 | 13.72 | 0.051 | 13.81 |

Table 5.4: Calibration temperature of R3C1W liquid crystal resulting from temperature evolution approach

| Test number | Day number | COOLING | | HEATING | |
|-------------|------------|-------------------|-------------------------|-------------------|-------------------------|
| | | Rate | Calibration temperature | Rate | Calibration temperature |
| | | [$^{\circ}C/s$] | [$^{\circ}C$] | [$^{\circ}C/s$] | [$^{\circ}C$] |
| 1 | 1 | -0.010 | 3.61 | 0.048 | 3.81 |
| 2 | | -0.010 | 3.65 | 0.048 | 3.83 |
| 3 | | -0.010 | 3.68 | 0.048 | 3.84 |
| 4 | | -0.009 | 3.68 | 0.049 | 3.85 |
| 5 | 2 | -0.011 | 3.70 | 0.049 | 3.85 |
| 6 | | -0.011 | 3.69 | 0.049 | 3.87 |
| 7 | | -0.011 | 3.72 | 0.050 | 3.85 |
| 8 | | -0.010 | 3.72 | 0.049 | 3.88 |
| 9 | 3 | -0.010 | 3.77 | 0.049 | 3.93 |
| 10 | | -0.011 | 3.79 | 0.049 | 3.94 |
| 11 | | -0.010 | 3.78 | 0.049 | 3.93 |

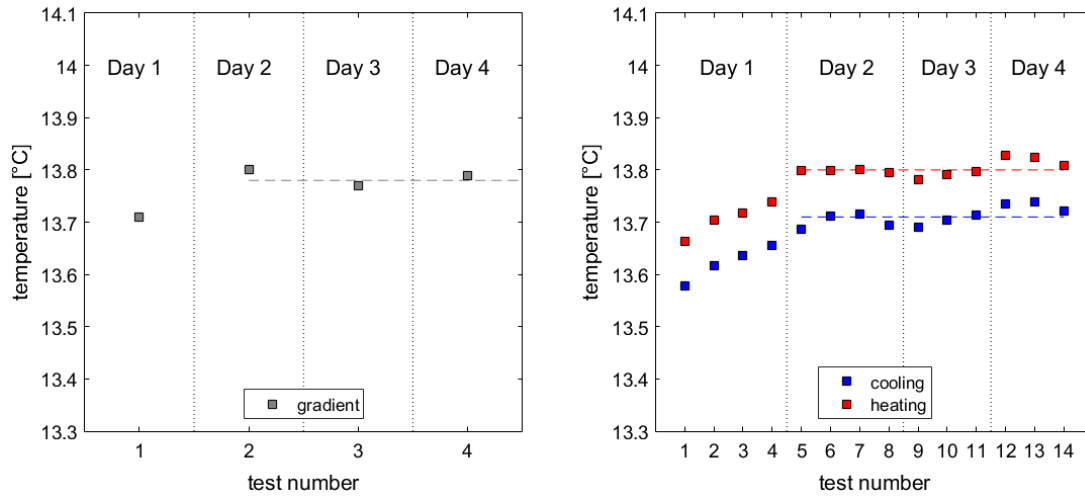


Figure 5.2: Trends of R13C1W calibration temperature for the different calibration approaches

Figure 5.2 shows the calibration outcomes of the R13C1W liquid crystal over days. The trends of the calibrations obtained in the temperature gradient approach or temperature evolution approach are reported on the left and right graphs, respectively. On the first day, the calibration temperatures are inconsistent, but after the values become almost stable in both calibration approaches. Therefore, only the results that come from the second day will continue to be taken into account. In light of this fact, the test channel underwent several cooling in order to perform a number of colour transition cycles to the liquid crystals, and the transient tests were performed only from the second day onwards. Furthermore, the colour response of the liquid crystal is different on cooling and heating: the green peaks occurred at a lower temperature when cooled rather than heated. A lot of studies have addressed this known behaviour, but considering liquid crystals in which the colour transition takes place above the ambient temperature [1, 2, 25]. This hysteresis phenomenon is repeatable and is due to the intrinsic properties that characterize the specific type of liquid crystals.

In Tab. 5.5 the average calibrations of the two liquid crystals are calculated for:

- *Cooling*, calibration temperature obtained over the temperature decreasing phase in the temperature evolution approach;
- *Steady-state*, calibration temperature evaluate in the temperature gradient approach;
- *Heating*, calibration temperature defined during the system restoring to room temperature in the temperature evolution approach;

Besides, a clear presentation of the calibration results is given by the bar graphs of Fig. 5.3. The cooling calibration is lower than heating one even for the R3C1W liquid crystal. Nevertheless, the gradient temperature approach provided calibration temperatures that are amid the cooling and heating calibration values.

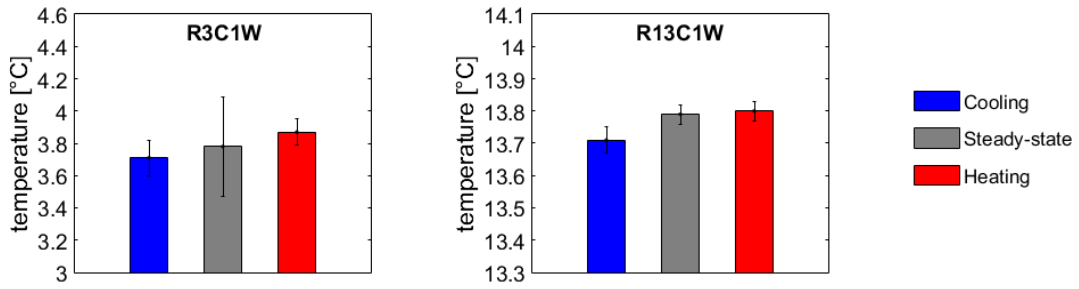


Figure 5.3: Comparison between the calibration temperatures obtained from the different calibration approaches

Table 5.5: Summary of liquid crystals calibration temperatures

| R3C1W | | | R13C1W | | |
|------------|--------------|------------|------------|--------------|------------|
| Cooling | Steady-state | Heating | Cooling | Steady-state | Heating |
| 3.71 | 3.78 | 3.87 | 13.71 | 13.79 | 13.80 |
| ± 0.11 | ± 0.31 | ± 0.08 | ± 0.04 | ± 0.03 | ± 0.03 |

The results prove that it is not correct to simply assume the same calibration temperature for heating, cooling and the steady-state of liquid crystals. Therefore the assigned calibration value has to be that obtained during the most similar condition to that in which liquid crystals undergo during transient tests. In the present work, the inner surface temperatures of the test channel decrease over time. Consequently, the cooling calibration value has to be used as wall temperature, and therefore, temperature gradient facility can't be useful to perform the calibration of the liquid crystals that are employed in the transient tests. A suggested future study is to investigate the cooling rate effect on the calibration temperature in order to get closer to the test conditions. This analysis will require several improvements to the temperature evolution calibration facility.

5.2 Heat transfer distribution

It is considered useful to provide some indications about the flow field development within the considered cooling channel in order to support the interpretation of the heat transfer distribution.

Considering the ribbed channel sketched in Fig. 5.4, in the presence of the rib the flow separates, causing a recirculation bubble downstream of the obstacle and a small vortex upstream. Downstream the rib, the main flow reattaches the channel wall (impingement zone) and a new boundary layer starts to develop. In the occurrence of rotation, how it does in the smooth channel as a result of Coriolis effects (Par 1.2.1), the core flow moves toward the trailing side. This brings in a size reduction of the recirculation bubble if the ribbed wall acts as trailing side, while an extension of the recirculation bubble is observed in the case of rib at the leading side. It becomes clear that the presence of ribs implies the generation of flow structures, which promote the wall heat transfer on the ribbed side.

Besides, also the heat transfer of the other smooth sides are increased even if to a lesser extent than the ribbed side.

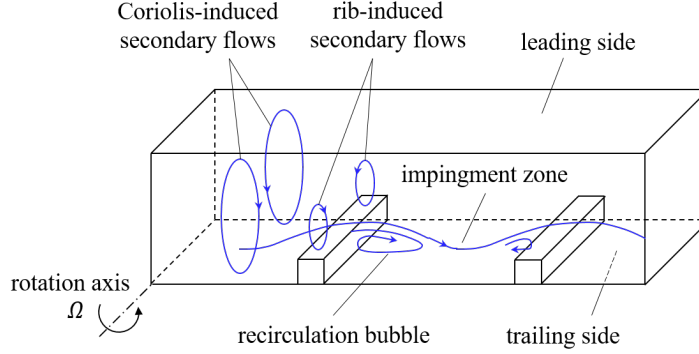


Figure 5.4: Main flow structure into a ribbed cooling channel

5.2.1 Transient tests

In order to describe the heat transfer distribution, Par. 1.2.3 has introduced dimensionless parameters that depend on several air properties, which in turns depend on the fluid temperature. In the transient test, the fluid temperature changes continuously over time, hence a reference temperature T_f^* has been defined as:

$$T_f^* = \frac{1}{t_{LC}} \int_0^{t_{LC}} T_f(t) dt \quad (5.1)$$

where t_{LC} is the time at which the green intensity reaches the maximum. By using this fluid reference temperature, the following expressions define the dimensionless wall temperature, the buoyancy parameter, and the enhancement factor:

$$\theta_w = \frac{T_w - T_0}{T_f^* - T_0} \quad Bo = \frac{T_w - T_f^*}{T_f^*} Ro^2 \frac{Y}{D_h} \quad EF = \frac{hD_h/k(T_f^*)}{0.023Re^{0.8}Pr(T_f^*)^{0.4}} \quad (5.2)$$

Unless otherwise indicated whenever average quantities will be presented, they will be the average values calculated over the two $15 \times 15 \text{ mm}^2$ windows sketched in Fig. 5.5. A window is defined for each type of liquid crystal (W_{LC3} and W_{LC13}) and is approximately located in the impingement zone.

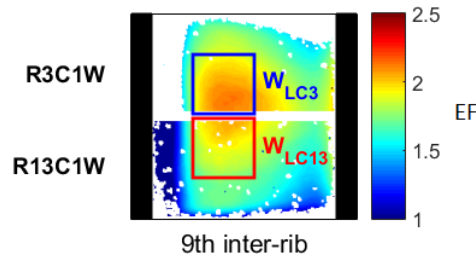


Figure 5.5: Definition of averaging windows for transient tests

It is recalled that two types of narrow-banded liquid crystals are sprayed in the two halves divided by the channel midline and they are consequently used simultaneously during the tests. The test matrix defined for the transient tests are reported in Tab. 5.6, in which the average dimensionless wall temperature is also given for each liquid crystal. From the plot of Fig. 5.6, it is possible to see that all the tests were executed within the range of the dimensionless wall temperature (i.e., $0.3 \leq \theta_w \leq 0.7$) suggested by Owen et al. [38]. Figure 5.6 reports also the error bars, which represent 1.96 times the standard deviation of the dataset.

Table 5.6: Test matrix for transient approach experiments

| Test number | Ro | θ_w | |
|-------------|------|------------|--------|
| | | R3C1W | R13C1W |
| 1 | 0 | 0.51 | 0.35 |
| 2 | 0 | 0.47 | 0.32 |
| 3 | 0.10 | 0.54 | 0.38 |
| 4 | 0.15 | 0.52 | 0.34 |
| 5 | 0.20 | 0.60 | 0.44 |
| 6 | 0.25 | 0.53 | 0.39 |
| 7 | 0.30 | 0.54 | 0.39 |
| 8 | 0.30 | 0.53 | 0.37 |

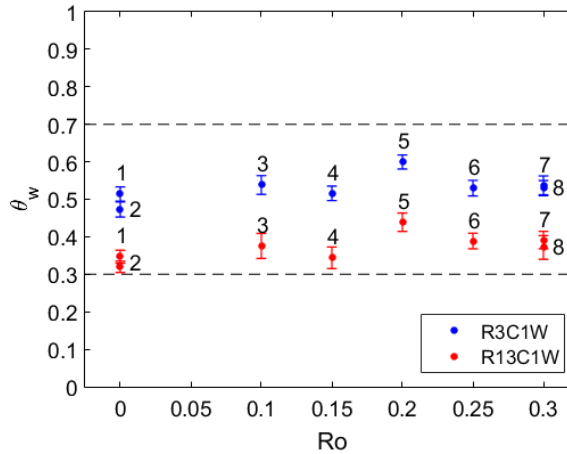


Figure 5.6: Average dimensionless wall temperature

Table 5.6 shows that in static and at the most extreme rotation condition two heat transfer distributions were achieved with different temperature evolutions imposed to the fluid, as reported in the plots of Fig. 5.7. Therefore the tests are characterized by different activation time of the liquid crystals. The comparison between the enhancement factor distributions of the 9th inter-rib (Fig. 5.8) proves that the heat transfer is the same for the two tests at the same rotation number, despite the different fluid temperature evolutions. These tests are also evidence of the good repeatability of the heat transfer measurements. For this reason, only tests 1 and 7 will be considered furthermore.

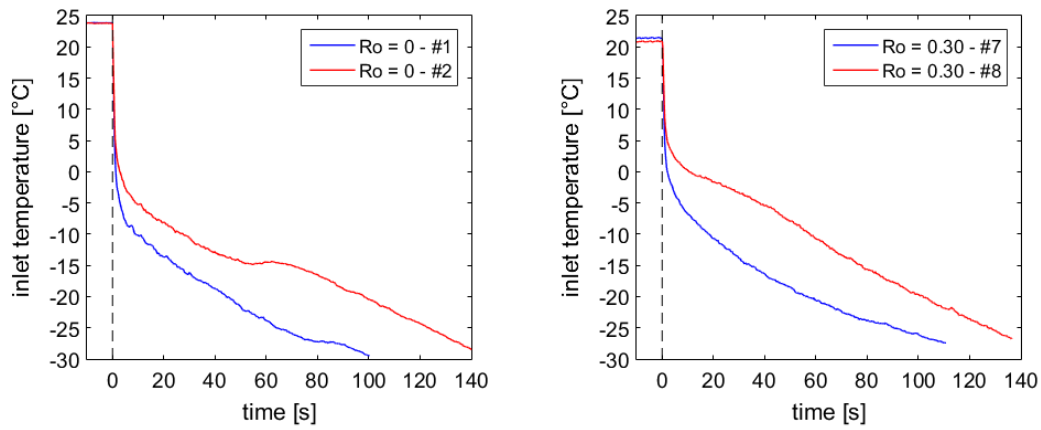


Figure 5.7: Fluid temperature evolutions for static (left side) and rotation conditions (right side)

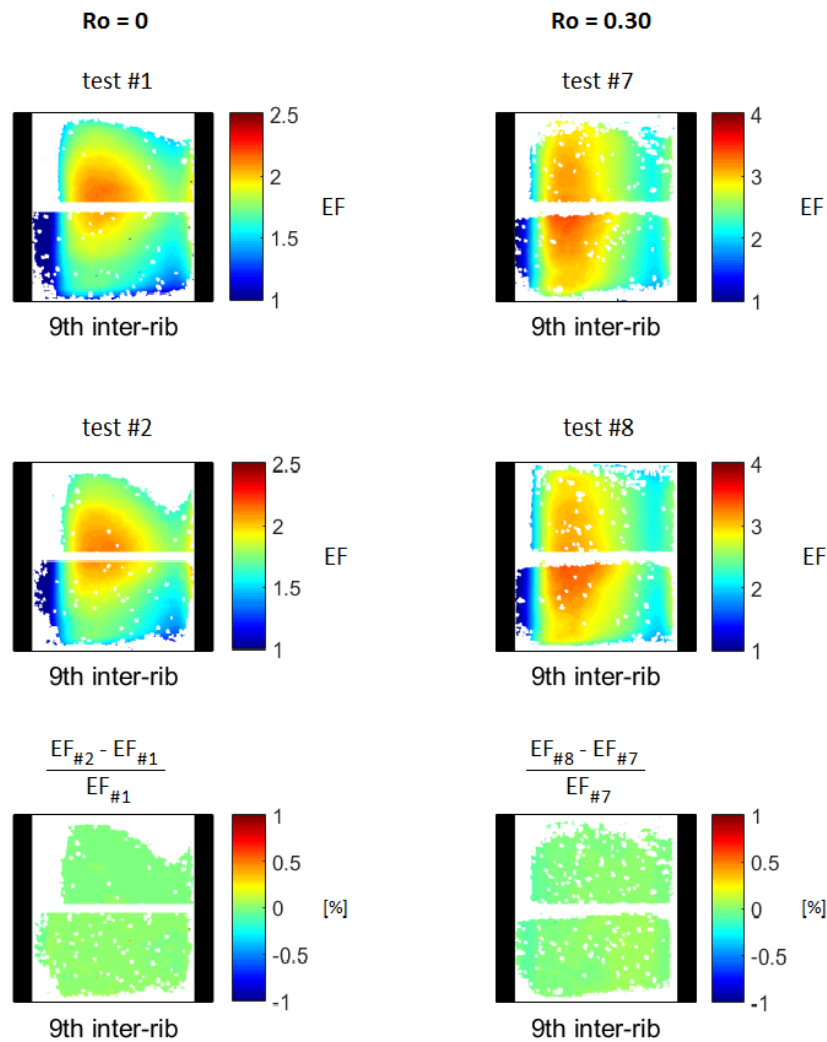


Figure 5.8: Comparison between tests carried out with different fluid temperature evolutions

The heat transfer can be qualitative compared among the different rotation conditions thanks to the maps of the enhancement factor in Figure 5.9. A similar thermal pattern behaviour occurs for all the inter-rib regions. Indeed the enhancement factor reached its peak at the central region of the inter-rib, in correspondence of the flow reattached zone as described in the preface of the Par. 5.2. On the contrary, the heat transfer is lower in the regions where the recirculation bubbles are established. The heat transfer trends across the inter-rib can also be appreciated in Fig. 5.10, in which two enhancement factor profiles are extracted along the channel length for each rotation condition:

- A profile stands for the R3C1W liquid crystal and it is obtained along the line 5 mm above the midline of the channel (at $z = 30$ mm);
- The other one shows the indications provided by the R13C1W liquid crystal along the line 5 mm below the midline of the channel (at $z = 20$ mm).

The two types of liquid crystals provide pretty much the same enhancement factor values and the difference between them is assessed using PD_{LC} , which is defined as:

$$PD_{LC} = \frac{EF_{R13C1W} - EF_{R3C1W}}{EF_{R3C1W}} \quad (5.3)$$

The plots of the PD_{LC} in Fig. 5.11 show that the difference is within about $\pm 6\%$. These values discrepancies are comparable with the measurement uncertainty estimations provided in the Par. B.1. Therefore the data achieved by means of the two liquid crystals are consistent, although they deliver the wall temperature at different time during the same tests (and so also at different fluid temperatures). In order to clearly show how the rotation conditions affect the heat transfer performance of the ribbed channel, the presentation of the results will follow this path: evaluation of heat transfer behaviour along the channel length, study of the heat transfer distribution variation within an inter-rib, and finally, global comparison of the heat transfer performances.

Figure 5.12 shows the heat transfer development along the channel by means of the area-averaged enhancement factor, which is calculated for each inter-rib over the evaluation areas of Fig. 5.5. It is possible to assert that all the inter-ribs have the same behaviour in a static condition, whereas they reveal different trends when the rotation takes place. At each rotation number conditions, it is possible to notice that several inter-ribs exchange more heat than the others. Indeed, the location of EF_{avg} maximum changes. Considering the trends of the R3C1W liquid crystals, the EF_{avg} maximum it moves upstream as the rotation increases (from the 11 ÷ 13 inter-rib at $Ro = 0.10$ to the 8 ÷ 10 inter-rib at $Ro = 0.25$), and at $Ro = 0.30$ it keeps moving upstream and a second maximum starts to grow at the last inter-ribs. This phenomenon is certainly caused by the establishment of flow coherent structures along the channel length promoted by the rotation. These structures are in continuous development along the channel radial direction, and this development is shortened in space (i.e. it takes less space) if the Ro is augmented [42].

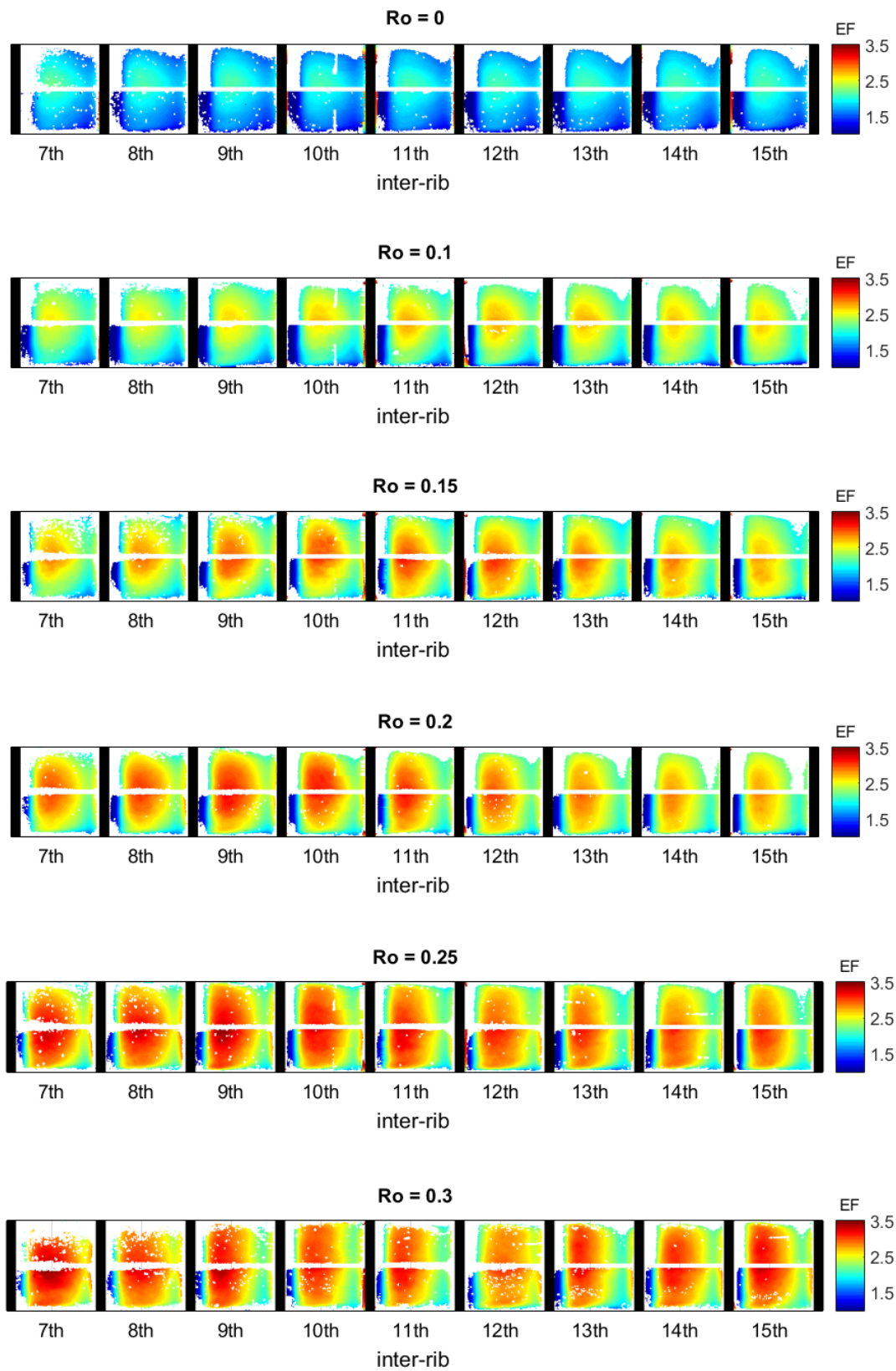


Figure 5.9: Enhancement factor maps for the different rotation conditions

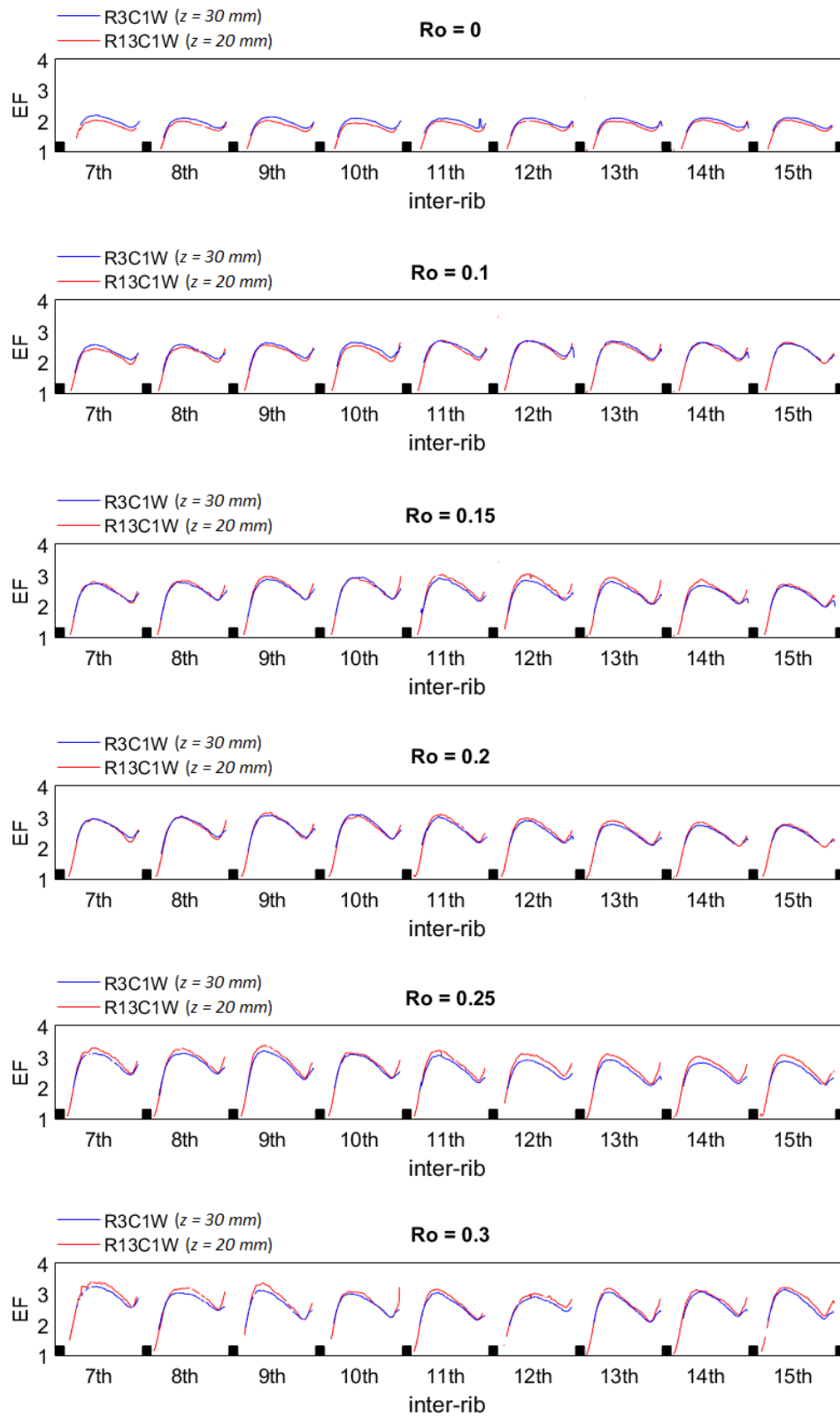


Figure 5.10: Enhancement factor profiles extracted at $z = 30$ mm (R3C1W) and $z = 20$ mm (R13C1W) for different rotation conditions

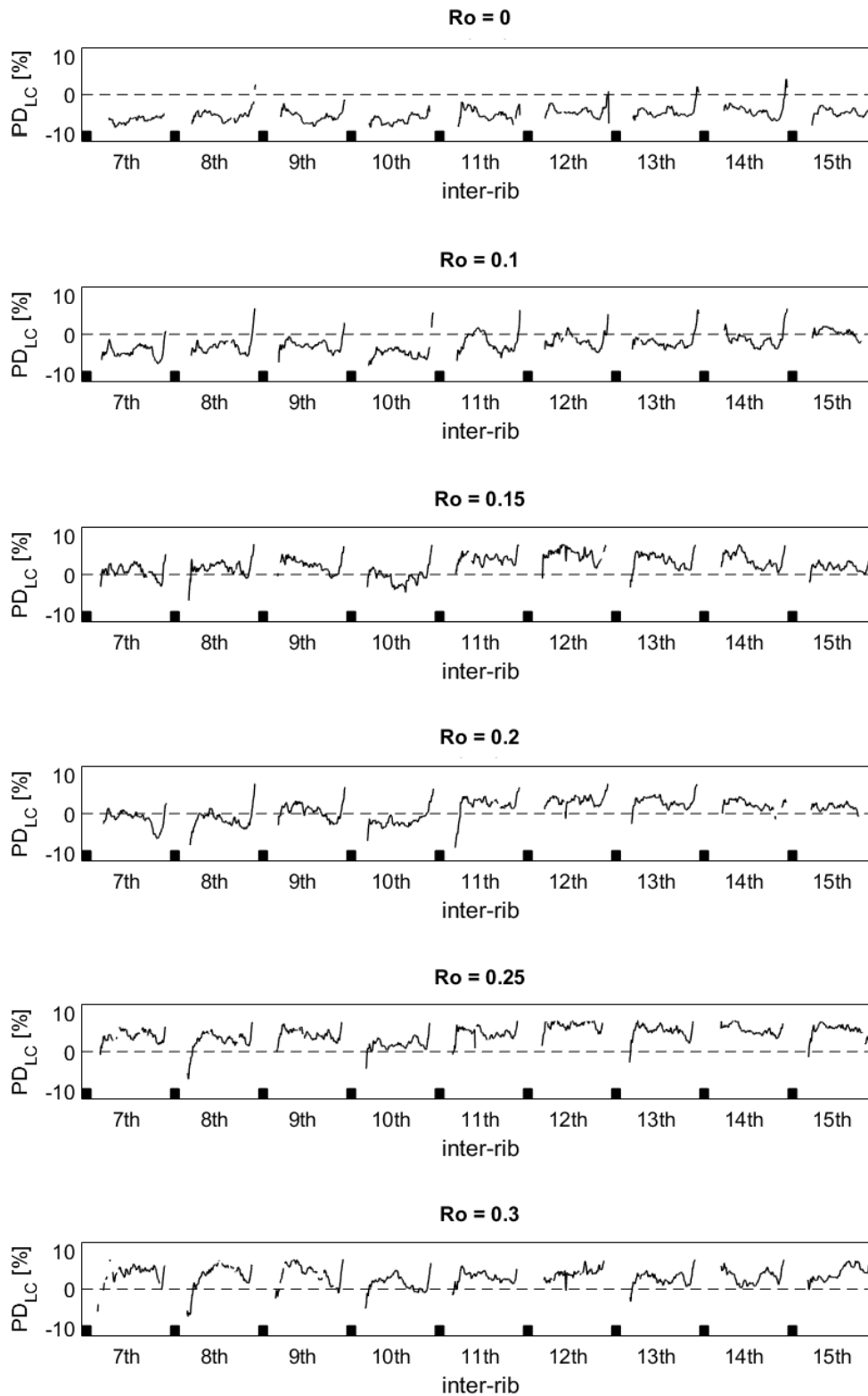


Figure 5.11: Percentage difference of the enhancement factor between the extracted profile at $z = 30\text{ mm}$ (R3C1W) and $z = 20\text{ mm}$ (R13C1W) for different rotation conditions

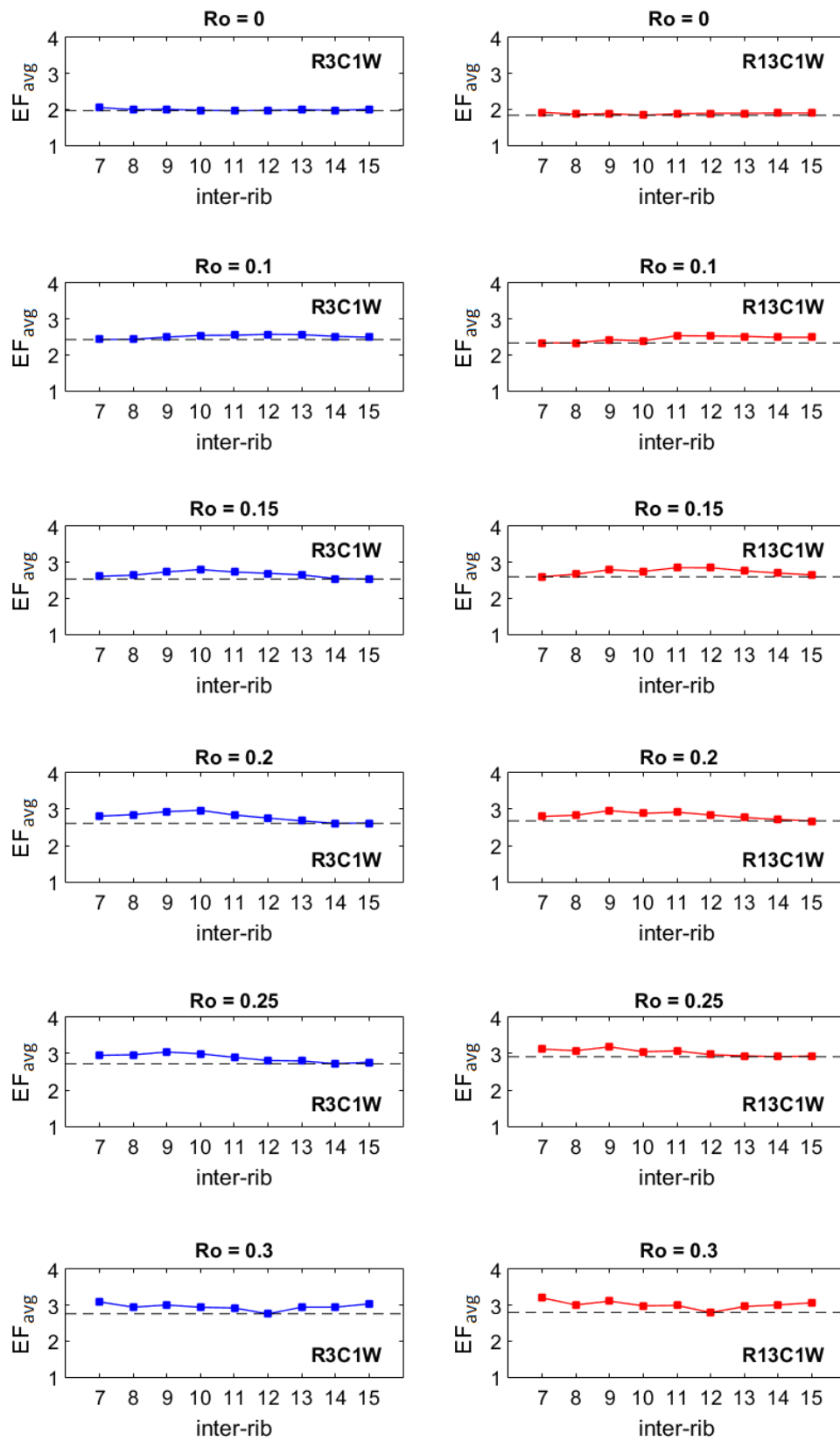


Figure 5.12: Average enhancement factor values along the channel length for different rotation conditions

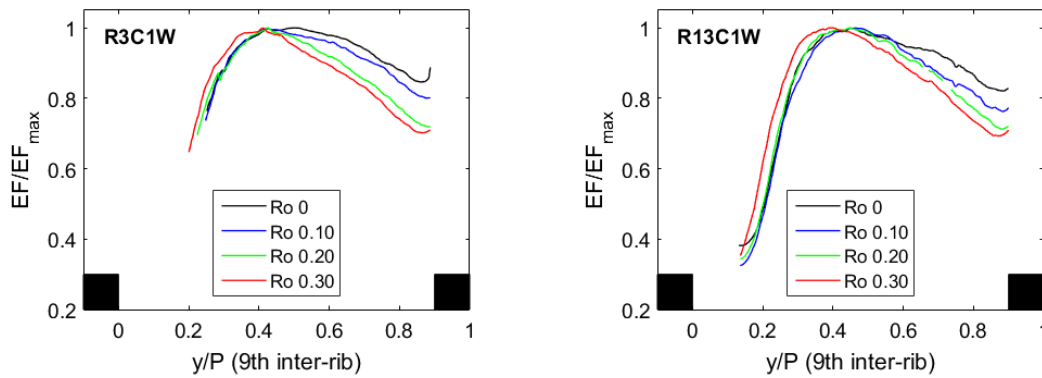


Figure 5.13: Normalized enhancement factor at the 9th inter-rib for different rotation conditions

From the maps in Fig. 5.9, it is possible to find out that the heat transfer distribution within an inter-rib becomes wider as the rotation number increases. Furthermore, the plots of Fig. 5.13 reports the enhancement factor profiles normalized with their maximum value for each rotation conditions, in order to highlight the variation of the profile shapes. These profiles are extracted across the 9th inter-rib for both liquid crystals and remain self-similar also in rotation conditions, therefore the mean flow structures don't change dramatically. However, the maximum of the heat transfer (reattachment area) moves upstream as the rotation is increased, and lower heat transfer is found where the new boundary layer develops. That is in accordance with the destabilizing effect on the boundary layer at the trailing side studied by Coletti et. al [9].

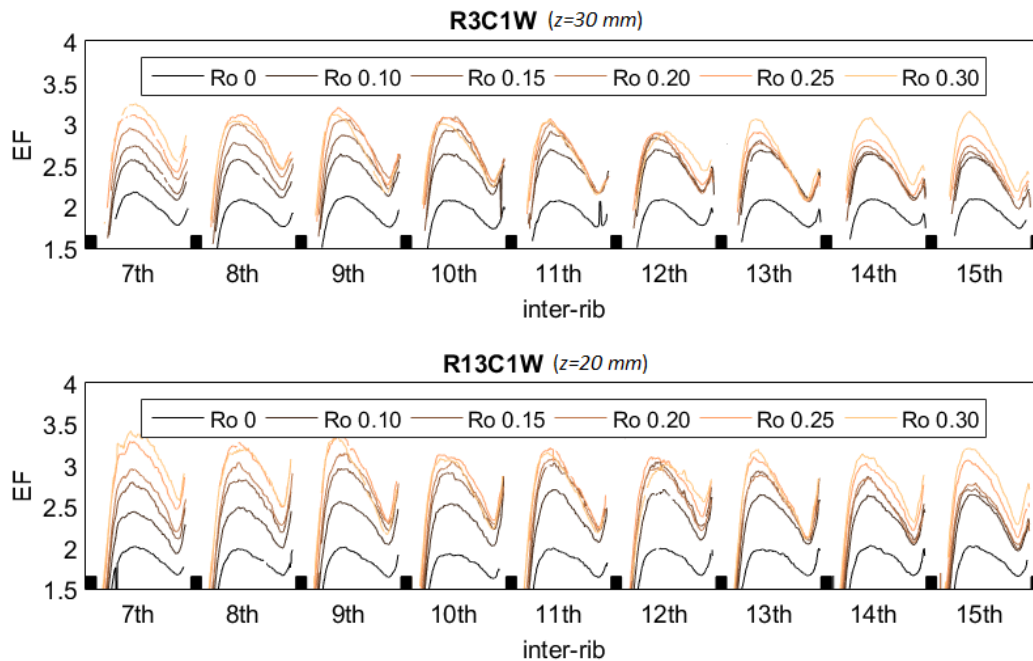


Figure 5.14: Comparison of the enhancement factor profiles for different rotating conditions

As expected augmentation of the enhancement factor can be observed at increasing angular speed, comparing the maps in Fig. 5.9 or the profiles in Fig. 5.14. This relationship is highlighted in Fig. 5.15 (on the left graph), in which the overall enhancement factors are plotted as a function of the rotation number (the overall enhancement factor is calculated averaging the average enhancement factors of each inter-rib). The data scattering can be attributed to measurement accuracy as early stated.

Furthermore, Fig. 5.15 provides the overall buoyancy parameters versus the rotation number. The Bo curves have almost parabolic trends given by the quadratic dependency ($\propto Ro^2$). The two tests carried out at rotation number equal to 0.30 (tests 7 and 8) achieve the same heat transfer despite a Bo variation more than 30%, therefore in the present study, the buoyancy effects can be neglected.

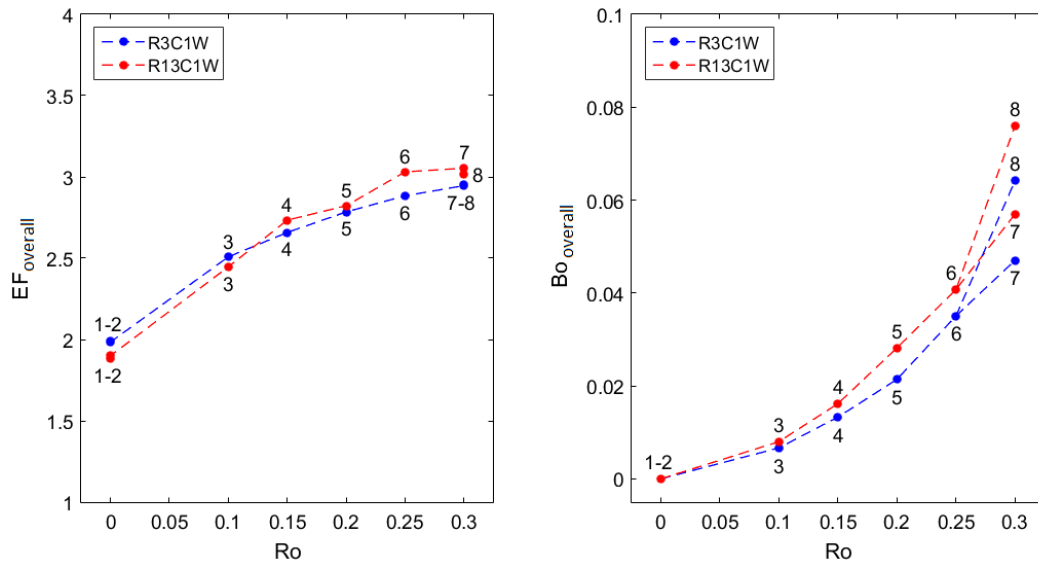


Figure 5.15: Overall enhancement factor and overall buoyancy parameter comparisons for different rotation conditions

5.2.2 Steady-state tests

The steady-state liquid crystals thermography was performed to analyze the thermal performance of the channel model in the conditions summarized in Tab. 5.7. The technical limitations of the test facility allowed to successfully accomplish the highest rotation condition at $Ro = 0.18$, slightly lower than the planned condition ($Ro = 0.2$). Anyway, this doesn't undermine the objectives to investigate the consequences on the heat transfer of the two walls heating conditions:

- *1 heated wall* (1HW), in which only the ribbed side was heated;
- *3 heated walls* (3HW), in which the ribbed and the lateral sides were heated.

Table 5.7: Test matrix for steady-state approach experiments

| Test number | Ro | Thermal boundary condition | |
|-------------|------|----------------------------|----------------|
| | | 1 heated wall | 3 heated walls |
| 1 | 0 | X | |
| 2 | 0.10 | X | |
| 3 | 0.18 | X | |
| 4 | 0 | | X |
| 5 | 0.10 | | X |
| 6 | 0.18 | | X |

For the steady-state tests, the average enhancement factor EF_{avg} are calculated over the $15 \times 30 \text{ mm}^2$ windows (Fig. 5.16), that is the area resulting from the merge of the two windows define for the presentation of the transient tests.

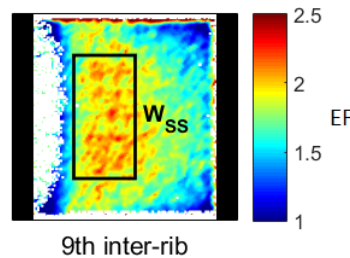


Figure 5.16: Definition of averaging window for steady-state tests

In order to point out possible differences between the heat transfer values that are obtained with the different walls heating conditions, Fig. 5.17, 5.18, 5.19 present the results of the experimental campaign for each rotation condition with this organization:

- the two maps of the heat transfer distribution relative to the two thermal boundary conditions;
- the enhancement factor profiles extracted at the channel centerline (at $z = 25 \text{ mm}$);
- the average enhancement factor values for each inter-rib.

For the static condition (Fig. 5.17), the two heat transfer distributions obtained under different walls heating conditions are pretty much the same. Unfortunately, a possible calculation of the percentage difference between the two maps wouldn't provide useful information because of the noisy nature of the experimental data. Anyway, only little discrepancies can be found in the proximity areas of lateral walls and ribs. These differences are attributed to the impact of the boundary conditions that are used in the conductive model, as described in Par. B.2 of Appendix B. However, similar EF behaviours are present in the central area along the channel length; indeed, the two midline profiles are very close.

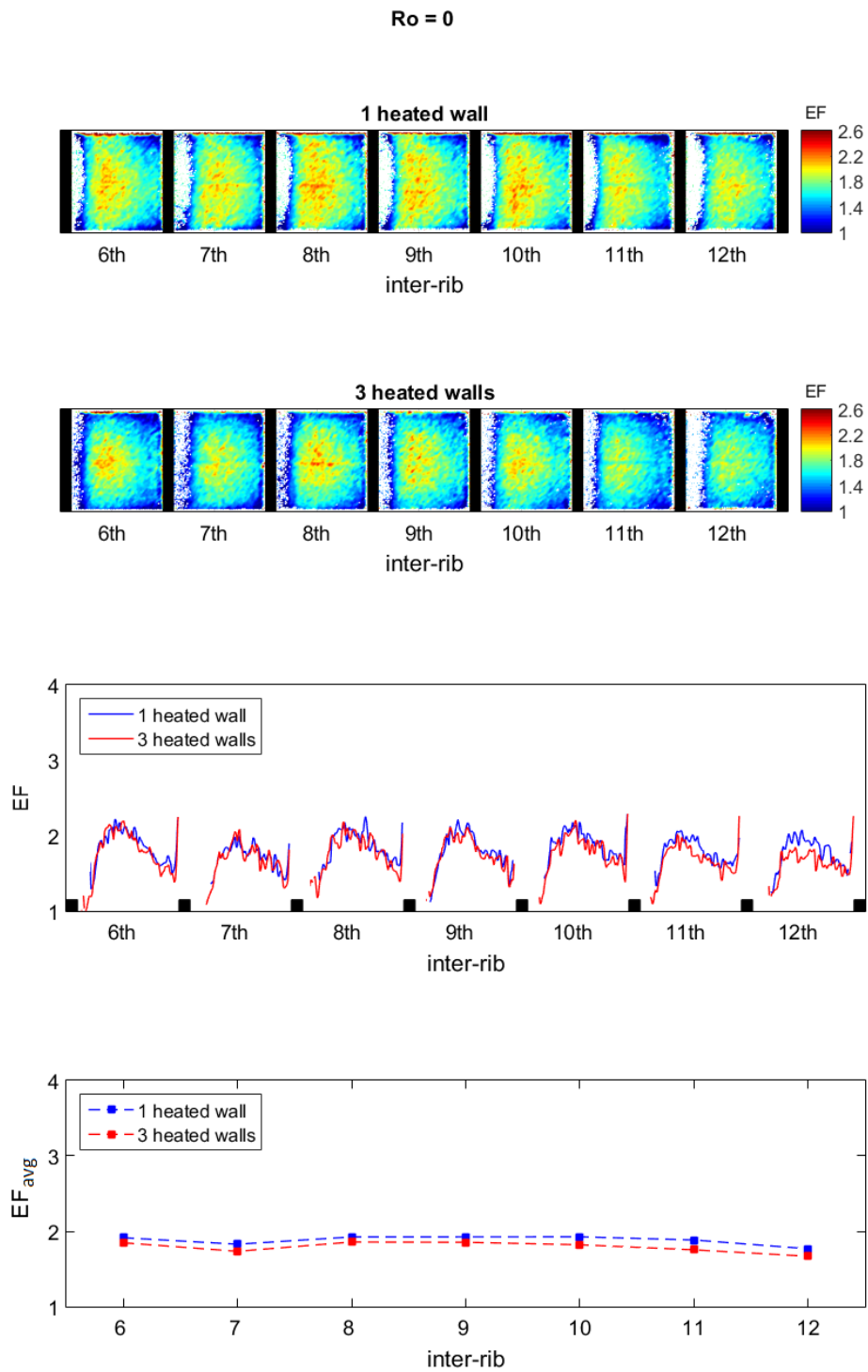


Figure 5.17: Comparison between the different heat boundary conditions for the static condition

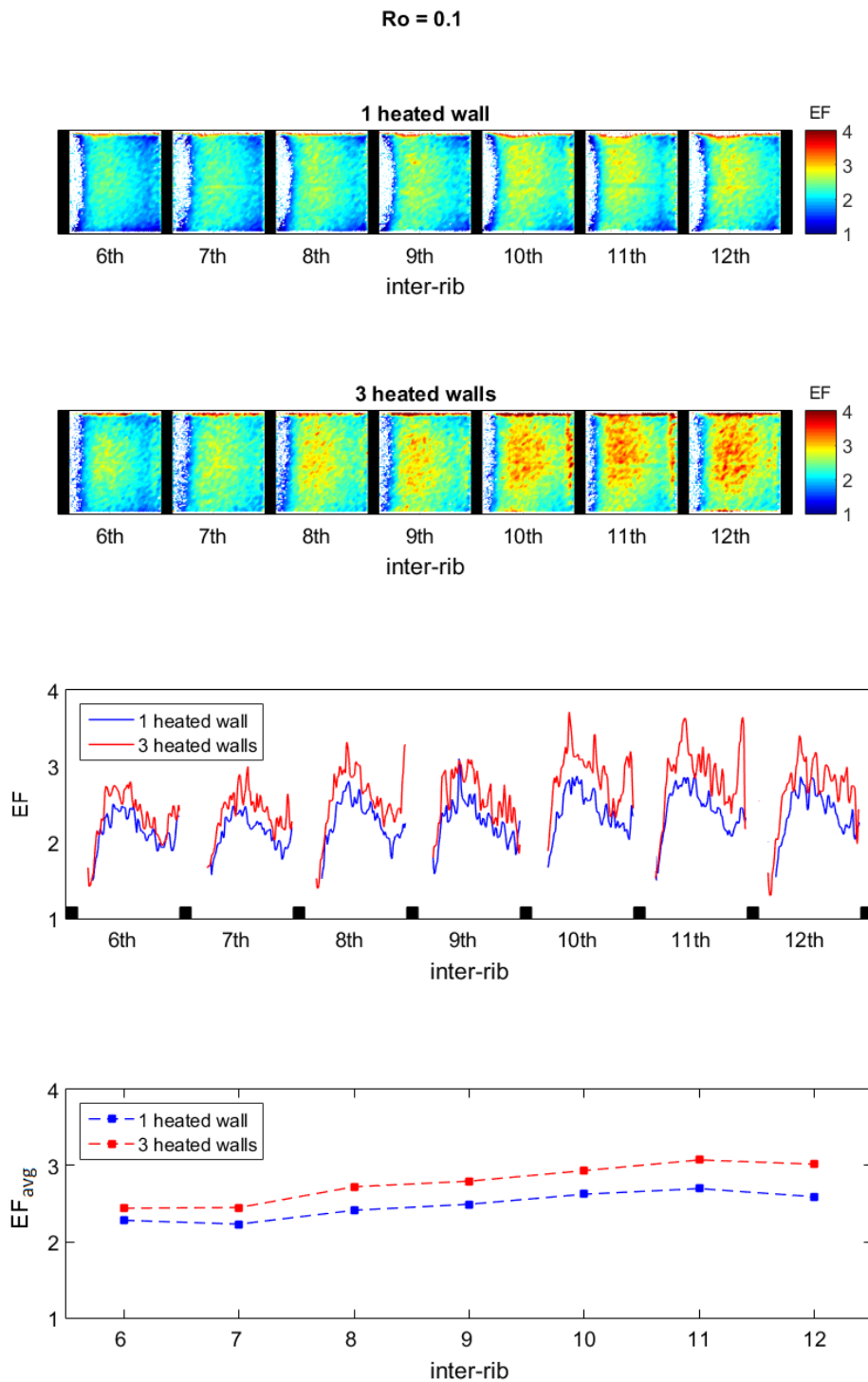


Figure 5.18: Comparison between the different heat boundary conditions for the rotation condition at $Ro = 0.1$

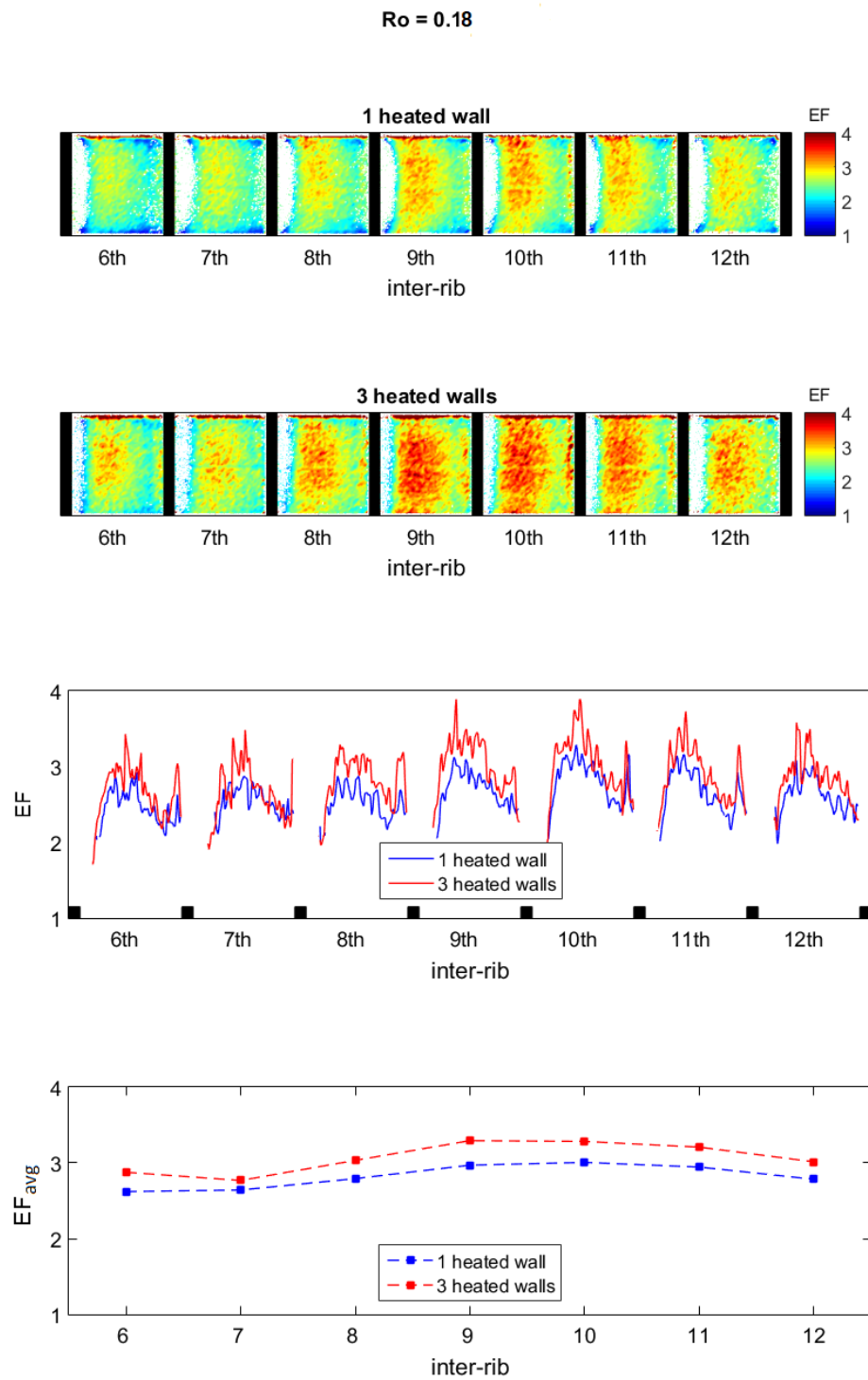


Figure 5.19: Comparison between the different heat boundary conditions for the rotation condition at $Ro = 0.18$

Therefore it is possible to assert that the heat transfer distribution is not affected by the thermal boundary condition in static condition. Further evidence of this fact is the same trend of the average values calculated for each inter-rib (the EF_{avg} maximum difference is within the 5%). On the other hand, the heating conditions significantly affect the heat transfer distribution when the rotation takes place. The maps of Figures 5.18 ($Ro = 0.1$) and 5.19 ($Ro = 0.18$) evidently show that the heat transfer distributions maintain almost the same pattern, but the EF values are much higher for the 3HW case. This is also possible to see from the comparison of the enhancement factor profiles or the EF_{avg} trends along the inter-ribs provided in the same Figures 5.18 and 5.19.

Figure 5.20 present the global comparison of the resulting overall enhancement factor that is obtained for the two heating condition. In static condition, the $EF_{overall}$ values of both thermal conditions are essentially the same. When the rotation number increases then the $EF_{overall}$ magnitude of the 3HW condition are more than 9.5% higher than 1HW case.

This behaviour is hardly imputable to systematic errors generated by data elaboration by means of the iterative procedure (Par. 4.3.3). Indeed the different configurations of walls heating generations are taken into account by the conductive model, and the radiative model estimates the radiative heat fluxes induced by the different temperature distributions on the internal channel surfaces. Moreover, a systematic bias in the data processing would affect also the static condition results. Figure 5.20 also presents the graph in which the overall buoyancy parameters are plotted as function of the rotation number. Under the same rotation condition, the $Bo_{overall}$ variations of the ribbed wall could be held accountable for the different heat transfer magnitudes that are induced by the two thermal conditions ($\Delta Bo_{overall}/Bo_{overall,1HW} = 26.2\%$ at $Ro = 0$). However, the results of the transient tests have already proved that a buoyancy parameter variation more than 30% doesn't affect the heat transfer.

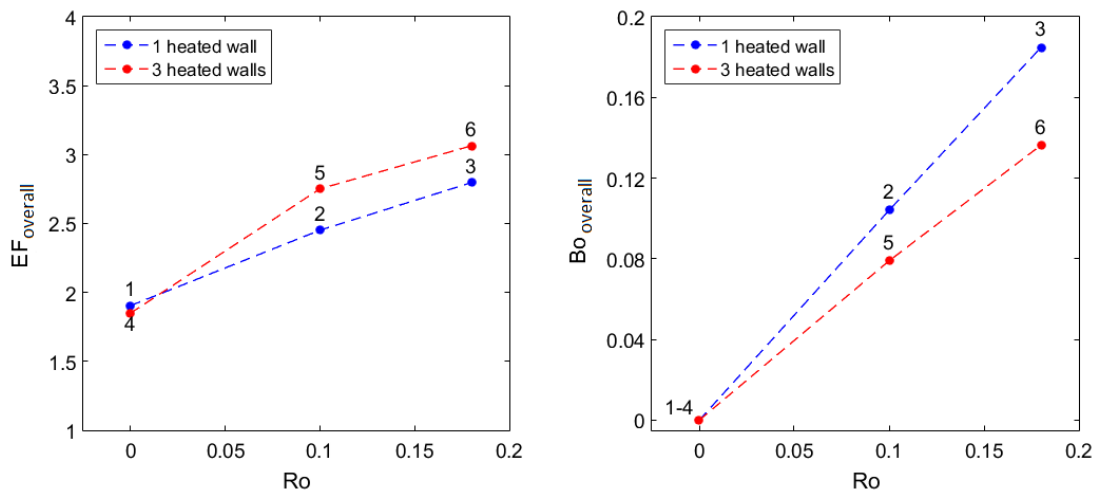


Figure 5.20: Overall enhancement factor and overall buoyancy parameter comparisons for different rotation conditions

The reason why the heat transfer level is significantly higher in the 3HW case than in the 1HW can be due to the local air density difference. When only the ribbed wall is heated, the lateral walls have temperatures lower than the case in which also they are heated. Therefore a different thermal condition of the inner channel surface is established between 1HW and 3HW cases. This induces different buoyancy effects that in turn would change the flow field during rotation, and consequently the local heat transfer coefficients.

Given the current configuration of the channel model used for the steady-state approach, there is only one optical access. This fact did not allow to experimentally investigate the flow field inside the channel in order to understand the flow mechanism coupled to the heat transfer.

Nevertheless, the simultaneous flow and heat transfer measurements are always complex and difficult in terms of methodologies and technical facilities. Indeed Wang et al. [52] investigated the impacts of the boundary heating conditions on a two-pass rotating channel with one side roughened by 45 degree inclined ribs with the help of numerical methods. The authors showed that the overall heat transfer performance of the entire first passage for all sides heated is more than 20% greater than when only the ribbed side is heated, at rotation condition equal to $Ro = 0.3$ (a similar behaviour seen in the present investigation). The different flows behaviour produced by the buoyancy effects were analyzed thanks to the numerical simulations, that allowed to assert that the change of the heat transfer is due to the alteration of the flow field.

5.2.3 Approaches comparison

Before to go into the details of the comparison between the outcomes achieved by the two approaches, the results are compared with the recent data available in the literature. Mayo et al. [33] measured the heat transfer distribution in a similar ribbed channel of aspect ratio W/H equal to 0.9 (present investigation $W/H = 1$) and for Reynolds number value of $Re = 20\,000$. The authors employed the steady-state liquid crystals thermography heating only the investigated surface. Therefore their result is compared to the steady-state approach test of this work in which only the ribbed side is heated (test 1 in Tab. 5.7).

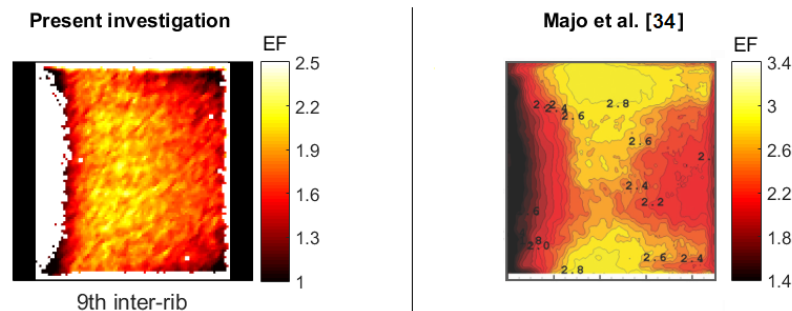


Figure 5.21: Enhancement factor distribution of the steady-state test with one heated side compared with literature result (Majo et al. [34])

Figure 5.21 provides the maps comparison with intentionally different colourmap ranges in order to highlight the distributions. The heat transfer values are almost similar along the centerlines, whereas a dramatically different behaviour can be found near the sidewalls. Indeed for the current investigation, the EF magnitude decreases going towards the sidewalls, on the contrary, two areas with highest EF values are present close to the lateral walls in the reported literature map. The authors have attributed this behaviour to the footprint of the rib-induced vortices. Although the same authors have investigated also the developed flow field inside the channel by means of the high-resolution particle image velocimetry [34], they haven't proved the strength of the flow structures that are held liable for the heat transfer enhancement in the lateral inter-rib regions. It appears quite unlikely that a secondary flow structure could be strong enough to promote heat transfer values higher than those pertaining to the flow reattachment downstream the rib. Beyond this reason, the EF distribution obtained from the measurement of this work is considered more correct than the literature contribution for another two reasons. The heat transfer behaviour accomplished with the steady-state thermography is consistent with that provided by the transient thermography as it can be possible to see by the enhancement factor map at $Ro = 0$ in Fig. 5.9, in which the maximum heat transfer is reached at the impingement zone and then it decreases moving closer to the lateral walls.

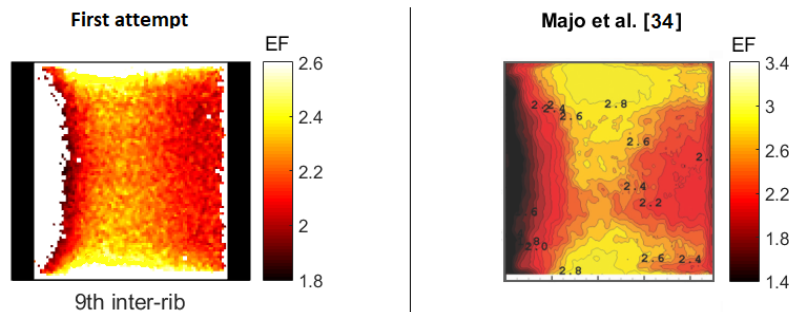


Figure 5.22: Enhancement factor distribution for the first attempt of the iterative data processing procedure compared with literature result (Majo et al. [34])

Moreover, Fig. 5.22 reports the comparison with the attempt EF distribution calculated to start the iterative procedure that elaborates the steady-state experimental data (described in Par. 4.3.3). Without focusing on the absolute values, it is possible to recognize a similar heat transfer behaviour in the two maps, indeed also the first attempt distribution presents the maximum heat transfer near the lateral walls. It is recalled that the first attempt values are calculated neglecting the heat losses that are due to conductive and radiative phenomena. Therefore the different distribution presented by Ref. [33] can be due to an inaccurate heat losses estimation. In the cited article, the heat transfer was indeed calculated by performing a simple energy balance on a surface element of the heating foil, in which the authors estimated the heat losses assuming one-dimensional conduction through the heated wall. In this way, lateral conduction is neglected, even though it has a large role near the sidewalls where the channel lateral walls behave like

heat sinks for the ribbed surface. Therefore the one-dimensional conduction assumption used by Ref. [33] is improper in lateral areas, but it is justifiable in the central region. Indeed, close to the channel centerline, the EF values reported by Ref. [33] are similar to the present ones. In view of all these, it is clear how heat losses estimation can significantly influence the obtained heat transfer results. Therefore, the choice of the proper physical model and relative assumptions are essential to avoid mendacious data which in turn can lead to misleading conclusions. This is the reason why it was chosen to set up the complex numerical models and the iterative procedure described in Par. 4.3.3.

One last comparison of the achieved data with the literature has been done by means of the spanwise averaged enhancement factor EF_{span} . The enhancement factor distributions of the static condition for the transient and steady-state tests are averaged in the z -direction within the 9th inter-rib. Figure 5.23 allows the comparison of the results with the data by Mayo et al. [35] and by Ekkad et al. [12]. The EF_{span} of Ref. [35] are available for test condition equal to $Re = 15000$, 30000 and from Ref. [12] are extracted at $Re = 12000$, 60000 after the 6th rib of the first section of a two-pass ribbed channel with $H/D_h = 0.125$ (present investigation $H/D_h = 1$). The measurements present similar trends and an agreement in the position of the maximum heat transfer, therefore that comparison could be considered a validation of the experimental results of the present investigation.

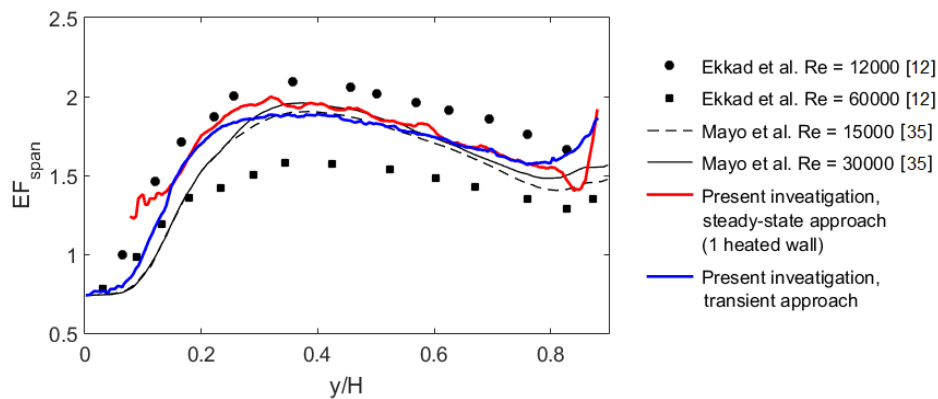


Figure 5.23: Comparison with literature of the spanwise averaged enhancement factor

Ekkad et al. [12] reported that heat transfer decreases with an increase in Reynolds number, while the EF_{span} profile at $Re = 30000$ is only slightly higher than the $Re = 15000$ ones in the result presented by Mayo et al. [35]. The insufficient coherence in the literature data has hence led to perform the steady-state thermography on the investigated channel in order to collect more reliable heat transfer data, which are used to validate the heat transfer distributions accomplished with the transient tests. From Fig. 5.23, it is already possible to appreciate the similar results in static condition that are obtained through the transient approach and the steady-state with one heated wall. However, the comparison between the two approaches has to be presented in more detail and for all the rotation conditions.

Figure 5.24 presents the heat transfer distributions about the 9th inter-rib for the various rotation conditions and for the different methodologies. In this regard, it should be noted that the highest rotation condition for the steady-state tests ($Ro = 0.18$) is compared with the closest transient rotation condition ($Ro = 0.20$). Furthermore, it has to keep in mind that the study can be accurately conducted in the central inter-rib areas for the steady-state tests, where the boundary condition assumptions used to process the experimental data have negligible effects. The comparison shows that in static condition the distributions are almost the same, whereas when the rotation number increases, the maps of the transient tests are closer to the distribution obtained with the steady-state method in which only the ribbed wall is heated.

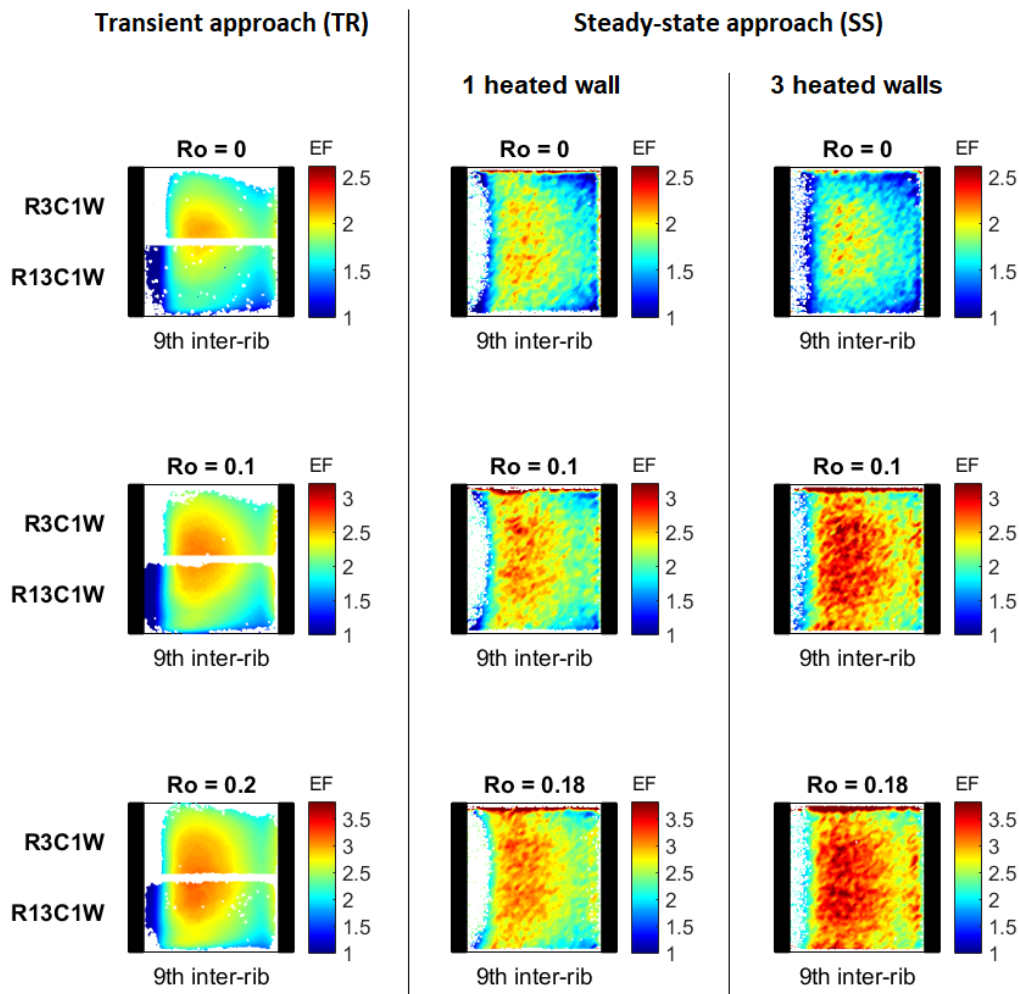


Figure 5.24: Enhancement factor maps obtained for the different thermography methods

These observations can be highlighted by the comparison between the EF profiles that are extracted along the channel length at $z = 20\text{ mm}$ and $z = 30\text{ mm}$ (Figures 5.25 and 5.26). The resulting profiles are shown for the inter-ribs that were investigated by both approaches (i.e., from 7th to 12th inter-rib).

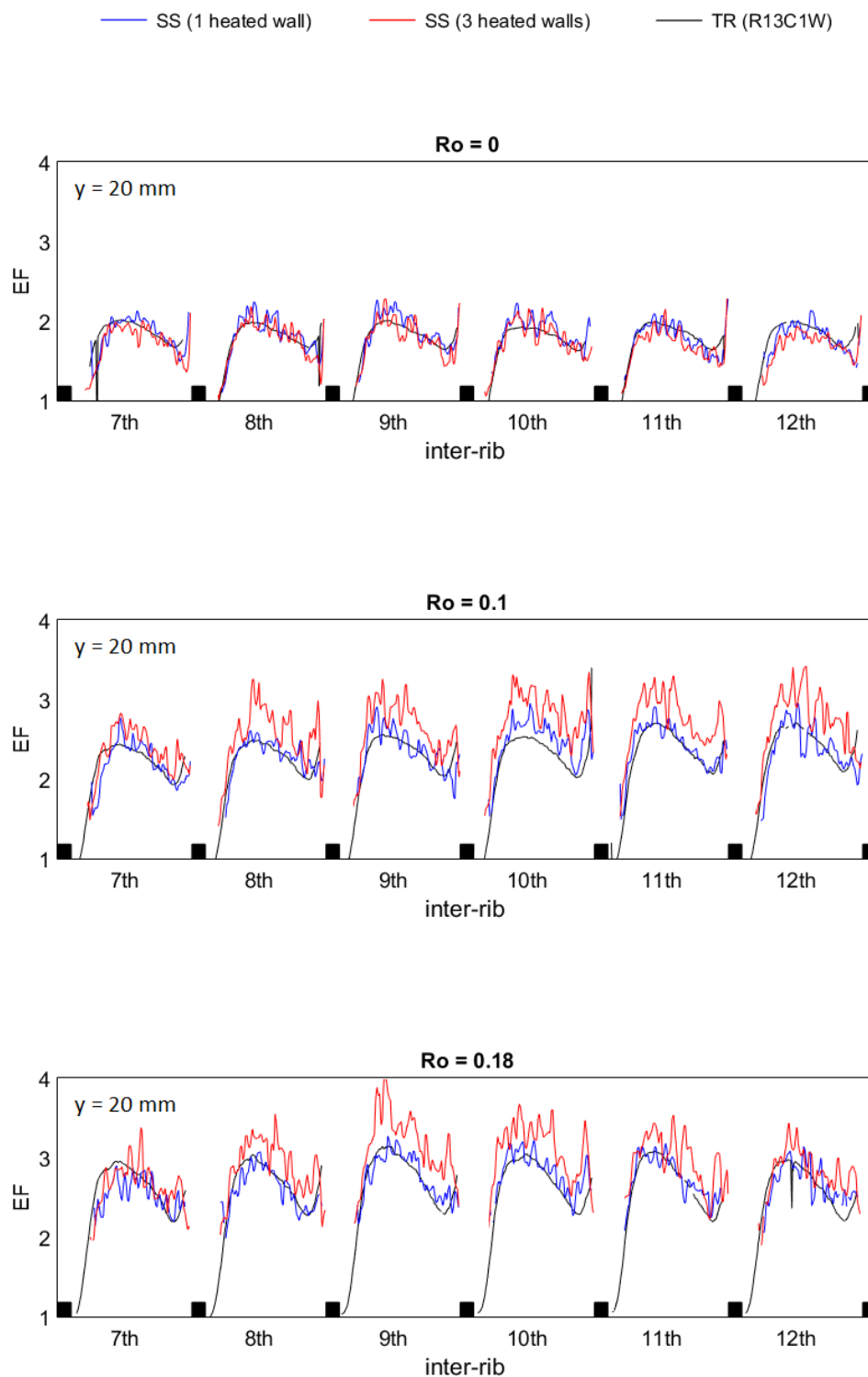


Figure 5.25: Enhancement factor profiles extracted at $z = 20 \text{ mm}$ for the different thermography methods

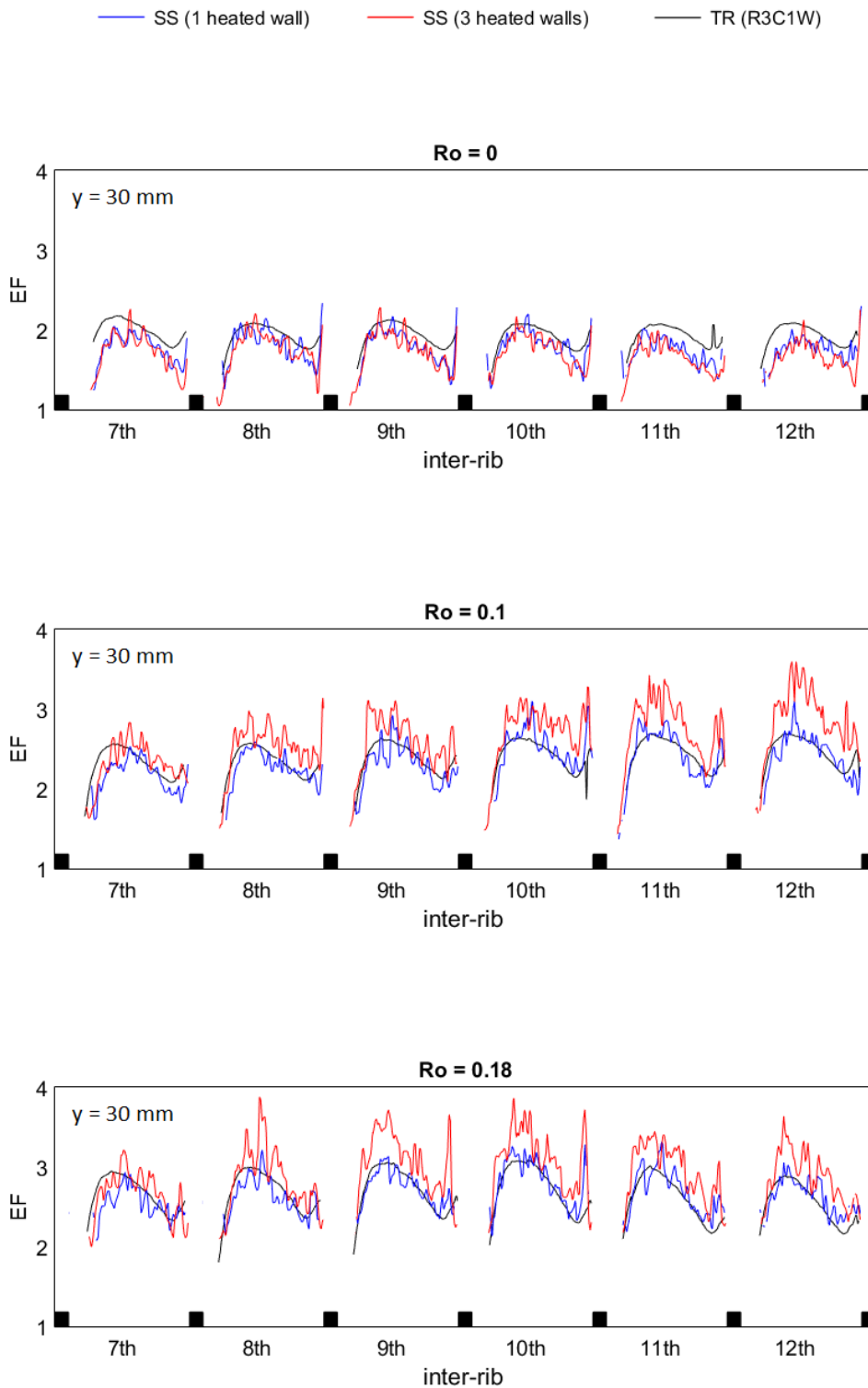


Figure 5.26: Enhancement factor profiles extracted at $z = 30 \text{ mm}$ for the different thermography methods

At each rotation condition, the transient EF profiles are closer to the steady-state test with only one side heated rather than to the steady-state tests in which are heated three sides, which shows higher EF_{avg} . Furthermore, this behaviour is confirmed by the comparison of the trends of the average enhancement factor, as reported in Fig. 5.27.

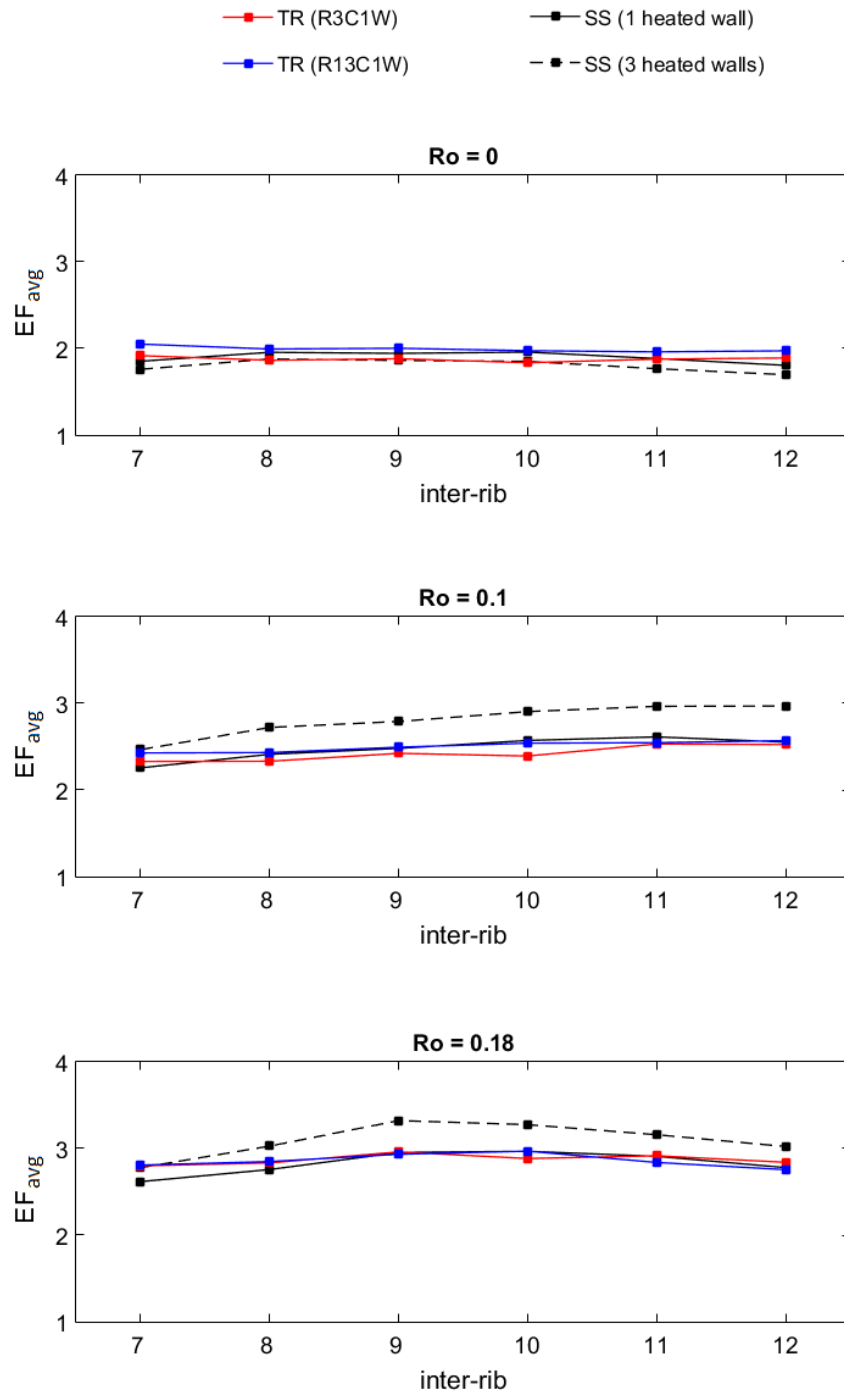


Figure 5.27: Average enhancement factor values along the channel length for the different thermography methods

Figure 5.28 reports the average enhancement factor at the 9th inter-rib as a function of the rotation number, for the different thermography methods and walls heating conditions. Once again, it is possible to assert that in static condition all the test approaches provide the same heat transfer information. When the rotation takes place the steady-state thermography with three heated walls provides heat transfer values that are higher than the values obtained from the same method in which only the ribbed side is heated. The transient results are pretty much similar to the latter steady-state walls heating condition data.

As stated, the difference between EF values within steady-state method can be ascribed to the different thermal conditions of the sidewalls that produce different buoyancy effects, which in turns generate secondary flow structures with different strengths. The same mechanism can be the potential cause for which EF values in the transient tests are similar to steady-state with only heated ribbed side heated, indeed in both of them the sidewalls aren't heated.

The setting up of a computational thermal-fluid model, which could be previously validated by the present experimental tests, could be useful to provide information about the flow field that develops inside the channel and hence to understand the different heat transfer indications provided by the two thermographs.

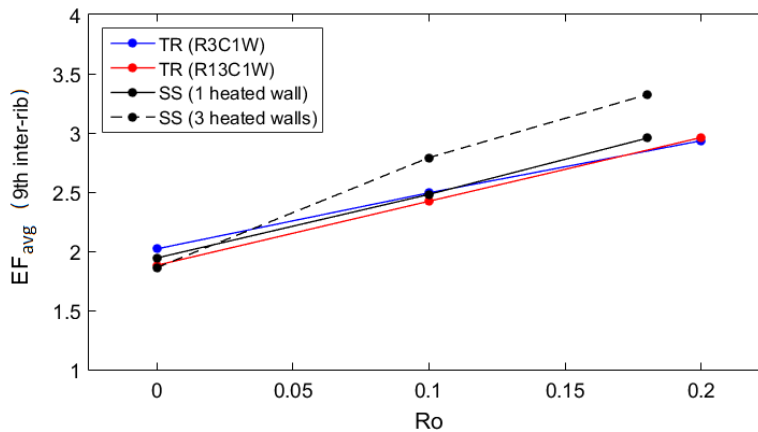


Figure 5.28: Average enhancement factor of the 9th inter-rib for the different thermography methods

According to the data obtained, the transient liquid crystals thermography can be considered validated by the liquid crystals thermography with only the ribbed side heated. Furthermore, the heating settings play a powerful role in the experimental results obtained employing the steady-state thermography. Indeed the thermal conditions of the channel inner surfaces significantly affect the flow field development, hence the heat transfer.

The thermography in both methods provides experimental data that can not be directly compared with the real blade cooling channel performances since the latter inner surfaces experience different thermal loads. Therefore, the experimental results can be properly used in the design phase or the computational fluid dynamics validation, only knowing under which thermal boundary conditions the measurements are accomplished.

Chapter 6

Conclusion

From an economic perspective coupled with even more awareness about the environmental aspect, there is a strong push to develop higher efficiency gas turbine engines. The best cycle performance can be accomplished by increasing the turbine inlet temperature, which requires a clever combination of different cooling techniques to thermally protect the engine components on the hot gas path. The internal forced convection is one of the most used techniques to preserve the structural integrity and to ensure a long lifespan of turbine blades of the early stages. Nowadays, the numerical simulation tools assist the cooling channels development and design, but the geometrical complexity and working conditions continue to make essential their experimental investigation. The liquid crystal thermography (LCT) in transient approach is a suitable method to obtain heat transfer measurements inside engine representative cooling channels. This experimental methodology allows achieving high spatial resolution distributions of the heat transfer coefficient inside very complex geometries and it requires shorter testing time than other and comparable techniques.

For these reasons, a rotating channel test facility was designed and used for research purposes in the Turbomachinery and Energy Systems Laboratory of the University of Udine. Firstly, the rig was developed only for aerodynamic measurements and only in the recent past was improved to allow performing also heat transfer measurement with a non-conventional transient LCT approach. The present contribution was mainly aimed to verify the measurement chain reliability and to finally validate the transient technique as in use in the rig.

The validation of the test facility and the LCT methodology was performed on rotating square cross-section channel with ribs on one side. The channel is a single passage with the flow moving radially outwards. Despite the simple geometry chosen, it was soon clear that in the open literature there are not reliable and consistent heat transfer results on both static and rotating conditions that could be profitably used for validation purposes. Therefore, in the frame of this project, it was decided to perform also heat transfer measurements by means of the well-established LCT in steady-state approach, in order to obtain reliable data to be cross-compared with those from the transient approach. Both thermography approaches were used to investigate the heat transfer on the channel

ribbed surface that acts as trailing edge. The different experimental methodologies have required different test facility setups with the design and realization of two channel models, identical in terms of internal geometry but with different technical requirements. A large effort was also made to improve the test facility to reach higher rotation numbers (up to $Ro = 0.3$ at $Re = 20000$, for the present study case) ensuring greater structural stability. Besides, several upgrades were made to the vision system used for the LCT, which now can deal with four cameras and has a higher storage speed. The two different channel models were easily installed on the test facility thanks to its versatile design.

The transient LCT was performed making use of two types of narrow-banded liquid crystals (namely, R3C1W and R13C1W). For the selected activation temperatures, those liquid crystals stay for most of the time in the melted phase and, most important, above their higher clearing point. Consequently, also supported by the literature (although almost absent for this kind of liquid crystals), some doubts aroused about the stability in time of their temperature/colour response and about the best approach for their calibration. For these reasons, a new calibration facility was designed and implemented, which allows evaluating the calibration temperature during a temperature evolution phase, i.e. by reproducing the temperature evolution that the liquid crystals undergo during a transient test. The results show that the liquid crystals have a different colour response depending on which direction the calibration is obtained: the calibration values on cooling (from room temperature down below the activation point) are lower by about $0.1^{\circ}C$ than on heating (from temperatures below the activation one up to room temperature values) for both type of liquid crystals. Calibration tests were repeated also by means of the calibration facility already in use in the laboratory, in which the liquid crystals undergo a time-stable temperature gradient over space. In this condition, the delivered calibration temperatures were found to fall in between the cooling and heating values obtained with the new approach. This evidence was obtained for both the liquid crystals here used and in multiple repeated tests. The conclusion of this survey about calibration is therefore that calibration of liquid crystals for transient experiments has to be taken also in transient and with the same direction of the temperature gradient (cooling or heating). Unfortunately, due to some technical limitation on the new calibration apparatus, it was not possible to investigate also about the effects of the velocity of the temperature evolution, leaving this answer open for future research activity.

Transient LCT tests were performed up to a rotation number equal to 0.3 and simultaneously with the two types of liquid crystals sprayed on the two halves of the ribbed surface (the separation is determined by the channel midline). The reason for this choice is to have a first indication of the measurement reliability. Indeed, being the activation temperatures very different, the indication useful for the computation of the heat transfer coefficient were made available at much different testing times and airflow temperature evolutions. In all rotating conditions, the comparison of the resulting heat transfer coefficient distributions turned out to be very satisfactory, reporting a maximum difference of about 6% in limited

regions of the investigated domain. This represents a first evidence of the consistency of the methodological approach. It has to be pointed out that this kind of check was already attempted on the facility at the early stage of its development, but the results have never been so good as in this case. The reason has to be ascribed to the new calibration approach here developed.

About uncertainty estimation, the standard and well-established Kline & Mc Clintock approach was applied to the transient liquid crystal methodology. The sensitivity coefficients can not be straight forward evaluated because of the analytic form of the equation used to evaluate the heat transfer coefficient. Therefore, it was dealing with the problem by performing a sensitivity analysis. This was done by firstly identify the experimental parameters which values might be affected by different error sources (i.e., uncertainty regarding the channel material properties, the calibration temperature, the fluid temperature and activation time determination of the liquid crystals). Then, the impact on the results by a variation of each parameter was assessed. The study results have revealed that the error sources mainly affect the measured values according to the liquid crystal type and the fluid temperature evolution. Consequently, a careful choice of the temperature step and of the liquid crystal activation value, tailored on the expected heat transfer levels, can help to limit the experimental uncertainty. In the present investigation for all the rotating condition and in the maximum heat transfer zone, the experimental uncertainty has been estimated 3.1% and 6.2% for the R3C1W and R13C1W liquid crystal, respectively.

The experimental channel setup used to perform the steady-state LCT has allowed to evaluate the heat transfer coefficient under two uneven walls heating conditions of the inner channel surfaces. The first is the common investigation way, in which only the surface of interest (i.e. the ribbed wall) is heated; in the other one, a uniform heat flux is applied also on the lateral walls. The maximum rotating condition was fixed at a rotation number of about 0.18 because of the technical limitation of the test facility.

The R35C7W wide-banded liquid crystal was chosen as the temperature indicator over all the ribbed surface. The hue-temperature function was determined by means of the calibration facility with the temperature gradient approach. The consistency of the temperature information pretty depends on lighting condition and viewing angle, therefore the two vision systems use for calibration and measurement were set up as much similar as possible. Colour perceptions between the calibration and test vision systems were verified thanks to an appropriate colour camera calibration procedure.

In order to accomplish faithful heat transfer data from the steady-state LCT, particular attention was dedicated to the procedure for the heat losses evaluation. This has led to set up a complex iterative numerical procedure to elaborate the collected experimental data and that can also deal with different walls heating conditions. An iterative procedure makes use of two numerical models, implemented by means of commercial software, in order to take into account both conductive and radiative phenomena. A correction step adjusts the attempted heat transfer coefficient values on the ribbed surface at each iteration, until the

numerical temperature distribution on the ribbed wall matches with the experimental temperature values obtained from the steady-state LCT.

Several strong assumptions were made in order to impose the unknown values set as boundary conditions in the conductive numerical model (e.g. the heat transfer coefficient on the smooth sides or in the blank areas where the liquid crystal was not activated). Although the values of this unknown were grounded on physical considerations or available literature data, a sensitivity analysis was performed to evaluate the impact on the resulting heat transfer values. The investigation has shown that it is possible to identify a wide inter-rib central region in which the heat transfer distribution has variation less than 1%, even if the boundary condition values were drastically changed $\pm 50\%$ of the reference value.

The whole data set (steady or transient LCT, stationary or rotating channel) was analysed in terms of enhancement factor and by looking at two-dimensional distribution maps, profiles extracted along the channel length, and area-averaged data over the inter-ribs domains. The data quality and resolution are such that it was possible to recognize the well known rotational effects but the focus was put on the cross-comparison between steady and transient approach. For all rotation conditions, the transient approach delivered results that are in very good agreement with those from the steady approach and obtained in the condition where the ribbed wall is the only heated surface. The results match satisfactorily not only if global values are compared (area-averaged data) but also if local effects are observed. This confirms both the reliability of the transient LCT methodology and the need for an accurate estimation of the heat losses for the steady-state LCT approach. Indeed, the comparison with the available literature in a very similar geometry where steady-state LCT was applied, fails in the regions close to the lateral walls, coherently with the simplified heat losses model that neglects lateral conduction and that was used to obtain the data in literature.

Steady-state LCT measurements were performed also by heating the ribbed surface and the two lateral walls with uniform heat flux, this in order to investigate the effects of heating boundary conditions. Data comparison revealed that wall heat transfer distribution does not change for the non-rotating channel if the heating condition is varied. Conversely, significantly higher enhancement values were observed under rotation for the case where the three walls supply heat to the flow, in agreement with the few contributions available in the literature. This behaviour suggests that the responsible for heat transfer augmentation can be probably the different buoyancy effect induced by different thermal boundary conditions. However, a lot of effort has still to be made in the understanding of the complex phenomena laying behind, and only advanced computational tools can provide the answers. This work aims also to provide a contribution in this direction with detailed and reliable heat transfer data useful for validation.

In conclusion, the aim of the present work has been reached. The experimental transient LCT methodology and test facility have been further developed and finally validated. The results also open the way to new aspects of internal cooling that could be the subject of new research projects.

Appendix A

Thermal properties

A.1 Air

The air thermodynamic properties at a constant pressure of 1 bar from M. Fossa [14] are reported in Tab. A.1.

Table A.1: Thermodynamic properties of air at pressure of 1 bar

| T [°C] | k [W/mK] | μ [$\mu\text{Pa s}$] | Pr [-] |
|-------------|---------------|-------------------------------|-------------|
| -100 | 0.01602 | 11.77 | 0.7423 |
| -80 | 0.01774 | 12.94 | 0.7357 |
| -60 | 0.01941 | 14.07 | 0.7301 |
| -40 | 0.02104 | 15.16 | 0.7258 |
| -30 | 0.02184 | 15.70 | 0.7236 |
| -20 | 0.02263 | 16.22 | 0.7215 |
| -10 | 0.02341 | 16.74 | 0.7196 |
| 0 | 0.02418 | 17.24 | 0.7179 |
| 10 | 0.02494 | 17.74 | 0.7163 |
| 20 | 0.02569 | 18.24 | 0.7148 |
| 30 | 0.02643 | 18.72 | 0.7134 |
| 40 | 0.02716 | 19.20 | 0.7122 |
| 60 | 0.02860 | 20.14 | 0.7100 |

In order to have the air thermodynamic properties easily available at every temperature, the data in Tab. A.1 are interpolated by second-order functions:

- Thermal conductivity:

$$k = -4.9983 \times 10^{-8} T^2 + 7.6560 \times 10^{-5} T + 2.4181 \times 10^{-2} \quad (\text{A.1})$$

- Dynamic viscosity:

$$\mu = -4.1416 \times 10^{-5} T^2 + 5.0553 \times 10^{-2} T + 17.247 \quad (\text{A.2})$$

- Prandtl number:

$$Pr = 7.1525 \times 10^{-7} T^2 - 1.6967 \times 10^{-4} T + 7.1781 \times 10^{-1} \quad (\text{A.3})$$

Figure A.1 provides a comparison between the interpolated function and the available data of the air thermodynamic properties.

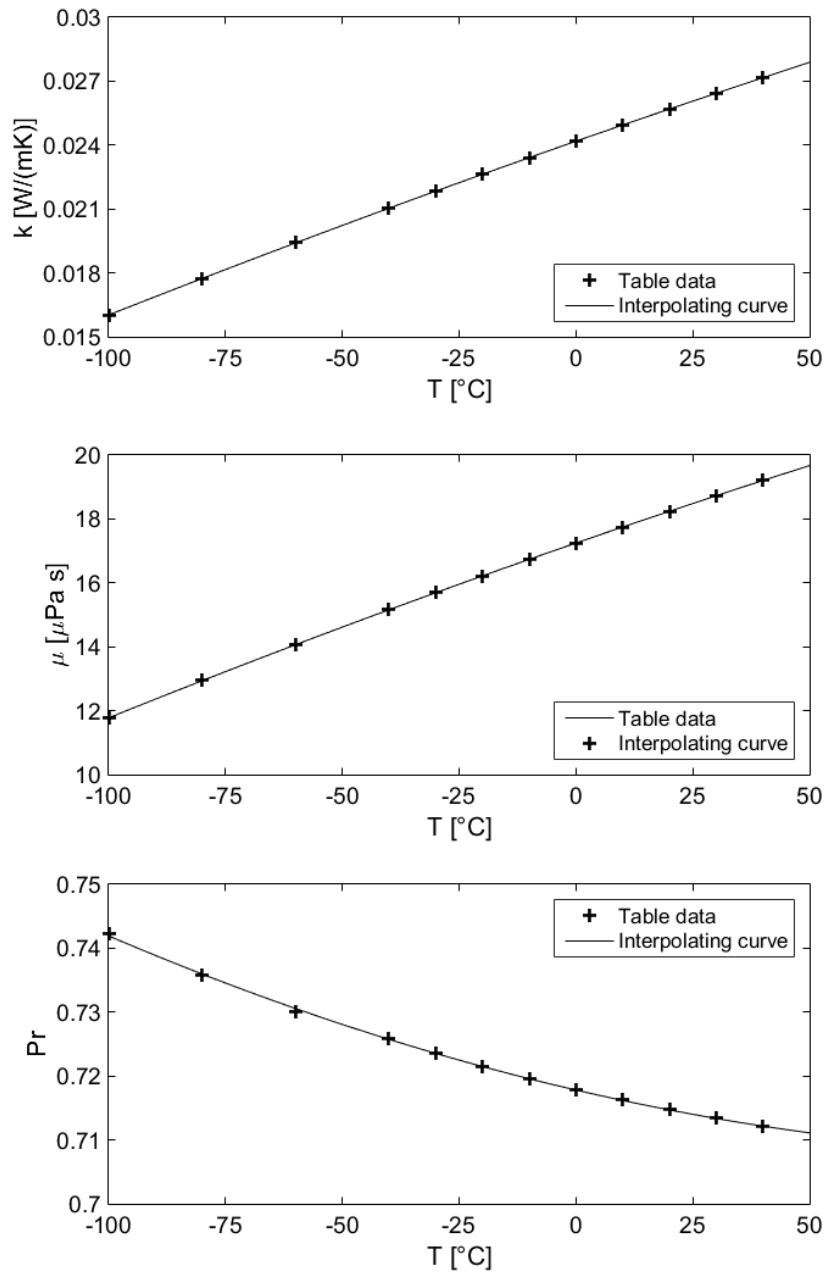


Figure A.1: Diagrams of air thermodynamic properties at pressure of 1 bar

A.2 Inconel alloy 600

The declared electrical resistivity of Inconel alloy 600 [21] is plotted as function of the temperature in Fig. A.2.

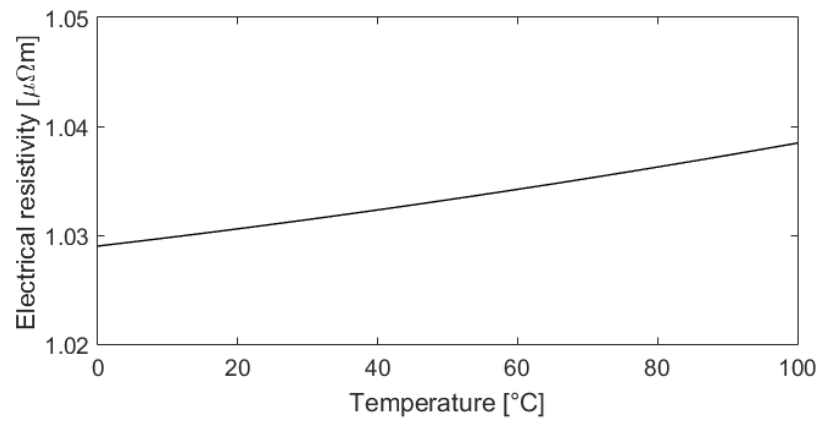


Figure A.2: Diagrams of electrical resistivity of Inconel alloy 600

Appendix B

Uncertainty and sensitivity analysis

B.1 Transient test data elaboration

In the present thesis, heat transfer coefficients are calculated from Eq. 2.18 that is the solution of the Fourier's 1D equation relative to a general fluid temperature evolution. However, Eq. B.1 describe the wall temperature T_w evolution consequent to an ideal step change of the fluid temperature from T_0 to T_f , in order to highlight the error sources.

$$T_w = T_0 + \left[1 - \exp\left(\frac{h^2 t}{(\rho k c)_{mat}}\right) \operatorname{erfc}\left(h \sqrt{\frac{t}{(\rho k c)_{mat}}}\right) \right] (T_f - T_0) \quad (\text{B.1})$$

It is possible to identify four experimental error sources:

- *Wall temperature* (T_w). The uncertainty of the liquid crystals calibration facilities affects the surface temperature value.
- *Fluid temperature* (T_f). The fluid temperatures values are detected by thermocouples immerse in the airflow, which are affected by measurement uncertainty.
- *Activation time* (t). The camera frame rate, the configuration of the vision systems, and the peak find algorithm contribute to the precision with which the maximum green intensity location is determined (it is the only instant at which is possible to know the surface temperature).
- *Material properties* ($\rho k c$). The surface temperature time-response obviously depends on the thermo-physical properties of the material of which the walls are made.

The summary of the uncertainty values addressed to the error sources are reported in Tab. B.1.

Table B.1: Uncertainties in error sources

| Error source | Value |
|--------------------------------|-------------------|
| T_w Wall temperature | $\pm 0.1^\circ C$ |
| T_b Fluid Temperature | $\pm 0.2^\circ C$ |
| t Activation time | $\pm 0.5 s$ |
| ρck Material propierties | $\pm 5\%$ |

The contribution of each error source δs_i in the final uncertainty δh of heat transfer coefficient is estimated by using the Kline & McClintock method [27]:

$$\delta h = \sqrt{\sum_{i=1}^M \left(\frac{\partial h}{\partial s_i} \delta s_i \right)^2} \quad (\text{B.2})$$

An analytic expression that isolate the heat transfer coefficient variable from Eq. B.1 does not exist, therefore it is impossible to straight forward evaluate the partial derivative terms of Eq. B.2, which are also known as sensitivity coefficients. To overcome this issue, this paragraph aims to separately quantify the relative importance of the parameters (i.e., material properties, wall temperature, fluid temperature and activation time) on the evaluation of the heat transfer coefficient value through a sensitivity analysis, and hence evaluate the magnitudes of the sensitivity coefficients. The sensitivity analysis is carried out for tests characterized by different rotation numbers $Ro = 0; 0.1; 0.2; 0.3$ (test number 1, 3, 5, 7 of Tab. 5.6) at two points on the ribbed wall, which are located close to the fluid reattachment zone of the 9th inter-rib: one point at $(y, z) = (625, 30) mm$ (R3C1W liquid crystal area) and the other at $(y, z) = (625, 20) mm$ (R13C1W liquid crystal area). Figure B.1 and B.2 show the trends of the percentage differences of the enhancement factor PD , calculated with respect to the reference case EF_{ref} in which no parameters have changed values:

$$PD_{EF} = \frac{EF - EF_{ref}}{EF_{ref}} \quad (\text{B.3})$$

It is possible to notice that a variation of the 10% of material properties affect the EF by about 5%, regardless the rotation conditions (hence the heat transfer coefficients values) and the types of the liquid crystals that are employed. That justifies the choice to send two samples of the channel wall to a specialized laboratory in order to obtain an accurate measurement of the thermal-physical properties (Par. 3.1.1). The R3C1W liquid crystal has a lower activation temperature than the other liquid crystal, and consequently, it reaches the green intensity peak after the R13C1W liquid crystal. For that reason, the R13C1W suffer more than the R3C1W from the error sources, indeed the PD trends of R13C1W have higher slope than R3C1W ones. It is possible to assert that the magnitude of the EF variation, relative to T_w and t uncertainties, significantly depends also from the fluid temperature evolution until the liquid crystal activation is reached.

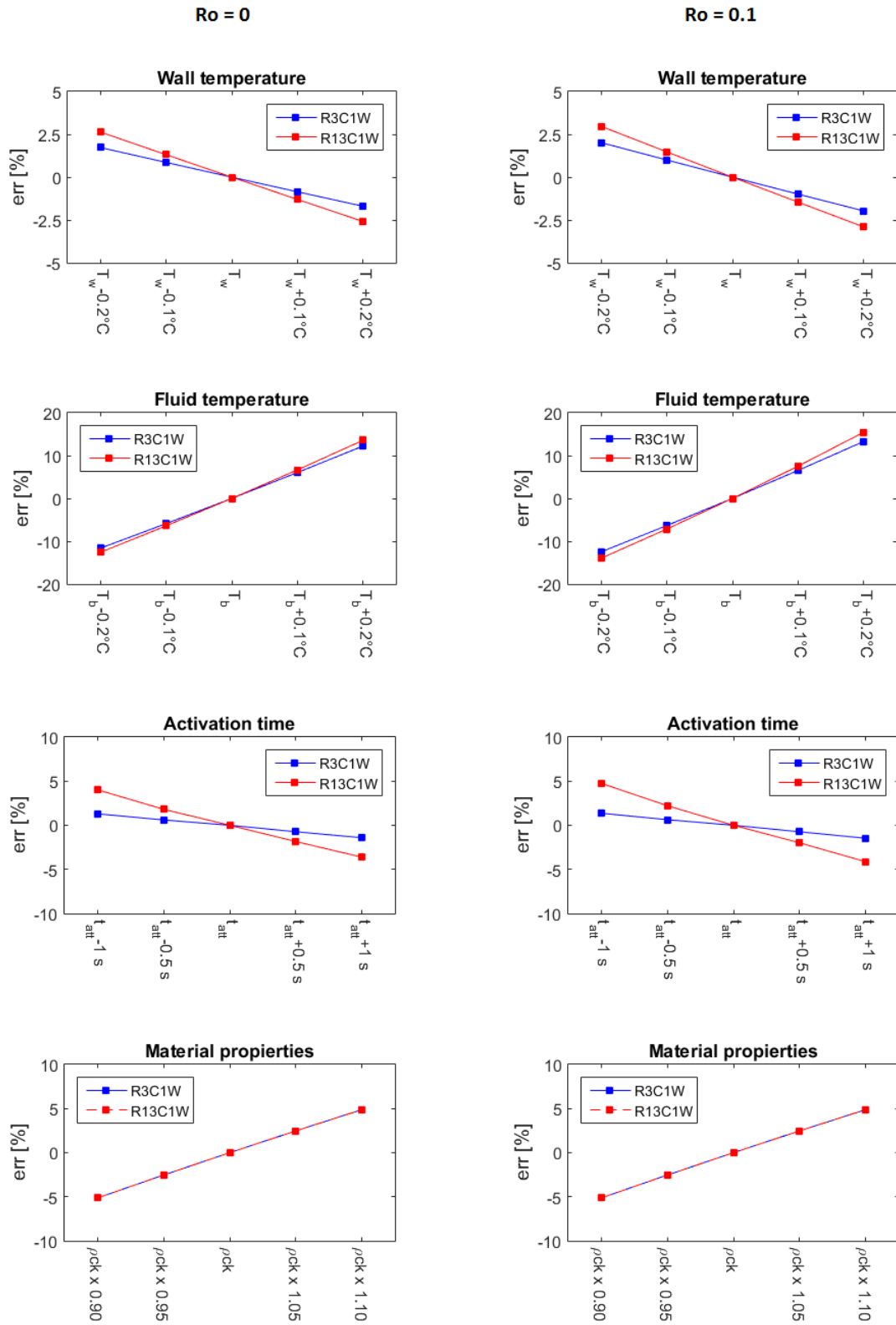


Figure B.1: Effects of main error sources on the heat transfer values in transient approach tests ($Ro = 0, 0.1$)

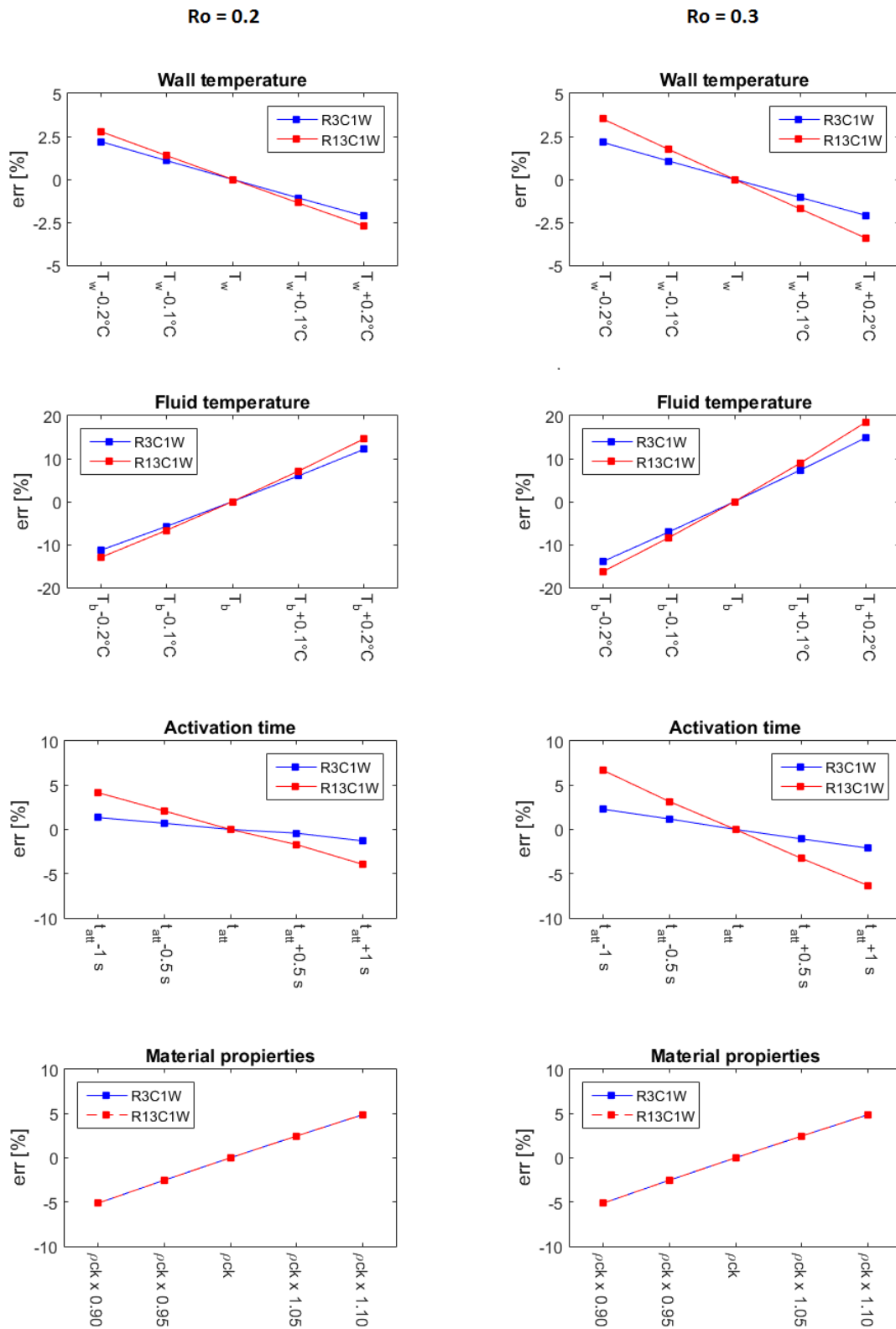


Figure B.2: Effects of main error sources on the heat transfer values in transient approach tests ($Ro = 0.2, 0.3$)

Table B.2: Uncertainty estimation for the transient tests

| Test number | Ro | Liquid Crystal | |
|-------------|-----|----------------|--------|
| | | R3C1W | R13C1W |
| 1 | 0 | 2.9% | 4.3% |
| 3 | 0.1 | 3.0% | 5.1% |
| 5 | 0.2 | 2.9% | 4.4% |
| 7 | 0.3 | 3.1% | 6.2% |

The resulting relative errors of the heat transfer coefficient are reported in Tab. B.2. As expected, the R3C1W liquid crystal has a greater accuracy than the R13C1W one for all the tests. Indeed the dimensionless wall temperatures associated to the R3C1W liquid crystal are more centered in the suggested range to minimize the uncertainties [38] (see Fig. 5.6).

Anyway for all the rotation conditions, the the percentage differences are lower than 3.1% and 6.2% for the R3C1W and R13C1W liquid crystals, respectively.

B.2 Steady-state test data elaboration

This paragraph aims to study the effects on the heat transfer distribution of the boundary conditions set to the FEM conduction model used in the iterative procedure that is used to elaborate the steady-state approach data(Par. 4.3.3). For this purpose, each boundary condition is investigated separately (Tab. B.3 gives an overview of all the cases considered):

- *Raditive heat fluxes* (q_{rad}). The heat transfer coefficient is evaluated using also the FEM radiative model coupled with the conductive one (case A1) or neglecting the radiative heat fluxes (case A2).
- *Outer surfaces temperature* (T_{ext}). The iterative procedure is run increasing by $5^{\circ}C$ the T_{ext} (case B1) or decreasing by the same amount the T_{ext} (case B2), in order to consider the surface temperature unevenness and the possible error in the measurement of the surface temperature.
- *Heat transfer coefficient* (h_{rib} , h_{blank} , and h_{smooth}). Constant heat transfer coefficient values are assumed: on the rib areas to simulate the presence of the turbulator elements, on the blank areas of the ribbed wall where the liquid crystals haven't provided information about the wall temperature, and on the smooth sides of the channel. These strong assumptions are tested by changing the heat transfer coefficient from the 150% (cases C1, D1, E1) to 50% (cases C2, D2, E2) of their starting values.

All the investigation are carried out for the static test in which only the ribbed wall is heated. The enhancement factor EF and the percentage difference PD_{EF} are used to present the results of the sensitivity analysis at the 9-th inter-rib.

Table B.3: Boundary condition values considered for the sensitivity analysis

| Boundary condition | case 1 | case 2 |
|--|-------------------------|-------------------------|
| A) Radiative heat fluxes | ON (ref.) | OFF |
| B) Outer surfaces temperature | $T_{ext} + 5^\circ C$ | $T_{ext} - 5^\circ C$ |
| C) Heat transfer coefficient on rib areas | $1.5 \times h_{rib}$ | $0.5 \times h_{rib}$ |
| D) Heat transfer coefficient on blank areas | $1.5 \times h_{blank}$ | $0.5 \times h_{blank}$ |
| E) Heat transfer coefficient on smooth sides | $1.5 \times h_{smooth}$ | $0.5 \times h_{smooth}$ |

The percentage difference PD_{EF} is define as:

$$PD_{EF} = \frac{EF_{case} - EF_{ref}}{EF_{ref}} \quad (B.4)$$

The reference distribution EF_{ref} is that with the boundary condition described in Par. 4.3.3 and with the radiative model enabled (case A1 in Tab. B.3)

The EF values considering the radiation model disabled (case A2) are more than 10% greater than the case A1 in which the radiative fluxes are estimated, as proved by Fig. B.3. When the radiative phenomenon is considered, it removes heat from the ribbed side (the ribbed channel wall has an average temperature greater than the other three walls), and consequently, the convective heat transfer will be lower. Therefore it is essential to predict the radiative heat fluxes since they significative affect the values of the heat.

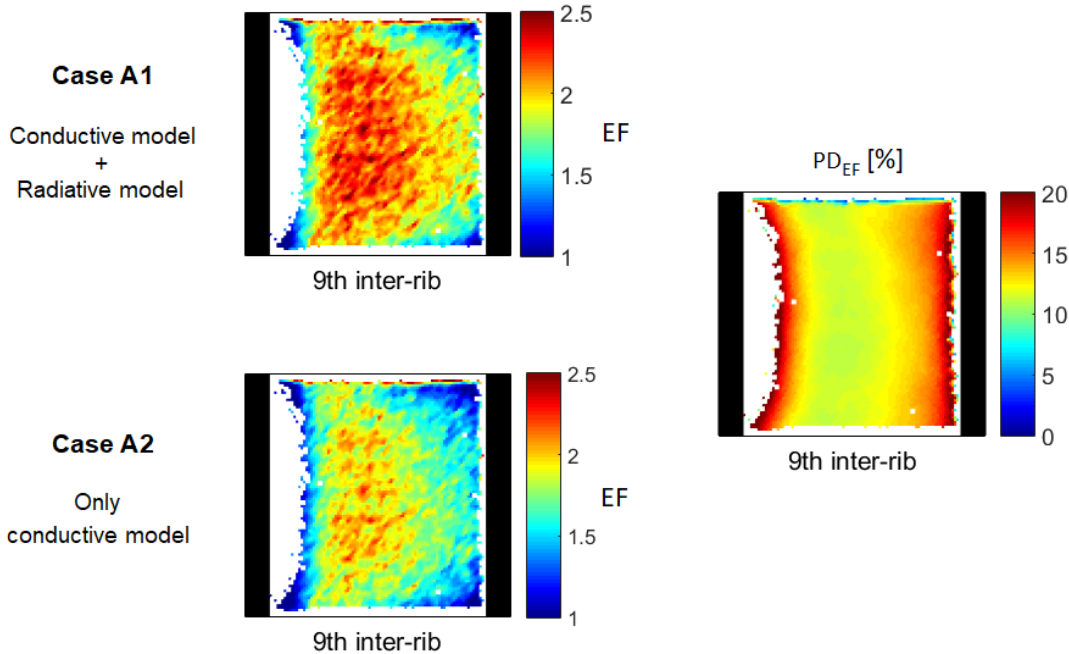


Figure B.3: Effect of the boundary conditions on the heat transfer distribution: radiative heat fluxes

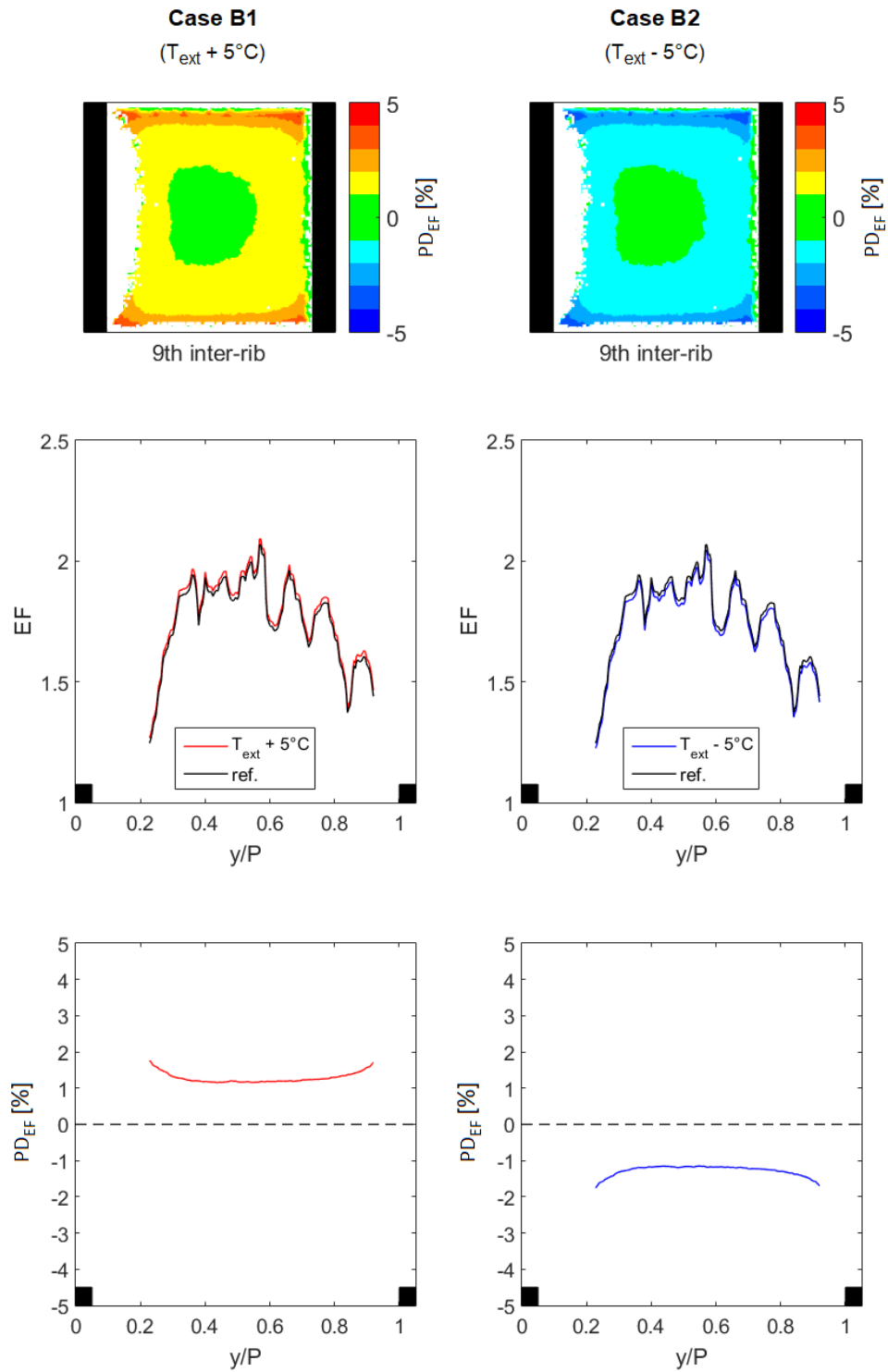


Figure B.4: Effect of the boundary conditions on the heat transfer distribution: outer surfaces temperature

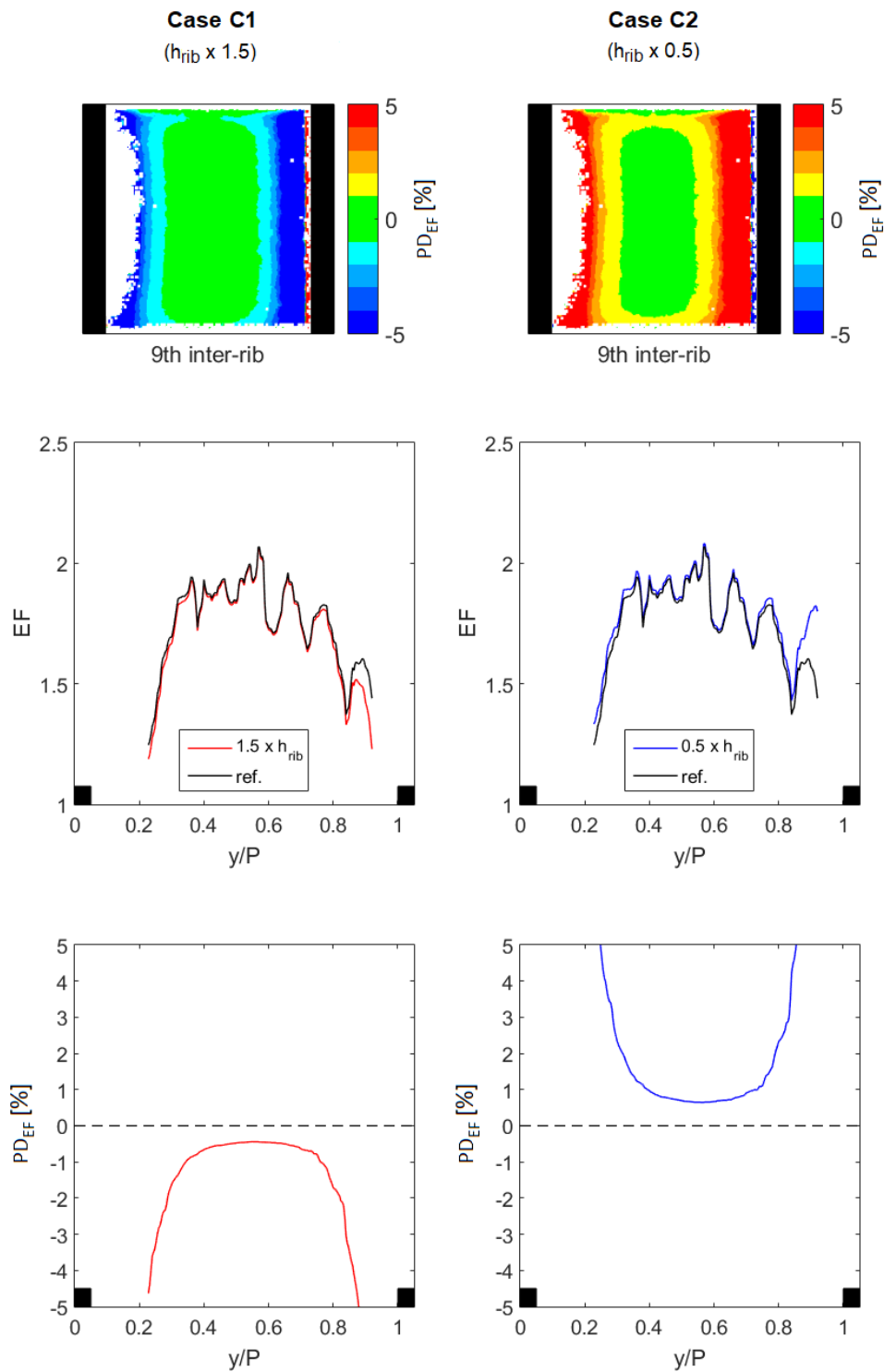


Figure B.5: Effect of the boundary conditions on the heat transfer distribution: heat transfer coefficient on rib areas

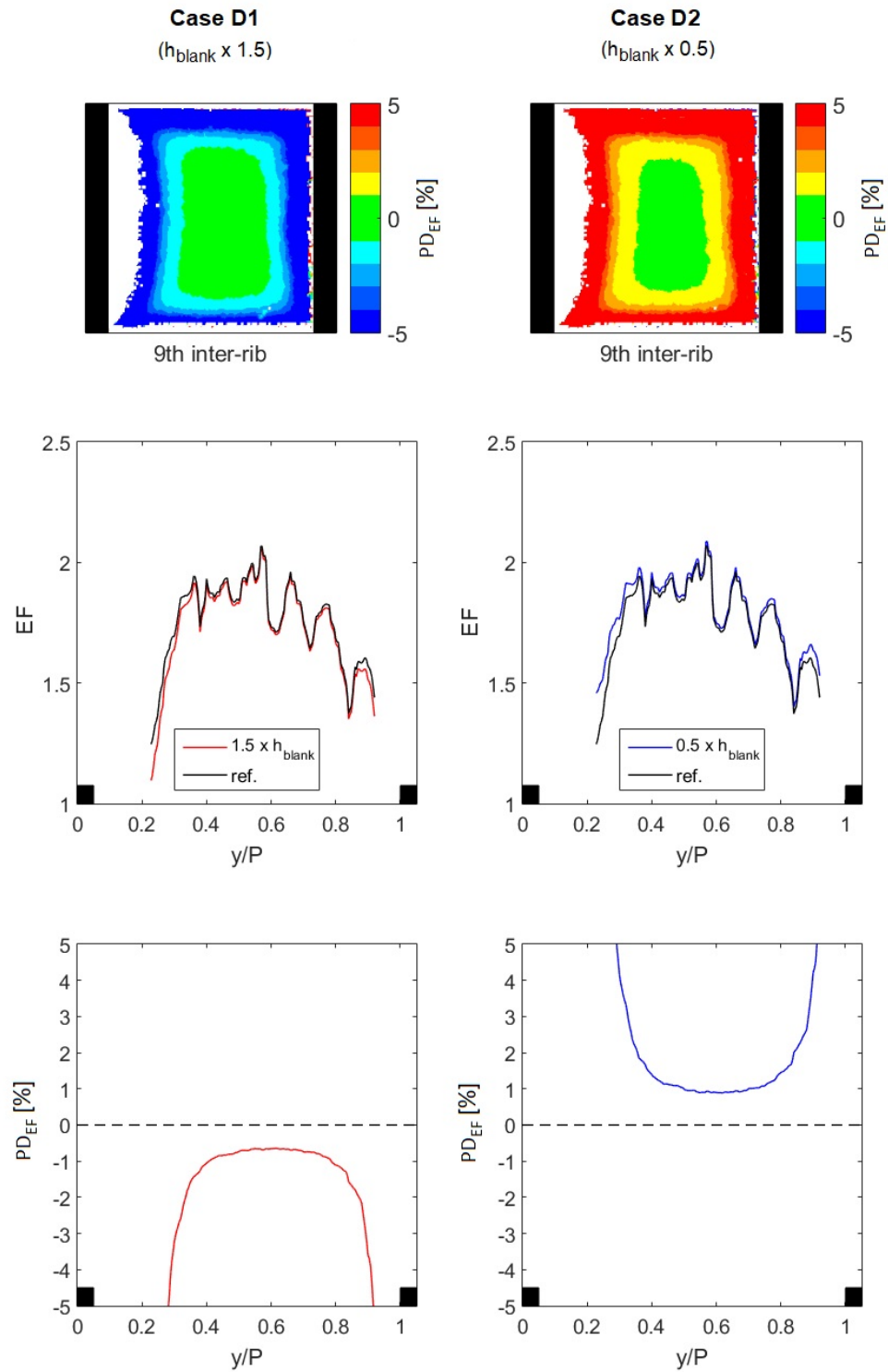


Figure B.6: Effect of the boundary conditions on the heat transfer distribution: heat transfer coefficient on blank areas

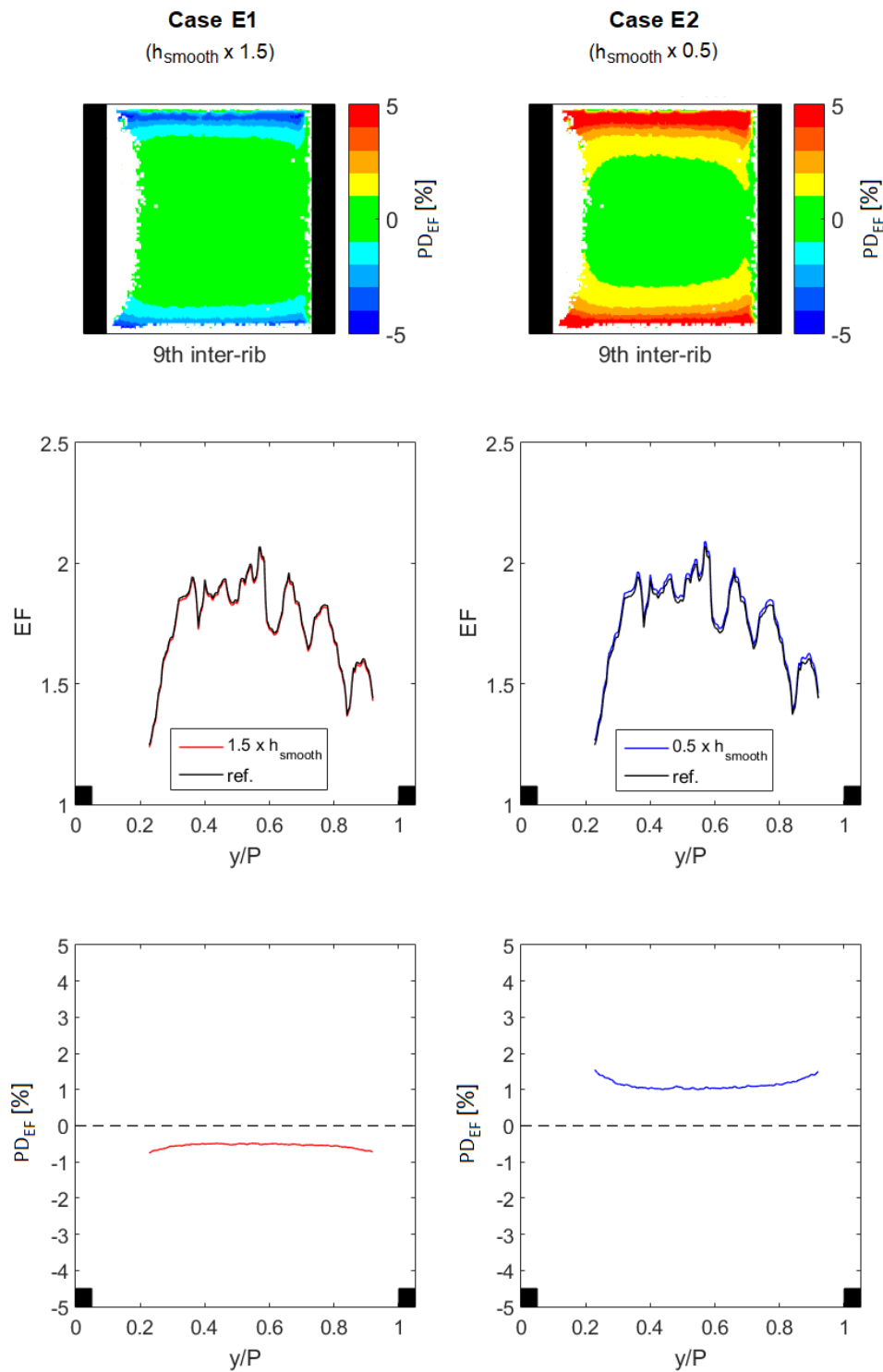


Figure B.7: Effect of the boundary conditions on the heat transfer distribution: heat transfer coefficient on smooth sides

The results of the investigation about the other boundary conditions are presented in Figures B.4, B.5, B.6, B.7, in which the percentage difference maps and the EF profile along the midline are showed. Relevant variations of the heat transfer distribution are obtained only with large outer temperature shifts (i.e., $\pm 5^\circ C$). Concerning the other boundary conditions, it can be seen how the heat transfer distribution is especially affected in the areas next to those in which constant values of heat transfer coefficient values are imposed. In any case, a large central region of the inter-rib is not significantly affected by the boundary conditions, although they have been drastically changed (i.e., increasing and decreasing the values of the heat transfer coefficients by 50%). This region can be individuated by the areas in which heat transfer distribution has variations less than 1% (green areas of the maps in Figures B.5, B.6, B.7).

In summary, it is possible to assert that the iterative procedure provides consistent information in a wide central inter-rib region despite the strong assumptions taken, allowing to obtain high detailed heat transfer distributions.

Bibliography

- [1] N. Abdullah, A.R.A. Talib, H.R.M. Saiah, A.A. Jaafar, M.A.M. Salleh (2011) – *Film thickness effects on calibrations of a narrowband thermochromic liquid crystal* – Experimental Thermal and Fluid Science, vol. 33, pp. 561-578
- [2] M.R. Anderson, J.W. Baughn (2004) – *Hysteresis in liquid crystal thermography* – Journal of Heat Transfer, vol. 126, pp. 339-346
- [3] A. Armellini, C. Mucignat, L. Casarsa, P. Giannattasio (2011) – *Flow field investigations in rotating facilities by means of stationary PIV system* – Measurement Science and Technology, vol. 23, No. 2
- [4] A. Armellini, L. Casarsa, C. Mucignat (2011) – *Flow field analysis inside a gas turbine trailing edge cooling channel under static and rotating conditions* – International Journal of Heat and Fluid Flow, vol. 32, pp. 1147-1159
- [5] M.P. Boyce (2002) – *Gas Turbine Engineering Handbook* – Gulf Professional Publishing, 2nd edition, p. 10
- [6] M. Çakan (2000) – *Aero-thermal investigation of fixed rib-roughened internal cooling passages* – Doctoral thesis, von Karman Institute for Fluid Dynamics
- [7] L. Casarsa, T.Arts (2005) – *Experimental investigation of the aerothermal performance of a high blockage rib-roughened cooling channel* – Journal of Turbomachinery, vol. 127, pp. 580-588
- [8] R.J. Clifford, T.V. Jones, S.D. Dunne (1983) – *Techniques for obtaining detailed heat transfer coefficient measurements within gas turbine blade and vane cooling passage* – American Society of Mechanical Engineers, 28th International Gas Turbine Conference and Exhibit, Paper No. 83-GT-58
- [9] F. Coletti, D. Lo Jacono, I. Cresci, T. Arts (2014) – *Turbulent flow in rib-roughened channel under the effect of Coriolis and rotational buoyancy forces* – Physics of Fluid, vol. 26
- [10] G. Comini, G. Cortella (2008) – *Fondamenti di trasmissione del calore* – Servizi Grafici Editoriali Padova, pp. 115-129
- [11] P.W. Dittus, M.K. Bolter (1930) – *Heat transfer in automobile radiator of the tubular type* – University of California Pub. Eng., vol. 2, No. 13

- [12] S. Ekkad, J.C. Han (1997) – *Detailed heat transfer distribution in a two-pass square channel with rib turbulators* – International Journal of Heat Mass Transfer, vol. 40, pp. 2525-2537
- [13] D.J. Farina, J.M. Hacker, R.J. Moffat, J.K. Eaton (1994) – *Illuminant invariant calibration of thermochromic liquid crystals* – Experimental Thermal and Fluid Science, vol. 9, pp. 1-12
- [14] M. Fossa (2012) – *Diagrammi e tabelle per i corsi di fisica tecnica* – Mechanical Engineering Department, University of Genoa
- [15] L. Furlani, A. Armellini, L. Casarsa (2015) – *Buoyancy effects at high rotation number on the flow field inside a triangular shaped rib roughened channel* – 11th European Conference on Turbomachinery Fluid dynamics and Thermodynamics
- [16] L. Furlani, A. Armellini, L. Casarsa (2015) – *Aerodynamic behaviour under rotation of an advanced leading edge impingement cooling channel* – 12th International Symposium on Experimental Computational Aerothermodynamics of Internal Flows
- [17] Grand view research (2018) – *Gas Turbine market size, share and trends analysis report by capacity (≤ 200 MW, > 200 MW), by technology (open cycle, combined cycle), by application (power generation, industrial, aviation), and segment forecasts, 2018-2025* – Market research report
- [18] J.C. Han, J.S. Park, C.K. Lie (1984) – *Heat Transfer and Pressure Drop in Blade Cooling Channels with Turbulence Promoters* – Texas A&M University College Station (prepared for NASA CR-3837)
- [19] J.C Han, S. Dutta, S. Ekkad (2013) – *Gas Turbine Heat Transfer and Cooling Technology* – CRC Press Taylor & Francis Group
- [20] J.E. Hart (1971) – *Instability and secondary motion in a rotating channel flows* – Journal of Fluid Mechanics, vol. 45, pp. 341-351
- [21] Hightempmetals – <http://www.hightempmetals.com/techdata/hitempInconel600data.php> – last consulted on 24/10/2019
- [22] P.T. Ireland, T.V. Jones (2000) – *Liquid crystal measurements of heat transfer and surface shear stress* – Measurement Science and Technology, vol. 11, pp. 969-986
- [23] ISO 5167-2 (2003) – *Measurement of fluid flow by means of pressure differential devices inserted in circular cross-section conduits running full - Part 2: Orifice plates* –
- [24] J.P. Johnston, R.M. Halleent, D.K. Lezius (1972) – *Effect of spanwise rotation on the structure of two-dimensional fully developed turbulent channel flow* – Journal of Fluid Mechanics, vol. 56, pp. 533-557

- [25] V.U. Kakade, G.D. Lock, M. Wilson, J.M. Owen, J.E. Mayhew (2009) – *Accurate heat transfer measurements using thermochromic liquid crystal. Part 1: Calibration and characteristics of crystals* – International Journal of Heat and Fluid Flow, vol. 30, pp. 939-949
- [26] J.R. Kingsley-Rowe, G.D. Lock, J.M. Owen (2005) – *Transient heat transfer measurements using thermochromic liquid crystal: lateral-conduction error* – International Journal of Heat and Fluid Flow, vol. 26, pp. 256-263
- [27] S. Kline, F. McClintock (1953) – *Describing uncertainties in single-sample Experiments* – Mechanical Engineering, vol. 75, pp. 3-8
- [28] Laboratory of the group of Materials Science and Technology of Terni that operates at the faculty of engineering of the University of Perugia – <http://www.nanofun.net/>
- [29] B. Lakshminarayana (1996) – *Turbine cooling and heat transfer. In Fluid Dynamics and Heat Transfer of Turbomachinery* – John Wiley, New York, pp. 597-721
- [30] LCR Hallcrest – *Handbook of thermochromic Liquid Crystals Technology* – <https://www.lcrhallcrest.com/liquid-crystal-handbook/>, last consulted on 24/10/2019
- [31] P. Ligrani (2013) – *Heat Transfer Augmentation Technologies for Internal Cooling of Turbine Components of Gas Turbine Engines* – International Journal of Rotating Machinery, col. 20, n. 3, pp. 493-499
- [32] M.G. Lucas, P.T. Ireland, Z. Wang, T.V. Jones (1992) – *Fundamental studies of impingement cooling thermal boundary conditions* – AGARD, Conference Proceeding
- [33] I. Mayo, T. Arts, A. El-Habib, B. Parres (2014) – *Two-dimensional heat transfer distribution of a rotating ribbed channel at different Reynolds numbers* – Journal of Turbomachinery, vol. 137
- [34] I. Mayo, G.L. Gori, T. Arts (2016) – *Aerothermal characterization of a rotating ribbed channel at engine representative conditions - Part I: High-resolution particle image velocimetry measurements* – Journal of Turbomachinery, vol. 138
- [35] I. Mayo, G.L. Gori, T. Arts (2016) – *Aerothermal characterization of a rotating ribbed channel at engine representative conditions - Part II: detailed liquid crystal thermography measurements* – Journal of Turbomachinery, vol. 138
- [36] D.E. Metzger, D.E. Larson (1986) – *Use of melting point surface coatings for local convection heat transfer measurements in rectangular channel flows with 90-deg turns* – Journal of Heat Transfer, vol. 108, pp. 48-54

- [37] C. Mucignat, A. Armellini, L. Casarsa (2013) – *Flow field analysis inside a gas turbine trailing edge cooling channel under static and rotating conditions: effect of ribs* – International Journal of Heat and Fluid Flow, vol. 42, pp. 236-250
- [38] J.M. Owen, Y. Yan (2002) – *Uncertainties in transient heat transfer measurements with liquid crystal* – International Journal of Heat and Mass Transfer, vol. 23, pp. 29-35
- [39] F. Pagnacco, L. Furlani, A. Armellini, L. Casarsa, A. Davis (2016) – *Rotating heat transfer measurements on a multi-pass internal cooling channel – I Rig Development* – ASME Turbo Expo, GT2016-56308
- [40] F. Pagnacco, L. Furlani, A. Armellini, L. Casarsa, A. Davis (2016) – *Rotating heat transfer measurements on a multipass internal cooling channel – II experimental tests* – ASME Turbo Expo, GT2016-56307
- [41] J.A. Parson, J.C. Han, Y. Zhang (1994) – *Wall heating effect on local heat transfer in a rotating two-pass square channel with 90° rib turbulators* – International Journal of Heat and Mass Transfer, vol. 37, n.9, pp. 1411-1420
- [42] M. Pascotto, A. Armellini, C. Mucignat, L. Casarsa (2014) – *Coriolis Effects on the Flow Field Inside a Rotating Triangular Channel for Leading Edge Cooling* – Journal of Turbomachinery, vol. 136
- [43] R. Poser, J. von Wolfersdorf, E. Lutum (2007) – *Advanced evaluation of transient heat transfer experiments using thermochromic liquid crystals* – Journal of Power and Energy, vol. 221, pp. 793-801
- [44] O. Pountney, G. Cho, G.D. Lock, J.M. Owen (2012) – *Solutions of Fourier's equation appropriate for experiments using thermochromic liquid crystal* – International Journal of Heat and Mass Transfer, vol. 55, pp. 5908-5915
- [45] Y. Ruquan, L. Haiwang, W. Kuan, T.Zhi (2017) – *Two-dimensional heat transfer distribution in a rotating smooth rectangular channel with four surface heating boundary condition* – Advances in Mechanical Engineering, vol. 9
- [46] D.L. Schultz, T.V. Jones (1973) – *Heat transfer measurements in short duration hypersonic facilities* – Agardograph No. 165
- [47] C.G. Speziale (1982) – *Numerical study of viscous flow in rotating rectangular ducts* – Journal of Fluid Mechanics, vol. 122, pp. 251-271
- [48] C.G. Speziale, S. Thangam (1983) – *Numerical study of secondary flows and roll-cell instabilities in rotating channel flow* – Journal of Fluid Mechanics, vol. 130, pp. 377-395
- [49] A.R. Smith (1978) – *Color Gamut Transform Pairs* – SIGGRAPH 78 Conference Proceedings, pp. 12-19

-
- [50] J. Stasiek, M. Wierzbowski, S. Klosowicz, J. Zmija, M.W. Collins (2002) – *Liquid crystals thermography for technical and biomedical application* – Design and Nature, 3, pp. 347-354
- [51] D.J. Tritton (1992) – *Stabilization and destabilization of turbulent shear flow in a rotating fluid* – Journal of Fluid Mechanics, 241, pp. 503-523
- [52] Z. Wang, R. Corral (2017) – *Numerical study of effect of wall heating conditions on heat transfer performance of rotating internal cooling channel* – Proceedings of 12th European Conference on Turbomachinery Fluid dynamics & Thermodynamics, n. 357
- [53] R. Wiberg, N. Lior (2004) – *Errors in thermochromic liquid crystal thermometry* – review of Scientific Instruments, n. 75, pp. 2985-2994